2018

DESIGN AND ANALYSIS OF A 3D-PRINTED, THERMOPLASTIC ELASTOMER (TPE) SPRING ELEMENT FOR USE IN CORRECTIVE HAND ORTHOTICS

Kevin Thomas Richardson
University of Kentucky, krichardson080@gmail.com
Author ORCID Identifier:
 https://orcid.org/0000-0002-8736-3319
Digital Object Identifier: https://doi.org/10.13023/etd.2018.466

STUDENT AGREEMENT:

I represent that my thesis or dissertation and abstract are my original work. Proper attribution has been given to all outside sources. I understand that I am solely responsible for obtaining any needed copyright permissions. I have obtained needed written permission statement(s) from the owner(s) of each third-party copyrighted matter to be included in my work, allowing electronic distribution (if such use is not permitted by the fair use doctrine) which will be submitted to UKnowledge as Additional File.

I hereby grant to The University of Kentucky and its agents the irrevocable, non-exclusive, and royalty-free license to archive and make accessible my work in whole or in part in all forms of media, now or hereafter known. I agree that the document mentioned above may be made available immediately for worldwide access unless an embargo applies.

I retain all other ownership rights to the copyright of my work. I also retain the right to use in future works (such as articles or books) all or part of my work. I understand that I am free to register the copyright to my work.

REVIEW, APPROVAL AND ACCEPTANCE

The document mentioned above has been reviewed and accepted by the student's advisor, on behalf of the advisory committee, and by the Director of Graduate Studies (DGS), on behalf of the program; we verify that this is the final, approved version of the student's thesis including all changes required by the advisory committee. The undersigned agree to abide by the statements above.

<div align="right">

Kevin Thomas Richardson, Student

Dr. Lyndon Scott Stephens, Major Professor

Dr. Alexandre Martin, Director of Graduate Studies

</div>

DESIGN AND ANALYSIS OF A 3D-PRINTED, THERMOPLASTIC ELASTOMER
(TPE) SPRING ELEMENT FOR USE IN CORRECTIVE HAND ORTHOTICS

_____

THESIS

_____

A thesis submitted in partial fulfillment of the
requirements for the degree of Master of Science in Mechanical Engineering in the
College of Engineering
at the University of Kentucky

By

Kevin Thomas Richardson

Lexington, Kentucky

Director: Dr. Lyndon Scott Stephens, Professor of Mechanical Engineering

Lexington, Kentucky

2018

ABSTRACT OF THESIS

DESIGN AND ANALYSIS OF A 3D-PRINTED, THERMOPLASTIC ELASTOMER
(TPE) SPRING ELEMENT FOR USE IN CORRECTIVE HAND ORTHOTICS

This thesis proposes an algorithm that determine the geometry of 3D-printed, custom-designed spring element bands made of thermoplastic elastomer (TPE) for use in a wearable orthotic device to aid in the physical therapy of a human hand exhibiting spasticity after stroke. Each finger of the hand is modeled as a mechanical system consisting of a triple-rod pendulum with nonlinear stiffness at each joint and forces applied at the attachment point of each flexor muscle. The system is assumed quasi-static, which leads to a torque balance between the flexor tendons in the hand, joint stiffness and the design force applied to the fingertip by the 3D-printed spring element. To better understand material properties of the spring element's material, several tests are performed on TPE specimens printed with different infill geometries, including tensile tests and cyclic loading tests. The data and stress-strain curves for each geometry type are presented, which yield a nonlinear relationship between stress and strain as well as apparent hysteresis. Polynomial curves are used to fit the data, which allows for the band geometry to be designed. A hypothetical hand is presented along with how input measurements might be taken for the algorithm. The inputs are entered into the algorithm, and the geometry of the bands for each finger are generated. Results are discussed, and future work is noted, providing a means for the design of a customized orthotic device.

KEYWORDS: 3D-Printing, Orthotics, Rehabilitation, Biomechanics, Elastomers, Personalized Medicine

___Kevin Thomas Richardson__

_____December 7th, 2018_____

DESIGN AND ANALYSIS OF A 3D-PRINTED, THERMOPLASTIC ELASTOMER
(TPE) SPRING ELEMENT FOR USE IN CORRECTIVE HAND ORTHOTICS

By

Kevin Thomas Richardson

_____Dr. Lyndon S. Stephens_____
Director of Thesis

_____Dr. Alexandre Martin_____
Director of Graduate Studies

_____December 7th, 2018_____

Acknowledgements

The completion of this thesis would not have been possible without the support and guidance of a number of key individuals and organizations. I first want to express my utmost gratitude to my Thesis Chair and Faculty Advisor, Dr. Lyndon Scott Stephens. His guidance and advice from his years of experience in academics, industry, and life in general proved to be one of the most valuable assets to my academic career. I'm ever grateful of the opportunities he provided for me, and the inspiration and encouragement to pursue those opportunities. I also want to thank Dr. Lumy Sawaki and Dr. Justin Huber for their invaluable contribution to this thesis and to my understanding of and motivation to study biomedical engineering. I want to thank my friends and family for being understanding when research took priority over social gatherings and family events. I want to thank my girlfriend, Shannon Vinci, for being patient and supportive from my first day of my graduate program to its last day. I also want to thank the members of my Thesis Committee, Dr. Johné Parker and Dr. Keith Rouch, for their recommendations and contributions.

I want to give recognition to a few organizations that provided value to this endeavor. I give thanks to the University of Kentucky Department of Mechanical Engineering and Department of Material Science Engineering for the resources made available to me, including workspace, equipment, and faculty. I also want to thank my supervisors at Ergo Mechanical Industrial for being accommodating towards my school schedule and being patient when my presence was greatly needed. I give thanks to Cardinal Hill Rehabilitation Hospital for resources made available to me, including meeting space, staff, and medical equipment.

I also want to thanks a number of current and former students at the University of Kentucky: Joey Stieha for his assistance during my teaching assistantship, insights, and friendship; Bo Tan for his support during writing and his friendship; Floyd Taylor for training me to use the

Contents

List of Tables

List of Figures

1 Introduction

1.1 Stroke Rehabilitation

There are currently 23 million stroke survivors in the United States, with nearly 800,000 strokes occurring every year. Stroke occurs when the flow of blood to the brain is blocked by either a blood clot (ischemic stroke) or the rupturing of a weakened blood vessel (hemorrhagic stroke). The result is the death of parts of the brain, which can cause a wide variety of disabilities ranging from speech impairment to memory loss to loss of motor skills in any area of the body.

Approximately 40% of stroke survivors have severe impairments that require special care and result in reduced quality of life. People with severe hemiparesis (i.e., almost no voluntary movement in the affected upper extremity) continue to have urgent need for rehabilitation yet have historically been underrepresented in research. For example, a hand that is affected by stroke will have lower strength and less sensation, causing many stroke survivors to not use that hand in activities of daily living. This leads to muscle atrophy, shortening of muscle fibers and tendons in the affected hand, a smaller pennation angle, and more compliant tendons (Gray et al, 2012). If the hand is not stretched and exercised, the tendons will lose their elasticity and become permanently shortened. Additionally, a stroke survivor may experience spasticity in their affected limbs. Spasticity is a tightness in the muscles due to involuntary contractures. Under normal function, the brain is able to send signals to these muscles to relax. After stroke, the brain is not able to do so, and the result is a constant tone in the muscles. This adds to the potential of permanent disability. Thus, the goal of physical therapy for someone with hand and arm weakness is to stretch and exercise the hand with hopes of recovery at most and prevention of permanent deformation at least.

Physical therapy for stroke survivors is often a long-term process – months if not years are spent going to rehabilitation exercise sessions. These sessions are often no more than an hour long and occur no more than three times per week in an inpatient rehabilitation setting. Recovery from impairments depends to some degree on spontaneous recovery but mostly on neuroplasticity. Neuroplasticity is the capacity of the central nervous system to reorganize and rewire itself, which precedes functional motor recovery. Neuroplasticity depends on training that is highly repetitive with progressive challenge and salience in order to elicit use of the limbs most affected by stroke. With a highly spastic hand, a patient has difficulty to engage it in practical ways during their recovery. Devices do exist that allow patients to perform physical therapy in the comfort of their own home. However, these devices are often mass-produced and based on a design that fits an "average" hand. This causes discomfort when the device is worn for long periods of time, which stunts the potential for more frequent exercise and, thus, a faster recovery.

1.2   Human Hand Anatomy

The human hand is a complex arrangement of bones, ligaments, muscles, and tendons. A comprehensive understanding of the hand's anatomy can be found in Human Anatomy: Color Atlas and Textbook by Gosling, Harris, Humpherson, Whitmore, and Willan. For the function of finger flexion, the involved bones are the metacarpals (MC), the proximal phalanges (PP), the medial phalanges (MP), and the distal phalanges (DP), shown in Figure 1.1.
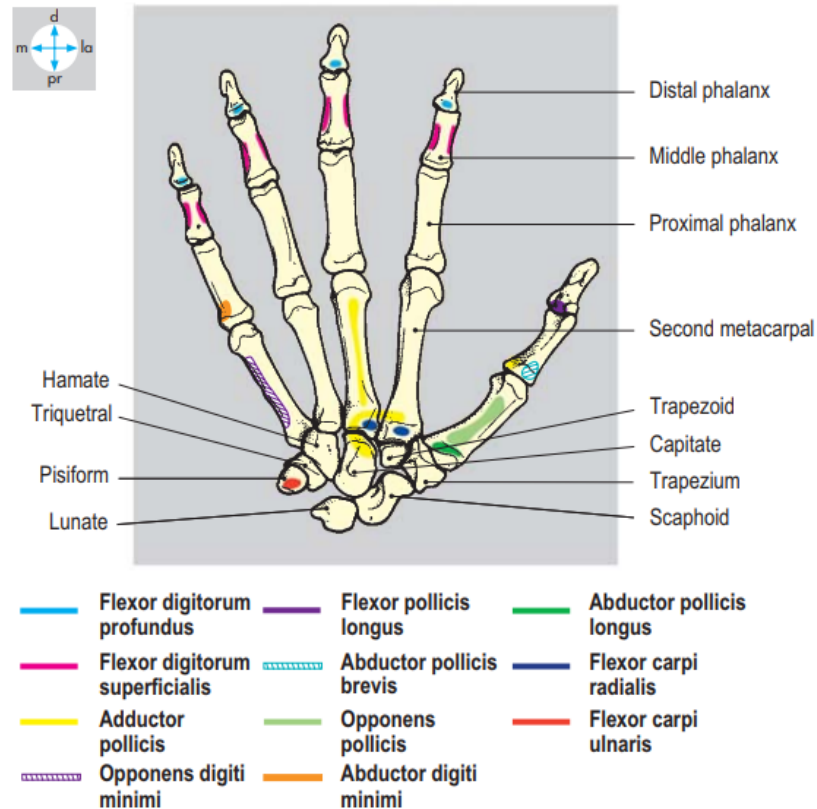
Figure 1.1: Skeletal system of the human hand, with connection points of muscle tendons (Gosling, et al. 2008)

These bones are held together by ligaments between each bone, creating the finger joints: the metacarpophalangeal (MCP) joint, the proximal interphalangeal (PIP) joint, and the distal interphalangeal (DIP) joint. The flexor muscles that actuate these joints are categorized as intrinsic - connecting to a bone or ligament of the hand – and extrinsic – connecting to a bone or ligament not found within the hand. The intrinsic muscles are the lumbricals and the interossei. The lumbricals attach proximally to the flexor digitorum profundus (FDP) muscle and attach distally to the extensor expansions. The interossei attach proximally along the shafts of the metacarpal bones and distally to the base of the proximal phalanx and the extensor expansion. The extrinsic muscles include the flexor digitorum profundus (FDP) and the flexor digitorum

superficialis (FDS). The FDP muscle is found in the forearm, with a tendon running through the length of the forearm up to the palmar side of the wrist, where the tendon splits into four segments for each of the four fingers. Each of the FDP tendons in the hand then attach to the base of the distal phalanx. The FDS also originates in the forearm and the FDS tendon splits at the wrist in a similar fashion as the FDP tendons. The FDS attaches to the palmar side of the proximal phalanx. The attachment points described are shown in Figure 1.1.

The FDP and FDS tendons are the major contributors to finger flexion, with the FDS contributing more than FDP to the actuation of the PIP joint, and the FDP contributing more than FDS to the actuation of the MCP (Yang et al, 2016). The extrinsic flexor tendons are held closely against the shafts of the MC, PP, MP, and DP bones through flexor tendon sheaths, shown in Figures 1.2 and 1.3. These tendon sheaths prevent bowstringing of the tendons as the fingers are flexed, creating an efficient means for producing joint rotation in the fingers. These efficiencies are discussed in (Rispler, et al. 1996). The lumbricals and palmar interossei also contribute to finger flexion when rotation of the MCP joint is desired with all other interphalangeal joints extended (Wang, McGlinn and Chung 2014). The extensor expansion includes lateral bands that, when slipped below the axis of rotation of the MCP joint for flexion/extension of the finger, causes the finger to flex in the prescribed manner.
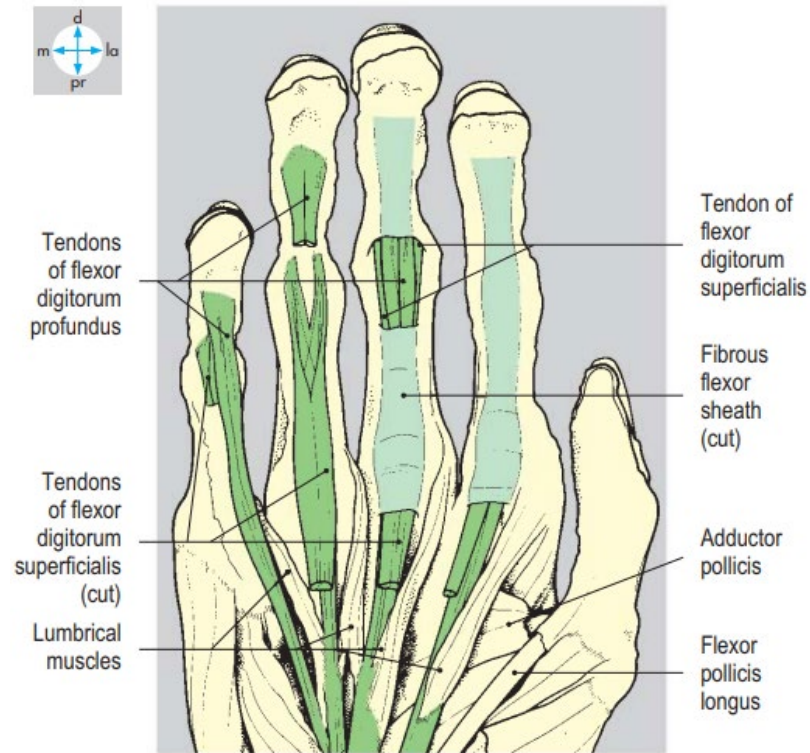
Figure 1.2: Palmar view illustration of flexor tendons and flexor tendon sheaths (Gosling, et al. 2008)
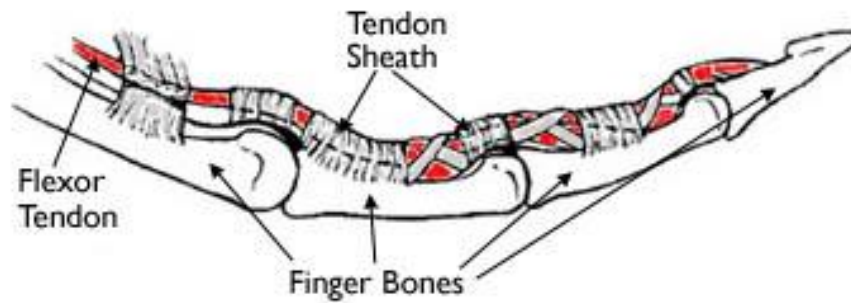
Figure 1.3: Lateral view illustration of flexor tendon sheaths (Flexor Tendon Injuries 2011)

1.3   3D Printing

The fabrication method of three-dimensional (3D) printing was invented in the early 1980s, and since then has grown to be used in rapid prototyping, manufacturing, and other applications. The most common method of 3D-printing is known as fused filament deposition (FFD), also referred to as fused filament fabrication (FFF), which was developed by Scott Crump and patented in 1989. While there are many iterations and designs of FFD printers, they all use the same method of depositing melted material, layer by layer, onto a print bed. The following description of an FFD printer is based upon a printer similar to that used in this study.

In the FFD process, material is supplied in the form of a filament, stored on a reel that is mounted onto the printer. The filament is fed into an extruder nozzle via a hob gear connected to a stepper motor, which provides precision extrusion. The extruder nozzle is connected to thermistors, which heat the nozzle up to or beyond the melting point of the material. This melts the material inside the nozzle. The hob gear and stepper motor, meanwhile, are continuing to push the preceding solid filament, which pushes the melted material out of the extruder. The extruding process is shown in Figure 1.4.
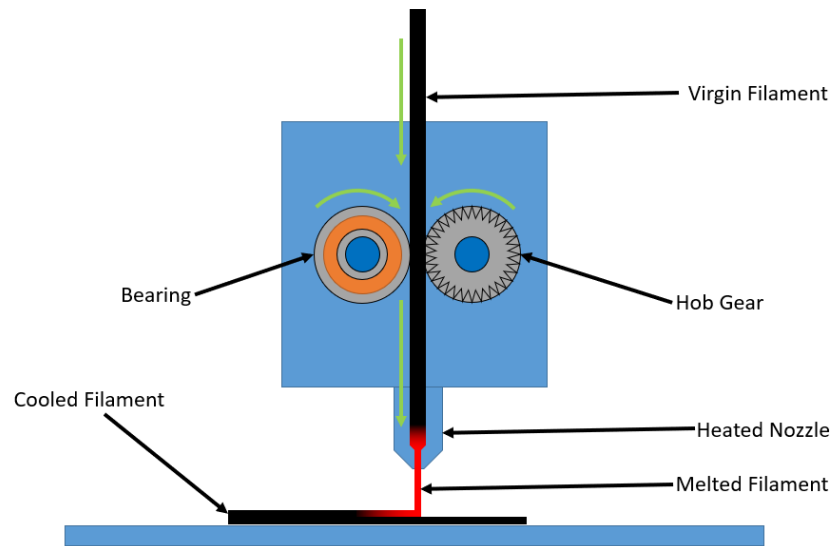
Figure 1.4: Illustration of FFD extrusion process

The apparatus shown in Figure 1.4, including the bearing, hob gear, housing, and heated nozzle, is referred to as the printer head. shows an image of the printer head for comparison with the illustration in Figure 1.4. The image is taken from the printer used in this study. The filament is black and shown between the hob gear and the ball bearing. In this printer head, the ball bearing exerts a force on the filament controlled by the adjustable springs shown on the top left. This is done such that the filament does not slip while the hob gear is rotating, ensuring accurate extrusion of material.
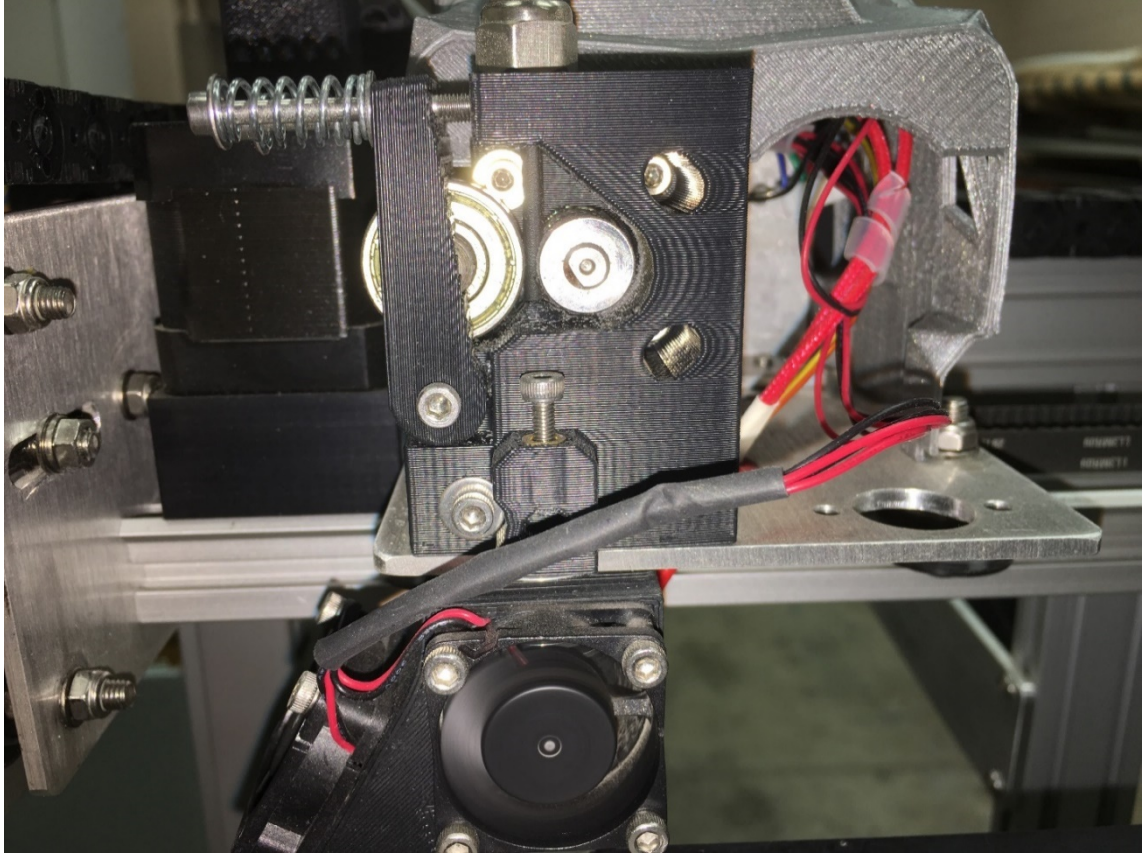
Figure 1.5: Printer head used in FFD extrusion process

The printer head is mounted onto mechanical carriage that facilitates movement in the "X" and "Y" axes, defined as the axes that create the plan parallel to that of the ground plane that the printer sits on. The movement along these axes is powered by stepper motors, which transmit rotational motion into linear motion through the use of timing pulleys and timing belts. The carriage is attached, in some fashion, to timing belts along the "X" and "Y" axes. This provides the means for printing each layer of a part, often designed in a 3D-modeling or computer-aided design (CAD) program and separated into layers through a slicer program (often simply referred do as a "slicer"). A picture of the mechanism present on the printer used in this study is shown in Figure 1.6.

Figure 1.6: FFD printer "X" and "Y" travel mechanism

To create a new layer within a print, the print bed, defined as the surface on which the first layer of material is deposited from the printer head, is moved along the "Z" axis, defined as the axis perpendicular to the "X" and "Y" axes. This movement is facilitated by a stepper motor, which transmits its rotational motion into linear motion through the rotation of an acme threaded rod connected to the motor. A ball screw is fashioned onto the rod and is attached to the print bed. As the stepper motor rotates, the acme threaded rod rotates with it, and the ball screw follows the threads up or down depending on the direction of rotation, moving the print bed up or down. This mechanism is represented in Figure 1.7.

Figure 1.7: FFD printer "Z" travel mechanism

One of the unique benefits of 3D-printing is the ability to adjust the infill of the printed

part. Infill refers to the material present in the part that is not present on an external surface.

From an aesthetic perspective, this material is not visible once the part is printed. Infill material

may be reduced by specifying an infill percentage, denoting the percentage of inside volume that

will be filled with material. Doing so results in a printed part that looks the same externally, but

saves the material used, time duration, and cost of the print. However, reducing infill will

inadvertently change the bulk material properties of the part, and should be considered when using the printed part in an application that will exert a load on the part.

One of the most common materials available for use in 3D-printing include thermoplastics such as acrylonitrile butadiene styrene (ABS) and polylactic acid (PLA), since they become formable after sufficient heat is applied and maintain some level of rigidity. The 3D-printing of metals, rubber-like materials, organic materials, and composites are newer areas of research and application of FFD printing. One material of interest within this list of specialized materials is NinjaFlex, a thermoplastic elastomer (TPE) created by NinjaTek as a filament for use in 3D-printing. The TPE comes in the form of a filament and combines the advantages of elastomers and thermoplastics. The elastomer portion causes the material to behave like rubber, providing the benefits of true flexibility and softness. The thermoplastic portion allows the material to be melted and solidified repeatedly, which is a necessity for materials being used in FFD printing. The thermoplastic portion also provides some added strength to the material. NinjaFlex has a reported 660% elongation, superior abrasion resistance compared to ABS and PLA, chemical resistance to many materials, and a low-friction filament exterior for smooth feeding through the heated extruder of the printer (Fenner Drives 2016). These properties led to the choosing of this material for use in tensile testing in this study. The material is intended to be used for the spring elements providing an assistive opening force to a person's finger.

1.4   3D Scanning and Imaging

3D scanning is defined as the process of obtaining real-world object data, such as its shape and/or color and translating that data into a three-dimensional (3D) model of the object for use in a wide variety of applications. There are many different types of 3D scanners, such as contact,

non-contact active, modulated light, and others. For sake of brevity, only the type of scanner used in this study will be introduced.

Structured-light 3D scanning is a method of 3D scanning that utilizes projected light patterns and a camera system to generate a 3D image of a real-world object. In principle, a thin band of light is projected onto a real-world object. Due to the changes in surface geometry of this object, the thin band of light, or stripe, is distorted when viewed from other perspectives than that of the projector. Cameras mounted in ways that show these other perspectives capture the distortion. This data can then be utilized to construct the surface in a 3D model. In reality, structured-light 3D scanners make use of many of these stripes at once to capture large amounts of data for mapping the surface of the object. The apparatus and function are illustrated in Figure 1.8.
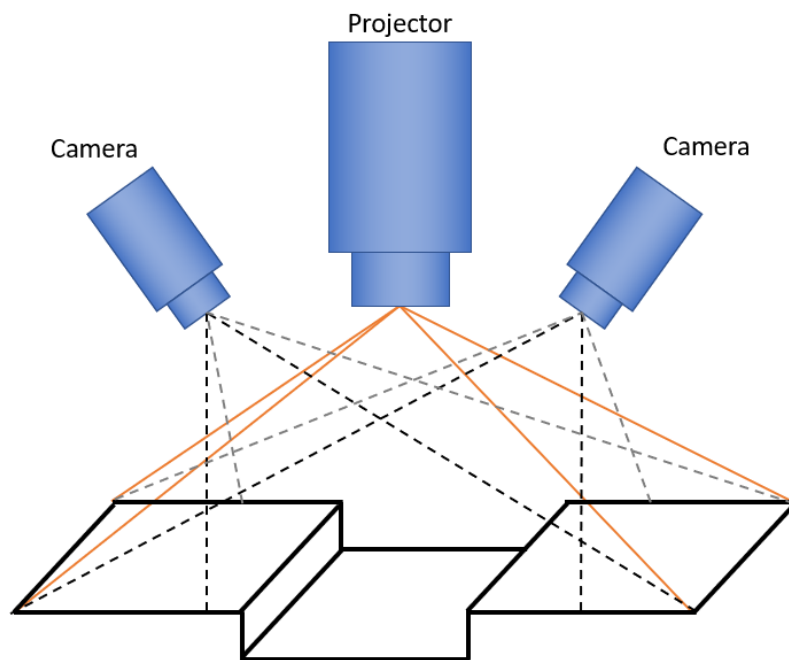
Figure 1.8: Illustration of structured-light 3D scanner apparatus

1.5   Literature Review

Establishing the groundwork for this study requires an examination of recent works in the areas of human hand biomechanics, 3D printing, and hand orthotics.

1.5.1   Human Hand Biomechanics

Biomechanics of the human hand are of particular interest to medical professionals and engineers alike, with signs that knowledge of its kinematics add value to the clinical assessment of their functionality (Bigoni, et al. 2016). Hanten et al studied a group of 1,182 men and women, aged between 20 and 64 years of age, to determine normative maximum grip strength data (Hanten, et al. 1999). In this study, it was found that hand grip was correlated with age, weight, height, gender, and hand dominance. Furthermore, the grip strength of one hand could be accurately predicted with the known grip strength of the other hand and the known age, weight, height, gender, and hand dominance with 87% of variance accounted for (R = 0.93). However, age, weight, height, gender, and hand dominance were found to only provide 1% of the total variance in the grip after the other hand's grip was entered into the equation, showing that grips of the right and left hand were highly correlated, and one hand's grip strength can be predicted from the known grip strength of the other hand. Moy et al built upon these findings in a 2011 study, which concluded that, for a group of 434 elderly people from a rural state of Malaysia, handgrip was positively correlated (P<0.05) with weight, height, and functional ability, while handgrip was negatively correlated (P<0.05) with depression (Moy, Chang and Kee 2011).

However, a deeper understanding of the mechanisms employed in the act of gripping is desired. MacDermid et al conducted a study to quantify the individual contributions of each finger

to the total grip strength. A group of 35 test subjects tested their grip on a specialized hand dynamometer. It was found that the grip strengths of the left and right hands were highly correlated (R = 0.98), which confirm Hanten's results (MacDermid, et al. 2004). It was also concluded that the percentage contributions of the index, middle, ring, and little fingers to overall grip strength were 25%, 35%, 25% and 14%, respectively. Now, a translation between overall grip strength and individual finger strength has been established. For each of these fingers, a specific group of muscles perform the flexion – the FDP, the FDS, the lumbricals, and the interossei.

A crucial topic in the literature is that of the human finger's movement, and how it is orchestrated by the complex network of muscles, tendons, and ligaments found intrinsically and extrinsically to the finger. In 2001, a study was performed based on a biomechanical model of the index finger. The model incorporated mechanical elements such as ropes, pulleys, and solid bodies to accurately portray the inner workings of the finger. The model's goal was to characterize the dynamic motion of the finger, which resulted in a quantification of the damping and stiffness at each of the three finger joints (MCP, DIP, PIP). The damping coefficients were constant throughout the angle of the joint, while the stiffness coefficient exhibited a second-order dependence on the angle of the joint (Kamper and Rymer 2001). The motion of the finger was further analyzed by examining the contribution of the individual extrinsic flexor muscles (Nimbarte, Kaz and Li 2008), the quantification of moment arms establish by the attachment location of each flexor muscle tendon to the finger bones (Franko, et al. 2011), and finger force production as it relates to finger joint position (Martin, Latash and Zatsiorsky 2012). Several studies also provided kinematics of the hand based on observational studies without relation to the hand's inner workings, which provide a useful contribution to test hand and finger models (Cobos, et al. 2008) (Gustus, et al. 2012) (Samadani, Kulic and Gorbet 2012) (Chen Chen, et al.

2013). In 2014, another model was presented based upon force-based biomechanics of the index finger (Qiu and Kamper 2014). The model was created using MATLAB Simulink and validated using a set of cadaveric hands, estimating the fingertip force of the hand with an average error less than 2° in direction and less than 10% in magnitude across all fingers.

1.5.2   3D-Printed Materials

3D printing has been used for a wide variety of applications, including orthotics (Hipolite 2014), radio technology (Bahr, et al. 2015), printing in zero-G (Johnston, Werkheiser and Cooper 2014), and robotic exoskeletons (Abdallah, Bouteraa and Rekik 2017). This technology is often desirable for its prototyping capabilities, ability to produce custom designs at an affordable price, as well as material properties that can be modified with print parameters. A 2018 study analyzed tensile test results of PLA with various infill shapes and infill volumes, showing the capabilities of 3D printing when it comes to desired material behavior (Arifa, Rahman and Asmatulu 2018). Fatigue tests have also been conducted on 3D-printed materials, such as elastomers (Moore and Williams 2008) (Moore and Williams 2015) and thermoplastic elastomers (TPE), which are a combination of thermoplastics and elastomers (McDonough, John K. (NinjaTek, Division of Fenner Drives, United States) 2016). From the 2012 paper, Moore et al performed fatigue testing on elastomers that were 3D-printed using stereolithography (SLA) printing, in which a photopolymer liquid is placed on a print bed, and ultraviolet light is trained on specific locations to harden the liquid, with the process being repeated for each layer of the part. A special tensile test specimen was created with a beaded edge to be held in specialized elastomer grips to prevent the specimen from pulling out of traditional grips (Moore and Williams 2008). In both studies by Moore et al, hysteresis of the elastomer was shown in the cyclic loading test results, which is a well-known characteristic of elastomers (Ewing 1889). The blending of thermoplastics and elastomers allow

15

for processability and elasticity in a single material known as a thermoplastic elastomer (Spontak and Patel 2000). A study by McDonough in 2016 analyzed the tensile properties of a TPE known as NinjaFlex, a material created by the additive manufacturing material supplier, NinjaTek (McDonough, John K. (NinjaTek, Division of Fenner Drives, United States) 2016).

1.5.3   Hand Diagnostics

Modeling methods in a clinical settings have been studied and established using recent technological innovations in many areas, including 3D scanning in dentistry (Qingmeng, et al. 2012), laser scanning in geology (Kasza 2018), and in particular interest to this study, various methods in human hand modeling. A 1969 study by Clauser et al developed a base of knowledge for weights, volumes, and centers of mass for various segments present in the human body. From this study, average densities of skin, fat, muscle, and bone were considered and tested (Clauser, McConville and Young 1969), which closely resemble figures used in the study by (Qiu and Kamper 2014). With the invention of 3D-modeling software and its advantages, a graphic model of the human hand was created and verified using the modeling software CATIA and 32 human subjects (Davidoff and Freivalds 1993). The model was tested for life-like range of motion for each finger joint, providing 23 degrees of freedom at 17 moveable joints. The hand measurements were compared to those of a study that used sliding calipers, goniometers, and other contact measurement instruments (Garrett 1968). A study by Pham in 2015 proposed a non-contact measurement scheme to determine ranges of motion of the hand. An optical sensor, camera, and computer for data acquisition and processing were used in conjunction with an algorithm to determine the ranges of motion of interphalangeal joints, with the goal of providing a more accurate and sanitary method for measuring compared to the conventional goniometer (Pham, et al. 2015). These studies focus on the range of motion of the human hand. A study by Steinen

et al in 2011 proposed a force-based measurement device to quantify motor impairments after brain injury. The device is used to measure produced torque about joint rotation axes at the wrist joint and at the collective MCP joints of the four fingers (Stienen, et al. 2011).

1.5.4 Hand Orthotics

Hand orthotics have been a useful tool in the field of physical therapy for many years, with more recent developments in creating customized orthotics and devices with biomimetic properties. These devices require an understanding of the biomechanics of the human hand as well as hand diagnostics. An artificial finger joint for anthropomorphic robotic hands is one example (Xu, et al. 2011). The artificial MCP joint takes inspiration from an actual finger joint's anatomy and uses conventional materials such as crocheted fiber and silicone to accomplish life-like joint characteristics. This study provides rationale for the design of a joint replacement, as opposed to an external orthotic device.

Studies have been conducted to test the efficacy of traditional orthotic devices (Lannin, et al. 2016). However, these devices are not customized to an individual's hand. For customized orthotic devices to be created, reverse engineering (RE) of one's hand through knowledge of the hand's biomechanics and kinematics must be performed prior to the design and fabrication of a customized orthotic (Baronio, Harran and Signoroni 2016). After stroke, spasticity makes it difficult to perform this kind of RE, and methods for overcoming such obstacles must be designed and implemented (Baronio, Volonghi and Signoroni 2017). Once RE is completed, knowledge of the individual's hand is established and a proper, customized orthotic may be designed and fabricated. The design and fabrication of various devices have been recorded in the literature, including an EMG-driven actuated glove (Polygerinos, et al. 2015), a glove utilizing actuated

17

exotendons (Lee, Landers and Park 2014), an improved exotendon glove with feedback control (Kim, Lee and Park 2014), and a 3D-printed static fingerboard orthotic (Wang, et al. 2018). In these cases, the gloves that were proposed and created are categorized as either static gloves or active dynamic gloves. Active dynamic gloves are characterized in this paper as having a power source to actuate components that result in the movement of a person's fingers for rehabilitation purposes. For example, the exotendon glove (Lee, Landers and Park 2014) used electrically-driven motors that were connected to cables. The cables attached to the tips of each finger and, once actuated, transformed rotational motion of the motors into linear motion of the cables. The cables pulled the fingers open to provide the assistive force and can be adjusted and controlled to produce a desired finger position.

An area underrepresented in the literature is that of passive dynamic gloves. These gloves still incorporate dynamic motion of the fingers, allowing for flexion of the fingers and changes in finger position. However, they require no power input to do so. Instead, methods such as interchangeable springs and custom-designed elastic bands. A recent study proposed a wearable orthotic device that incorporates these customized elastic bands with existing orthotic devices through the use of 3D printing, which provides crucial benefits to recovery post-stroke (Huber, et al. 2017).

1.6   Contributions

From the findings in the background and literature review, it was apparent that several pieces of information were missing that could be provided by this study. When looking into the anatomy and biomechanics of the human hand, specifically the flexor muscles of the fingers, it was discovered that there was a correlation between overall grip strength and the contributions

of individual fingers to that grip strength (MacDermid, et al. 2004). However, there were no studies found that attempted to find a relation between a finger's grip strength and the contribution of individual flexor muscles to that finger's grip strength. This relation is crucial to this study and application and would provide unique insight into the detailed inner workings of the human hand during finger flexion. Numerous mechanical models of the human finger were found in literature, but none included contributions of the flexor muscles and joint stiffness when the flexor muscles were contracted, in conjunction with an assistive opening force. A model of this nature would include the individual contributions of flexor muscles and further illustrate the mechanisms found in the human hand during finger flexion.

When investigating 3D-printed materials, recent studies were found that placed 3D-printed tensile specimens under fatigue testing, including FFD-printed PLA specimens with varied infill geometries (Arifa, Rahman and Asmatulu 2018) and SLA-printed elastomers (Moore and Williams 2008). However, NinjaFlex TPE was the material of interest for this study. While there was technical data available on the material from the manufacturer (Fenner Drives 2016), no studies had been done on the various infill geometries possible with FFD printing to determine their effects on bulk material properties. This created another opportunity to contribute to the pool of knowledge for 3D-printed materials.

During the review of literature surrounding hand orthotics, many studies were found that used active devices (Kim, Lee and Park 2014), (Lee, Landers and Park 2014), (Polygerinos, et al. 2015). These active devices employed actuators such as servo motors to provide active control over the assistive opening force of the fingers on the hand. Missing from this body of literature were studies examining the design of a passive orthotic device based upon a mechanical model of a spastic hand for use in stroke rehabilitation. A passive device would appeal to the practical

side of rehabilitation, as it would provide a safer, more intuitive device for the wearer. The passive device would also likely have a lower price point, should it make to market as a consumer product.

To summarize, the major contributions made by this paper are listed below:

1. An initial correlation between overall finger grip strength and the contributions of each flexor muscles of that finger to its grip strength

2. A mechanical model of the human finger with flexor muscles and joint stiffness represented, with the addition of an assistive opening force that counteracts the muscles and stiffness when the muscles are contracted

3. Material data on NinjaFlex TPE acquired by testing of printed specimens with various infill geometry

4. A passive orthotic device, designed around a mechanical model of a spastic hand for the use of rehabilitation after stroke

1.7   Thesis Overview

This thesis contributes to the current body of knowledge by providing an innovative method of combining recent developments in the areas of biomechanics, 3D printing, hand diagnostics, and hand orthotics to create a customized orthotic device for a stroke survivor exhibiting mild spasticity in the hand. This design is unique in that it incorporates an algorithm that draws knowledge from human anatomy, biomechanics, material properties of 3D-printed materials, and mechanical engineering design to reverse engineer an individual's hand and provide design parameters for 3D-printed elastic bands to be used in an orthotic device that gives the correct assistive/corrective force to each finger. While this thesis focuses on the application as it pertains to stroke survivors exhibiting spasticity, this design and its process may also be used

for physical therapy required from other groups, such as those involved in car accidents, sports injuries, and wounded veterans.

Chapter 1 provides introductory information for each of the key areas of this paper – stroke rehabilitation, human hand anatomy, 3D printing, and 3D scanning and imaging. It then provides a literature review in the areas of study most-closely related to this paper, which include elements of the key areas – human hand biomechanics, 3D-printed materials, hand diagnostics, and hand orthotics. Chapter 2 provides an in-depth analysis of the proposed system intended to model a human finger within the algorithm, including rationale for assumptions and choices made when designing the system, its behavior and the importance of its behavior, declaration of forces acting upon the system and where they originate, and a final analysis of the balancing of these forces. The algorithm's overall structure will be presented at the end of this chapter. Chapter 3 covers a brief testing of some key material properties of the 3D-printed material, NinjaFlex TPE, including the fabrication details, testing procedures, and a presentation and discussion of the experimental results, including how the material properties are utilized within the algorithm. Chapter 4 illustrates the proposed design of the orthotic device. A fitting procedure is proposed, which provides the inputs needed for the algorithm. A hypothetical hand is presented, along with input values found from the fitting procedures described. The algorithm structure is presented to show the path between inputs from the fitting procedure and outputs to be used in the design of the spring element of the glove. The outputs for this hypothetical hand are presented, and the manner in which these outputs are used for spring element design are discussed. Chapter 5 provides a summary and conclusions made from the paper along with future recommendations to further the work.

The objectives accomplished in this work are presented below:

a) Establishment and rationalization of a model of a human finger based upon human anatomy and biomechanics

b) Description of an algorithm that utilizes the prescribed human finger model to determine design parameters for an elastic band used to balance forces from the finger flexor muscles

c) Collection of experimental data from material testing of TPE that has been 3D-printed with a variety of infill geometries

d) Analysis of the experimental data

e) Proposition of the orthotic design and methods for incorporating algorithm outputs into the design

f) Simulate the fittings and designs of the proposed orthotic for a hypothetical human hand

g) Recommend future areas of investigation to further the translational research found in biomedical engineering

2 System Modeling and Rationale

2.1 Introduction

This chapter introduces the system intended to model a human finger used within the design algorithm. It provides base assumptions made within the model, rationale for those assumptions, characteristic equations used in the system, the behavior of the system, and forces present within the system. The chapter concludes with the structure of the algorithm, largely based upon the system discussed.

2.2 System Description

For the purpose of creating a mechanical system, the human finger was approximated as a triple-rod pendulum, shown in Figure 2.1. The system reflects the anatomy of a realistic human finger, which has three joints – the MCP, DIP, and PIP joints – and three segments made of the PP, MP, and DP bones and the tissue that surrounds them. The MC bones move very little in relation to the PP, MP, and DP bones during typical movement of the hand, and is not considered in the model except as the rigid portion of the MCP joint.
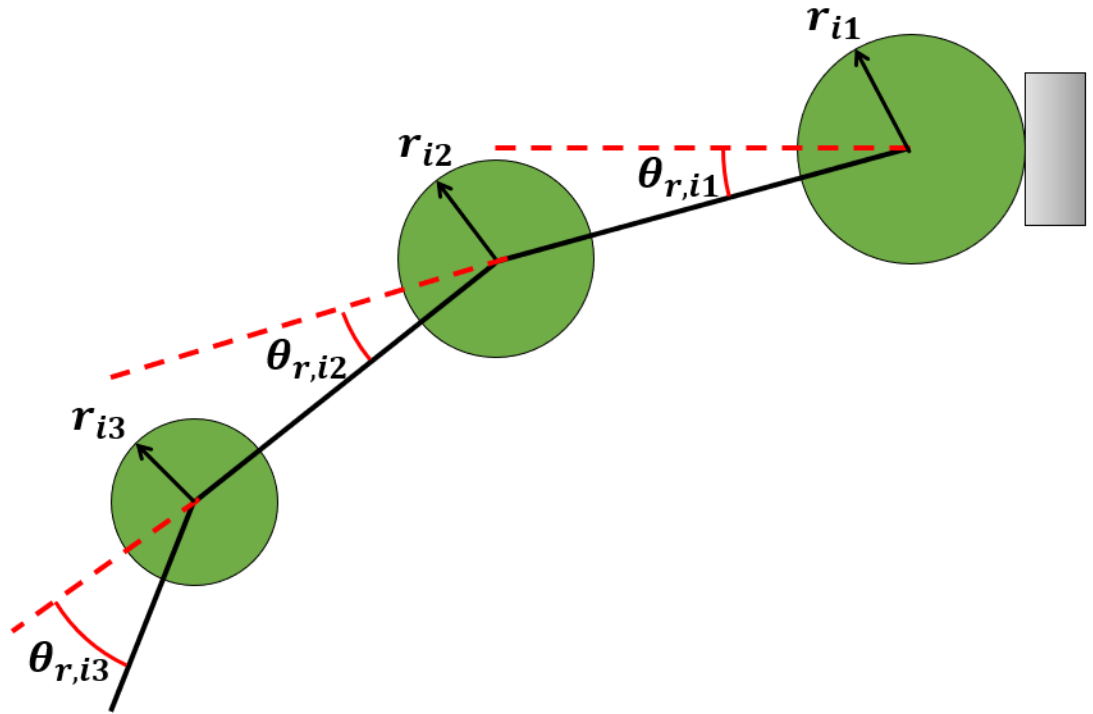
Figure 2.1: Triple-rod pendulum

As noted in the introduction, the finger's flexor muscles connect to the finger in three locations – the lumbricals attach to the extensor expansion, the FDS muscle's tendon attaches to the palmar side of the MP bone, and the FDP muscle's tendon attaches to the palmar side of the PP bone. The tendons are held tightly against the bones within tendon sheaths. In the mechanical system, these tendons are approximated by cables that flex easily but do not stretch axially, which is true to the behavior of a realistic tendon under typical loads that do not result in tendon rupture. The cables are rigidly connected to the appropriate bones and are fed through eyelets connected to the bottom portions of the bones, preventing bowstringing and creating efficient rotation of the joints when pulled. The cables are routed past the MCP joint and are connected to actuators that represent the extrinsic flexor muscles within the forearm that actuate the tendons

24

of a real human hand. This mechanism is shown in Figure 2.2. The extensor muscles and tendons are excluded from this system, since spasticity majorly affects the flexor muscles.
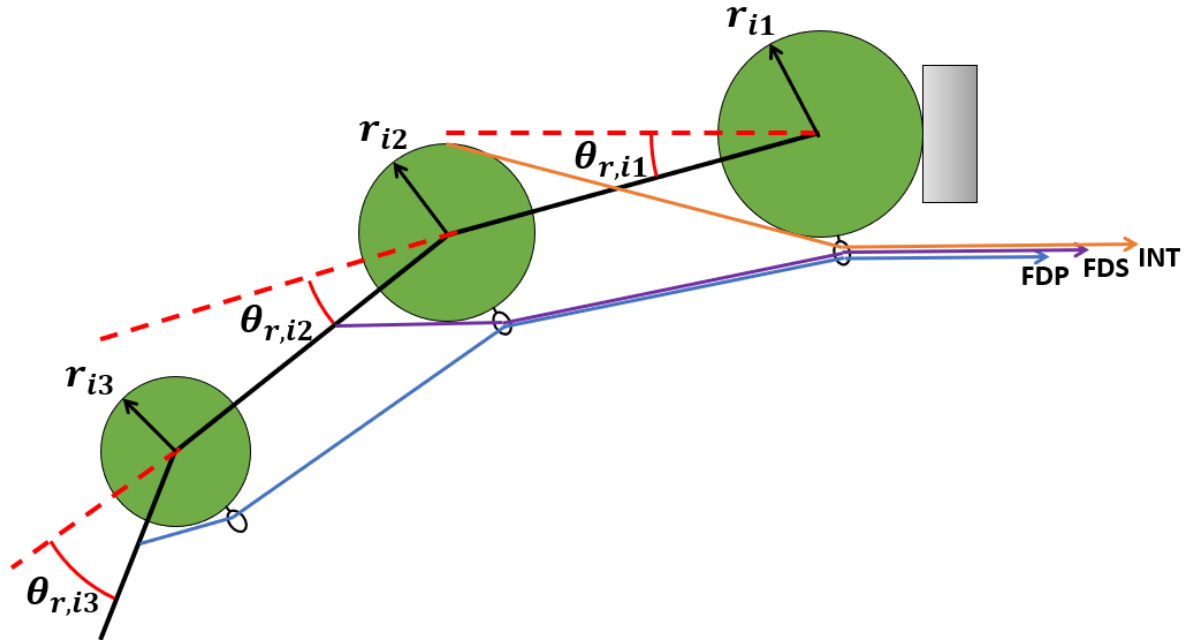
Figure 2.2: Biomechanical model of human finger

To overcome the forces produced by these flexor muscles, the proposed orthotic pulls on the fingertip from the dorsal side with a cable element. In a similar fashion to the mechanical system approximation of the flexor tendons, the orthotic guides the cable through a sheath running the length of the dorsal side of the finger. The cable exits the proximal end of the sheath and connects to a spring element. This spring element is 3D printed and is designed to balance the forces produced by finger flexion and extend the finger a prescribed amount according to clinical specification. The spring element then connects to a rigid support found on the dorsal side of the hand. This mechanism is shown as an addition to the mechanical system approximation of the finger in Figure 2.3.
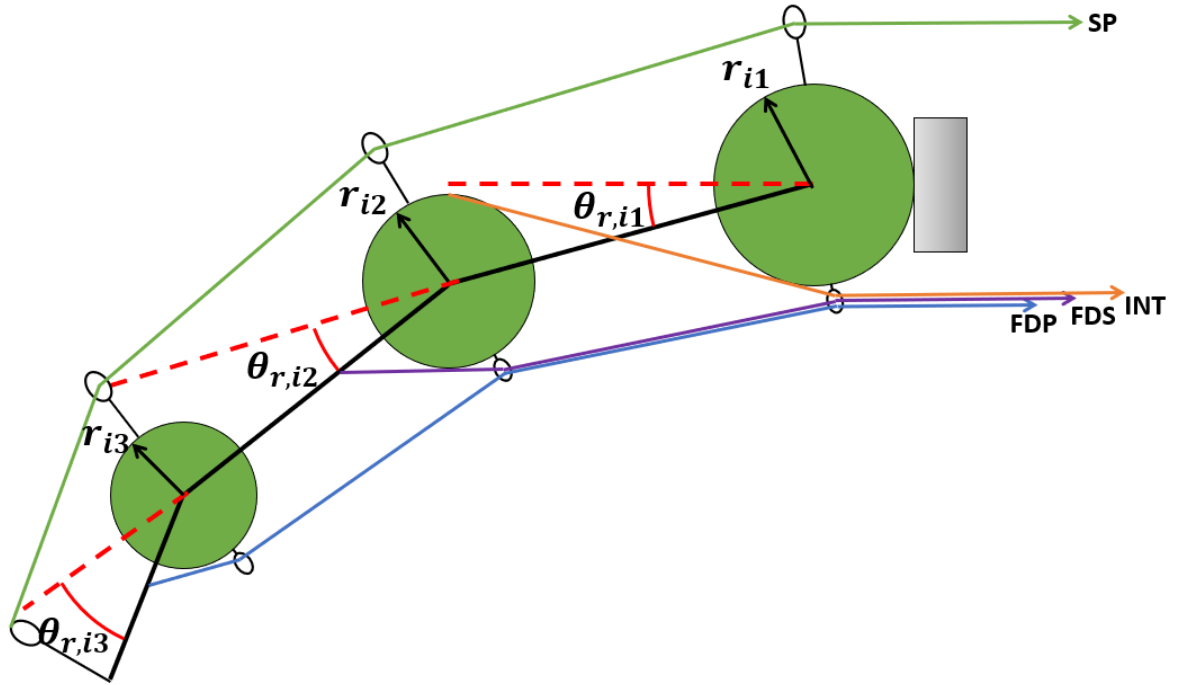
Figure 2.3: Full model of human finger, with spring element

2.3   System Behavior

Initially, the system was treated as a dynamic system with a range of motion similar to that of a realistic human finger. This was the analysis used in Kamper's 2001 study. However, for this application of finding the spring element's produced force that will balance the combined forces of the flexor tendons, there is very little movement if any. For this reason, the system is analyzed as a quasi-static system. While the term "quasi-static" is often used to describe chemical process, it is used here to describe the behavior of the mechanical system that is dynamic in that it has the ability to move but is in fact static due to the balancing of forces. Additionally, it is noted that once the finger flexors' forces are balanced by the spring element and the finger is extended, the finger will be able to flex or extend to the limits of its range of motion by further contracting

26

the flexor muscles or relaxing them, respectively. At this point, a dynamic analysis could be performed for large movement, but this is outside of the realm of this study.

2.4   Declaration and Summation of Joint Torques

Now that the system structure and behavior has been established, the torques at each joint are to be determined appropriately within the quasi-static mechanical system. The torques produced at each joint are used as a means to determine the force required by the spring element and are created by the portion of the flexion forces perpendicular to the radius of the joint extending from the center of rotation to the point of application of the flexion force. To illustrate, Figure 2.4 shows a simplified version of the full mechanical model of the finger to clearly show forces as they affect the finger joints.
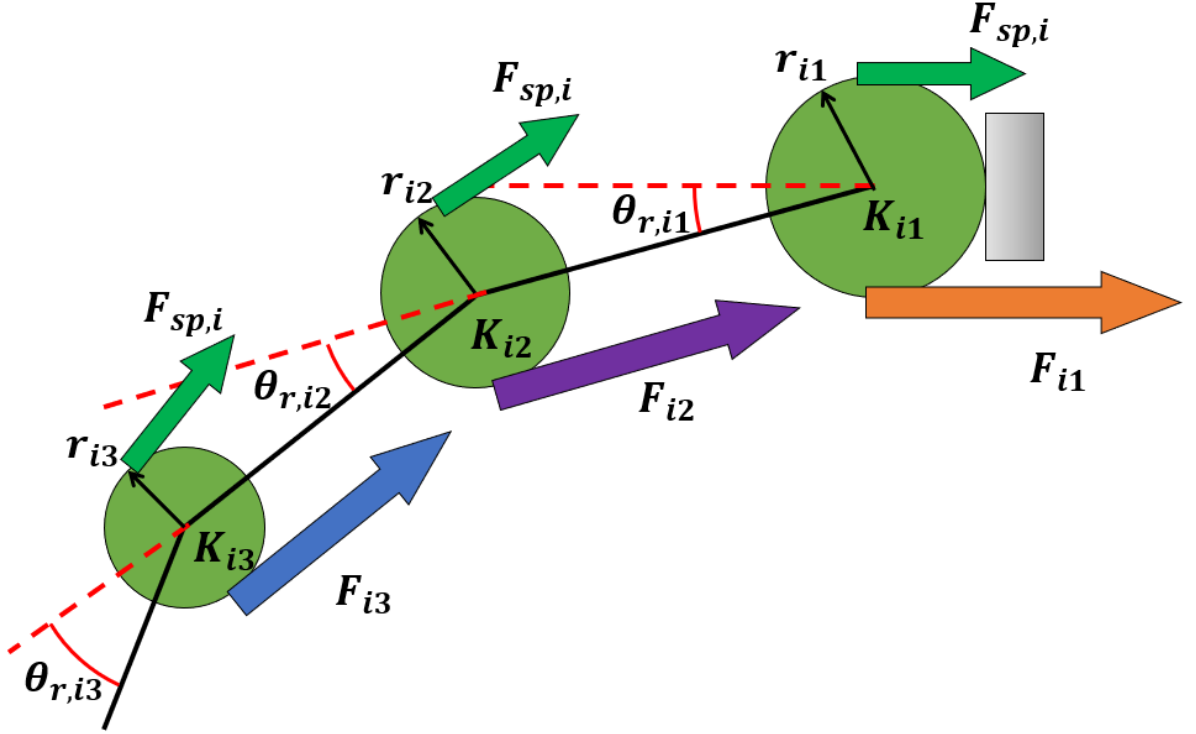
Figure 2.4: Simplified model with acting forces

Before analyzing the torques of the fingers, the forces that produce those torques must be understood and established. The muscles that actuate each finger include the lumbricals, interossei, FDP, and FDS. Muscle strength is determined by Equation (2.1), where F_m is the muscle force, $PCSA$ is the physical cross-sectional area, T_{sp} is the specific tension in the muscle, and ϕ is the pennation angle of the muscle's fibers. Experimental values for $PCSA$ and ϕ of the muscles that actuate the finger were found in previous studies (Jacobson, et al. 1992) (Lieber, et al. 1992). However, T_{sp} was largely missing from the literature for these muscles. As a result, a new method is devised to approximate flexor muscle contribution to overall strength. The method is determined in the following paragraphs.

$$F_m = (PCSA)T_{sp}\cos(\phi) \tag{2.1}$$

Of these variables, the $PCSA$ has the widest range of values (Jacobson et al, 2012). Using this, the main variations within muscle forces of the finger flexor muscles are approximated using the $PCSA$ to normalize those forces with that of the finger's total flexion force, which was found as a portion of the total grip strength in MacDermid's model from 2004, shown in Equation (2.2) for clarification. In the equation, each of the four fingers are denoted by index i, where the index finger is denoted as $i = 1$, the middle finger as $i = 2$, the ring finger as $i = 3$, and the little finger as $i = 4$. Additionally, $F_{i,total}$ denotes the portion of grip strength contributed by the i-th finger, P_i is the percentage of grip force contributed for the i-th finger from MacDermid 2014, and F_{grip} is the measured grip strength of the hand.

$$F_{i,total} = P_i F_{grip} \tag{2.2}$$

The normalization of each finger flexor muscle can be found in Equation (2.3), where each of the three flexor muscle groups are denoted by index j, where the FDP is denoted as $j = 1$, the FDS as $i = 2$, and the intrinsic flexor muscles (lumbricals and interossei) as $j = 3$. Additionally, N_j is the normalized constant of the j-th muscle, $PCSA_j$ is the physical cross-sectional area of the j-th muscle, and $PCSA_{total}$ is the sum of physical cross-sectional area of all five flexor muscles.

$$N_{ij} = \frac{PCSA_{ij}}{PCSA_{i,total}} \tag{2.3}$$

From here, the force of the individual flexor muscles of the finger can be determined by multiplying the normalized constant and the finger's contribution to grip strength. This operation is shown in Equation (2.4), where F_{ij} is the force exerted by the j-th flexor muscle on the i-th finger, and $F_{ij,total}$ is the vector $F_{i,total}$ repeated for three rows (one for each muscle group).

$$F_{ij} = N_{ij}F_{ij,total} \tag{2.4}$$

Now, the moment arms created by the flexor muscles at each finger joint may be calculated. Since the tendons are held closely against the finger bones in reality, the moment arm is approximated to be the apparent radius of each joint, within each finger. The torque can be calculated by using Equation (2.5), where $\tau_{m,ik}$ is the torque by muscle flexion experienced by the k-th joint on the i-th finger, and r_{ik} represents the radius of the k-th finger joint on the i-th finger. The MCP joint is denoted as $k = 1$, the PIP joint is denoted as $k = 2$, and the DIP joint is denoted as $k = 3$.

$$\tau_{m,ik} = F_{ij}r_{ik} \tag{2.5}$$

In this system, the joint stiffness's contribution to the total torque seen by each of the joints is considered as well. The stiffness experienced in each joint is determined by Equation (2.6) (Kamper and Rymer 2001). The stiffnesses exhibit a second-order relation to the relative angle of rotation of each joint, noted in Figure 2.4. These angles are represented as $\theta_{r,ik}$, denoting the relative angle of the k-th joint on the i-th finger. The stiffness is denoted as K_{ik} representing the stiffness of the k-th joint on the i-th finger. The constants a_k, b_k, and c_k are specified in Equations (2.7), (2.8), and (2.9) from results in (Kamper and Rymer 2001). In the study, these constants were determined by a second-order polynomial curve fitting of the data from five adults' index fingers. This fact warrants the statement of two assumptions made. First, for this application of the joint stiffness equations, the middle, ring, and little fingers are assumed to have the same second-order relationship between joint stiffness and joint flexion angle. This assumption would need to be verified by conducting similar experiments and data analysis for those fingers as was conducted on the index finger in the study. Second, the curve fitting of the data is assumed representative of the total population. This assumption suffices for one of the purposes of this study, which is to

30

propose a mechanical model of the human hand. However, it is acknowledged that joint stiffness likely varies from person to person, potentially from factors such as age, finger size, arthritis, previous hand injuries, and more. Specifically, for stroke survivors with spasticity, joint stiffness can add to the effects of spasticity depending on factors such as weather conditions (barometric pressure) and the individual's stress levels. These factors in particular may change in a matter of minutes and introduce a type of uncertainty in the joint stiffness. This uncertainty may be mitigated through use of robust control techniques within the system.

$$K_{ik} = a_k \theta_{r,ik}^2 + b_k \theta_{r,ik} + c_k \tag{2.6}$$

The constants are determined such that each of the stiffnesses are represented in units of N-m/rad. Kamper also determined damping coefficients for each joint of the index finger, which were found to be constant through the rotation of each joint. However, as mentioned, this system is analyzed under static conditions, negating any effects of damping.

$$K_{i1} = 1.019\theta_{r,i1}^2 - 0.541\theta_{r,i1} + 0.454 \tag{2.7}$$

$$K_{i2} = 1.058\theta_{r,i2}^2 - 0.760\theta_{r,i2} + 0.396 \tag{2.8}$$

$$K_{i2} = 0.384\theta_{r,i3}^2 - 0.089\theta_{r,i3} + 0.133 \tag{2.9}$$

From here, the contribution to total joint torque by the stiffness of each joint is calculated by Equation (2.10), where $\tau_{s,ik}$ is the torque from joint stiffness of the k-th joint on the i-th finger.

$$\tau_{s,ik} = K_{ik}\theta_{r,ik} \tag{2.10}$$

The spring element for the i-th finger will be designed to produce a force, identified as $F_{sp,i}$, that will balance the flexor muscle torque $\tau_{m,ik}$ and the joint stiffness torque $\tau_{s,ik}$. In a similar fashion to the forces produced by the flexor muscles, the spring element's force will create a torque about each joint with the moment arm being approximated to the joint radius r_{ik}. Thus,

the equation for spring element torque at the k-th joint on the i-th finger is termed $\tau_{sp,ik}$ and determined by Equation (2.11).

$$\tau_{sp,ik} = F_{sp,i} r_{ik} \tag{2.11}$$

All torques seen by the joints of the i-th finger are shown in Figure 2.5. Noting that the spring force is applied to the tip of the finger from the spring cable attachment shown in Figure 2.3, it became uncertain as to how the force would translate to torques on the finger joints. Namely, the force was thought to either exert a torque on just the third joint (DIP), or on all three joints. To obtain an answer, a quick experiment was conducted. A tactical glove was modified to accommodate a 3D-printed eyelet piece fashioned to the fingertip of the glove, and a piece of fishing wire was inserted through the eyelet and secured. By putting the glove on one hand and pulling the fishing line towards the wrist, the spring cable action was simulated. Through experimental observation, it appeared that all three finger joints saw a reaction from the simulated spring force.
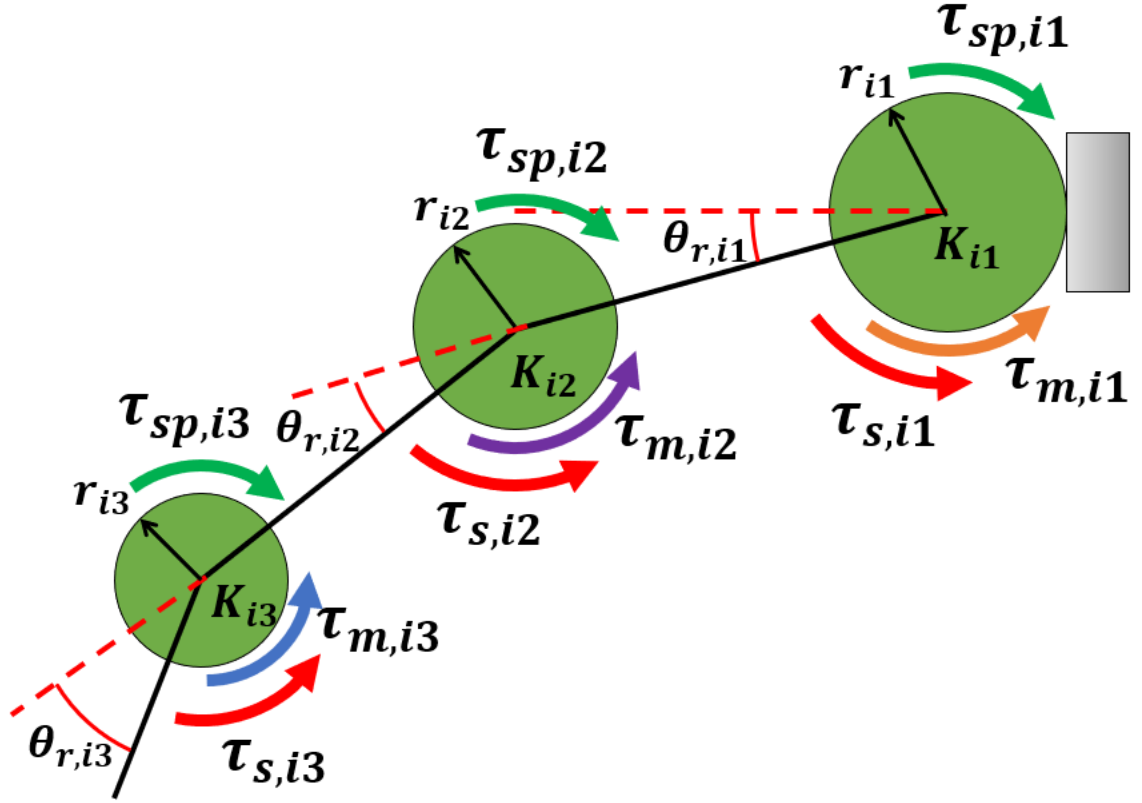
Figure 2.5: Torques acting on finger joints of i-th finger

The summation of torques for the i-th finger is shown in Equation (2.12), from which the required spring force is determined. The equation for determining this spring force is derived and found in Equation (2.13).

$$\sum_{k=1}^{3} \tau_{sp,ik} = \sum_{k=1}^{3} \tau_{s,ik} + \sum_{k=1}^{3} \tau_{m,ik} \tag{2.12}$$

$$F_{sp,i} \sum_{k=1}^{3} r_{ik} = \sum_{k=1}^{3} K_{ik}\theta_{r,ik} + \sum_{k=1}^{3} F_{ij}r_{ik}$$

$$F_{sp,i} = \frac{\sum_{k=1}^{3} K_{ik}\theta_{r,ik} + \sum_{k=1}^{3} F_{ij}r_{ik}}{\sum_{k=1}^{3} r_{ik}} \tag{2.13}$$

2.5 Design of Spring Element

The spring element in this system is assumed to have a rectangular cross-section and shall only see the applied force along its major axis, shown in Figure 2.6.
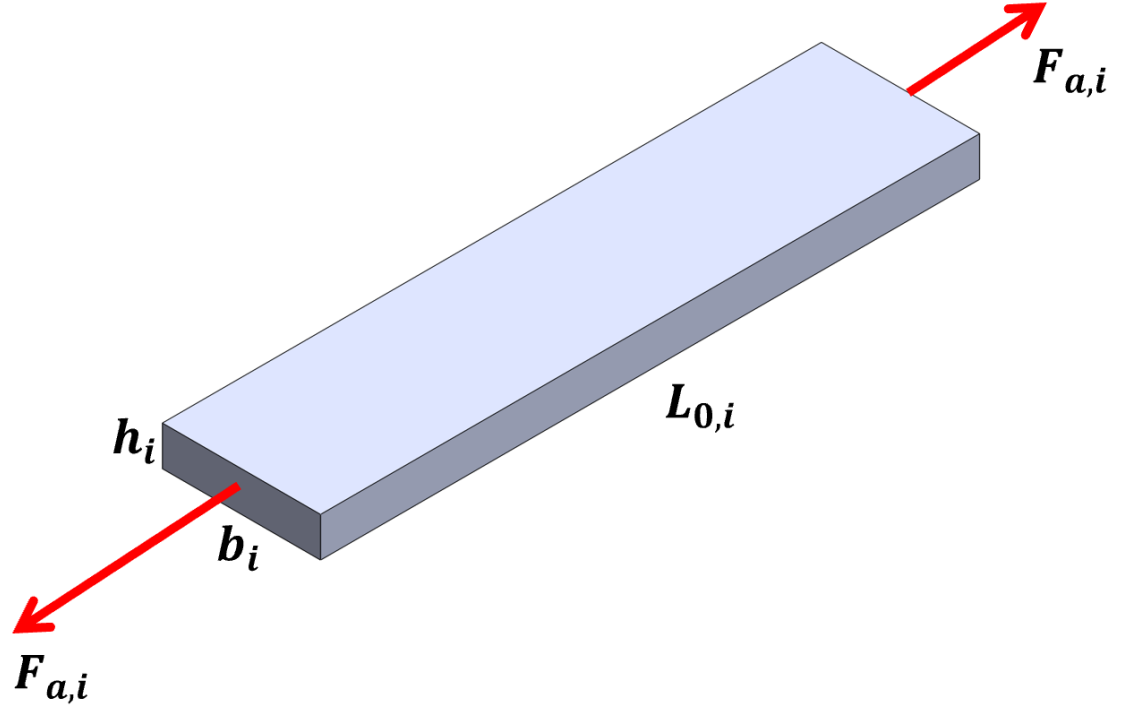
Figure 2.6: Spring element geometry and applied forces

The spring element is made of 3D-printed TPE, which is a blend of a thermoplastic and an elastomer, as mentioned in the introductory section. Plastics and elastomers alike exhibit nonlinear stress-strain relationships, and therefore the equation for a linear spring is not sufficient for analyzing this spring element. Instead, the relationship must be derived for the i-th finger from Equation (2.14), where $\sigma_{a,i}$ is the axial stress, $\epsilon_{a,i}$ is the axial strain, and $\sigma(\epsilon_{a,i})$ is the general relationship between the axial stress and the axial strain. For a linear spring, this relationship is

simply the constant E, denoting Young's modulus. The relationship of axial stress to axial strain in 3D-printed TPE is not present in the literature and will be determined in Chapter 3.

$$\sigma_{a,i} = \sigma(\epsilon_{a,i}) \qquad (2.14)$$

Therefore, the axial strain must be determined in order to find the axial stress. Axial strain of an element loaded in the direction of its major axis is defined in Equation (2.15), where ΔL_i is the displacement of the element for the i-th finger and L_0 is the initial length of the element for the i-th finger.

$$\epsilon_{a,i} = \frac{\Delta L_i}{L_{0,i}} \qquad (2.15)$$

The initial length of the element $L_{0,i}$ is a design input of the spring element and must be chosen. The displacement of the element ΔL_i, however, is determined by the desired position of the finger once the spring element is attached to the finger and producing force. This position is characterized by a set of desired correction joint angles determined by the clinician. The calculation of the displacement is shown in Equation (2.16), where $\theta_{c,ik}$ is the correction joint angle of the k-th joint on the i-th finger.

$$\Delta L_i = \sum_{j=1}^{3} r_{ik} \theta_{c,ik} \qquad (2.16)$$

The axial stress of an element with rectangular cross-section that is loaded only along its major axis is defined in (2.17), where $F_{a,i}$ is the axial force applied to the element on the i-th finger and $A_{cs,i}$ is the cross-sectional area of the element on the i-th finger. Note that the axial force on the spring element is equivalent to the required force from the moment balance in Equation (2.13). Therefore, the cross-sectional area of the element can be solved for, shown in Equation (2.18).

35

$$\sigma_{a,i} = \frac{F_{a,i}}{A_{cs,i}} = \frac{F_{sp,i}}{A_{cs,i}} \tag{2.17}$$

$$A_{cs,i} = \frac{\sigma_{a,i}}{F_{sp,i}} \tag{2.18}$$

The rectangular cross-section of the spring element has dimensions noted in Figure 2.6, where b_i is the base length for the band on the i-th finger, and h_i is the height for the band on the i-th finger. The cross-sectional area is determined by these dimensions in Equation (2.19).

$$A_{cs,i} = b_i h_i \tag{2.19}$$

Aside from the constraint determined by Equation (2.19), there appear to be no other restrictions on the base and height of the spring element's cross-section with respect to engineering analysis. Other considerations for these dimensions are given in Chapter 4.

2.6 Algorithm Structure

The algorithm used to determine appropriate spring element geometry for a set of input parameters concerning the hand geometry and grip strength of an individual person is a key component of this study. The model, its governing equations, and its assumptions are the building blocks of the algorithm. As a summary of the chapter, the algorithm's pseudocode is presented in Appendix A.

3 3D-Printed Material Testing

3.1 Introduction

The material used in this study is a thermoplastic elastomer (TPE), which is a combination of a thermoplastic and an elastomer. Both material classes exhibit a nonlinear relationship between stress and strain. The material is fabricated via the 3D printing process discussed in the introductory sections. To understand this material's behavior after printing, tensile testing was performed to acquire stress-strain curves under static loading (load to failure) and cyclic loading in a specified deflection range for a specified number of cycles. A stress-strain relation is deduced for use in the algorithm discussed in Chapter 2.

3.2 Design and Fabrication Methods

The tensile specimens were designed according to ASTM D638-14 standards using the 3D modeling software Autodesk Inventor (Standard Test Method for Tensile Properties of Plastics 2015). Dimensions of the specimens used in the tests are shown in Figure 3.1.
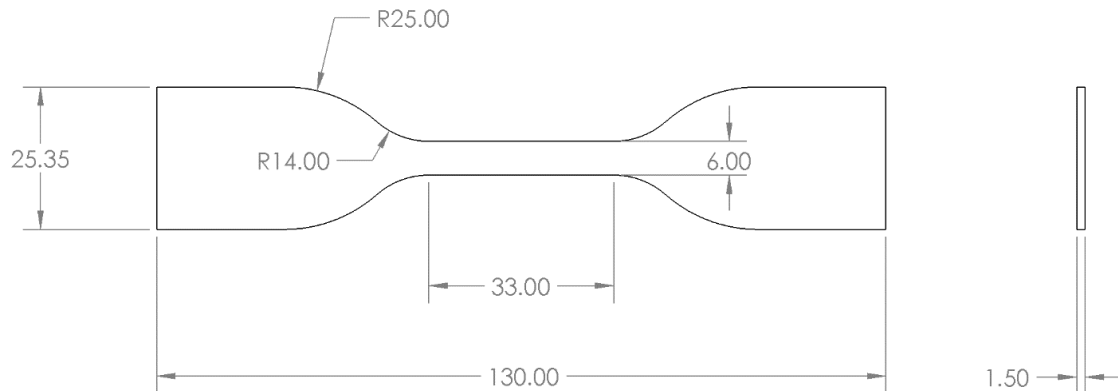
Figure 3.1: Tensile specimen geometry and dimensions

The 3D model of the specimen was exported as a .STL file to be used in the slicer software, Simplify3D. Simplify3D, like other similar programs, allows the user to import 3D objects into a workspace that represents the workspace of the 3D printer. The objects imported into Simplify3D could be copied, rotated, translated, scaled, and arranged on the workspace's bottom (print bed) to the user's liking. The interface showing the working volume is shown in Figure 3.2.
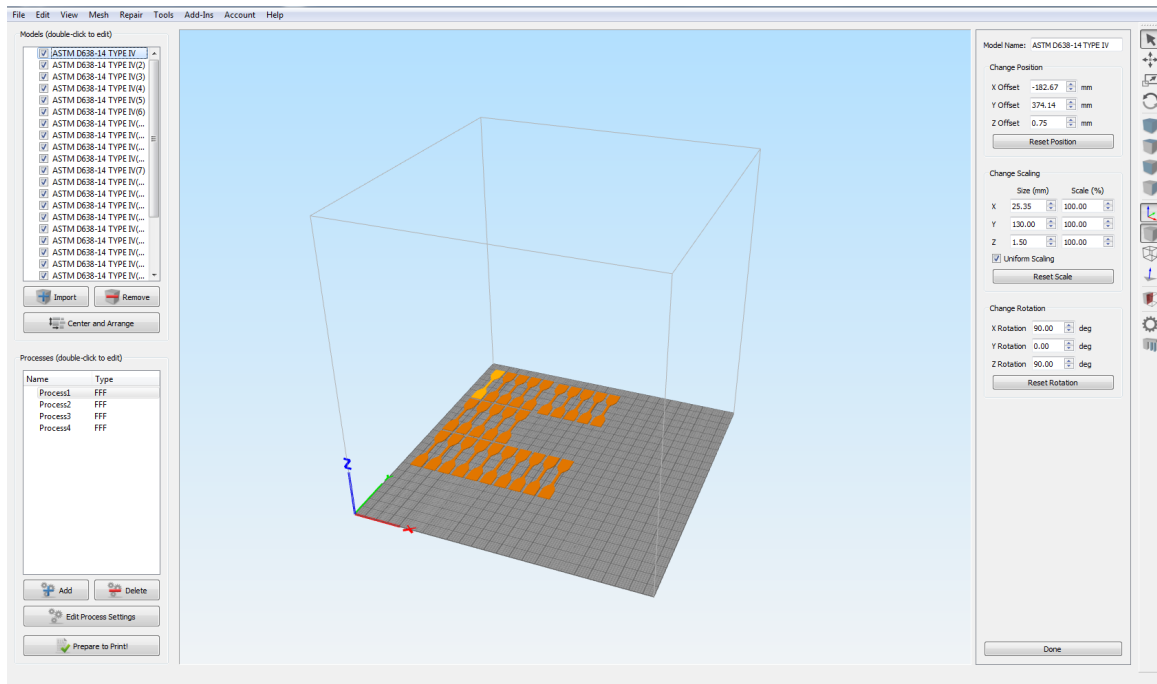
Figure 3.2: Workspace with print bed and object controls within Simplify3D slicer software

The program also provided a large number of print process settings that dictate details of the printing process being set up. Some of these settings are common with many software packages similar to Simplify3D, including extruder temperature, print bed temperature, printing speed, options for supports and rafts, and more. Simplify3D also provides more specialized settings such as extrusion rate, layer-specific settings, infill details, and more. This allows the user to fine-tune the print process to fit the requirements of the printed part.

In this experiment, specimens were to be printed to mimic appearance and properties of specimens that were fabricated via traditional manufacturing methods, such as injection molding. Therefore, the print settings included a 100% infill of the part. However, the infilling of the part during printing can be done in various patterns and directions. Some examples of print infill geometry are shown below. A rectilinear infill pattern is shown in Figure 3.7. A honeycomb pattern is shown in Figure 3.4. The grid infill pattern is shown in Figure 3.5. A triangular infill pattern is shown in Figure 3.6. An infill pattern known as a "wiggle" pattern is shown in Figure 3.7.
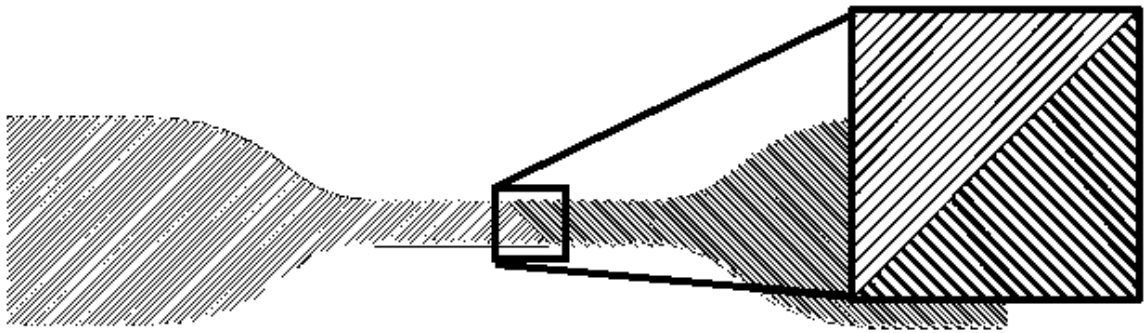
Figure 3.3: Rectilinear infill pattern
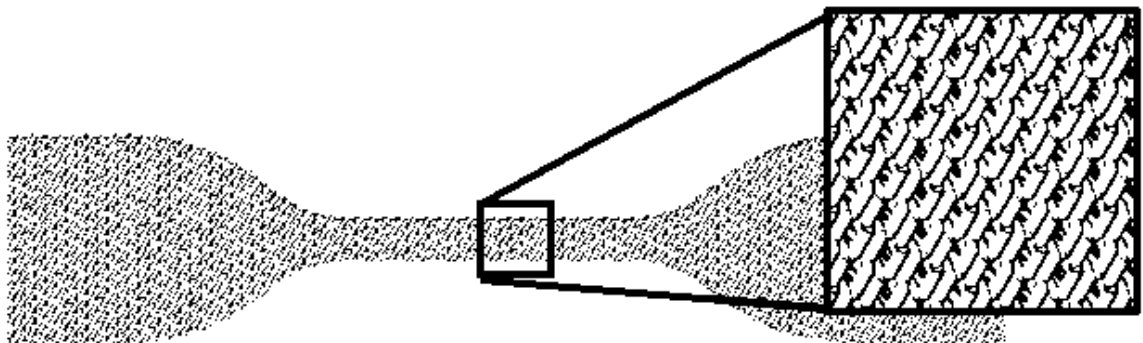
Figure 3.4: Honeycomb infill pattern

39
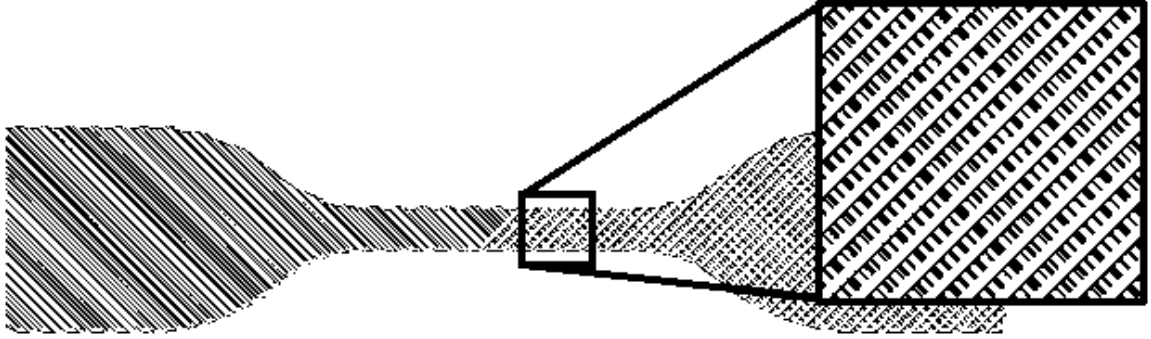
Figure 3.5: Grid infill pattern
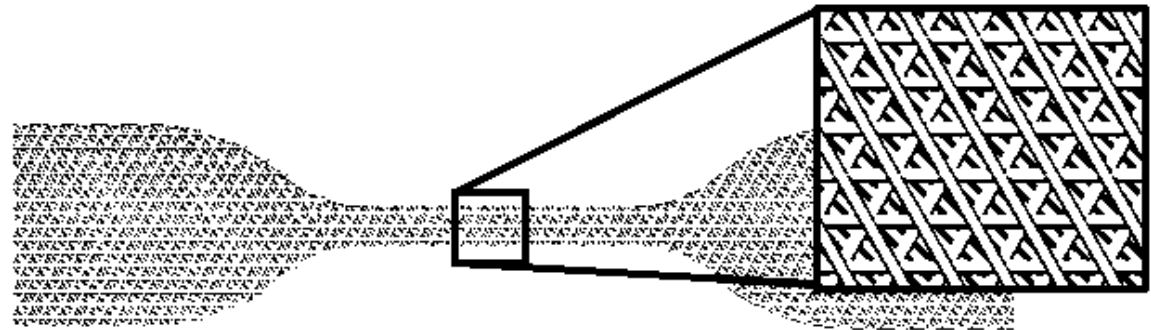
Figure 3.6: Triangular infill pattern
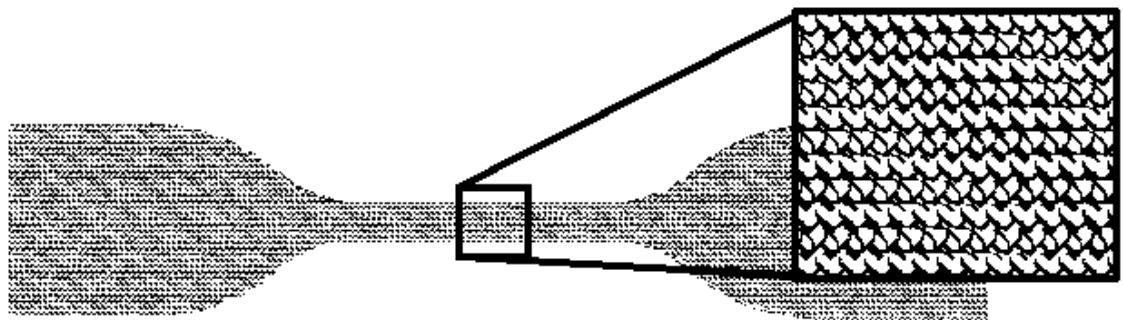
Figure 3.7: "Wiggle" infill pattern

Since this is a variable not present in injection molding of TPE, specimens were printed

using various infill geometries, all at 100% infill. The rectilinear infill pattern was chosen, and the

40

angles at which the layers would be printed at, referred to as orientation angles, were the variable. The chosen infill orientations are shown below in Figure 3.8, Figure 3.9, Figure 3.10, and Figure 3.11.
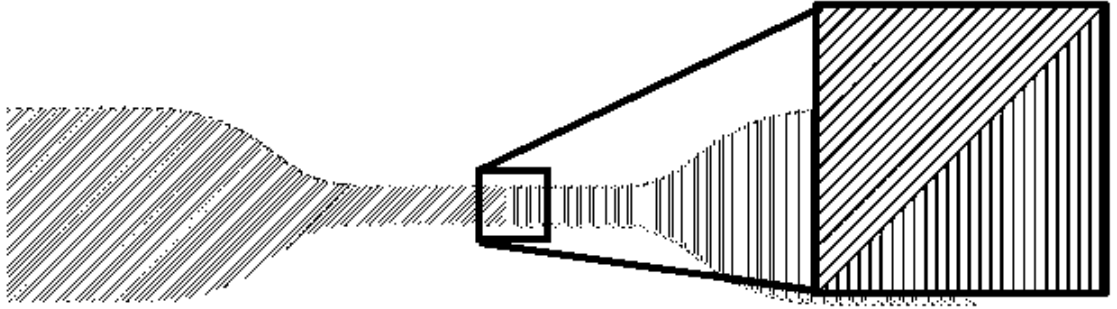
Figure 3.8: [0,45] print infill orientation
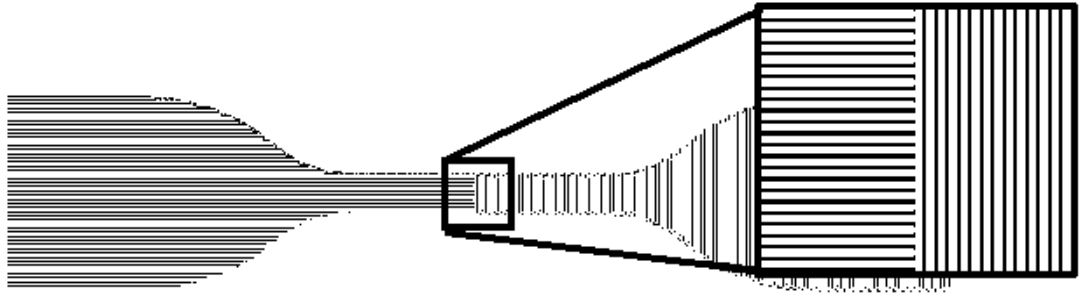
Figure 3.9: [0,90] print infill orientation
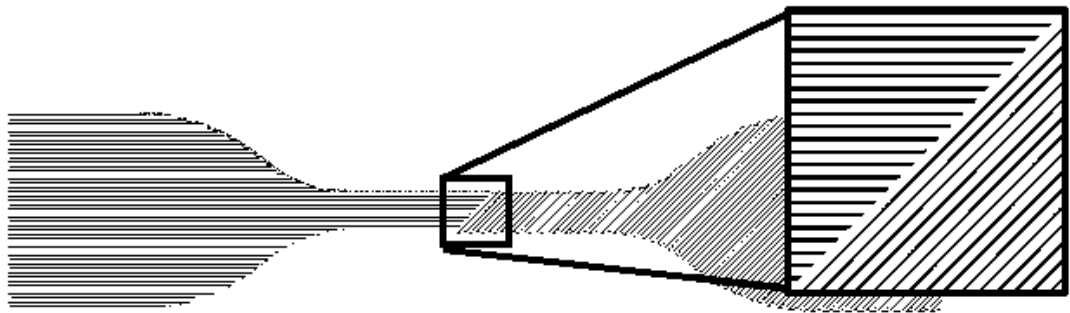
Figure 3.10: [45,90] print infill orientation
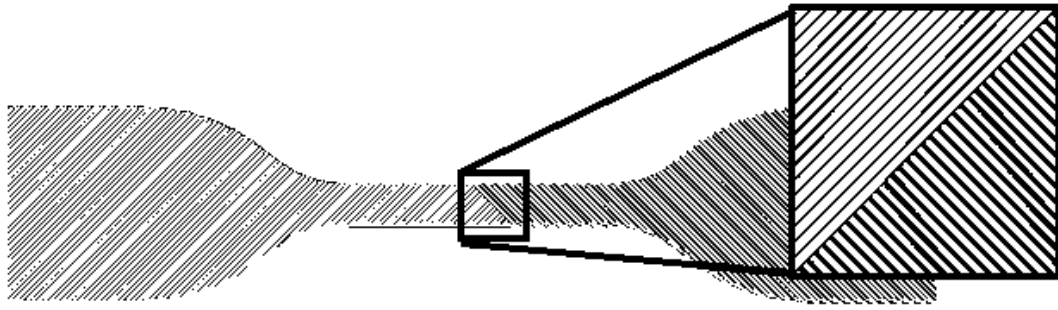
Figure 3.11: [45,-45] print infill orientation

The print settings for TPE filament were determined through adjusting the print parameters one by one until the print quality was acceptable, loosely defined as good first layer adhesion to print bed, good inter-layer adhesion, and minimal print defects while maintaining print speed and resolution. A list of key print settings used within the Simplify3D slicer software for the chosen TPE are listed in Appendix B: Simplify3D Printer Settings for TPE. A screenshot of the print setting interface is shown in Figure 3.12.
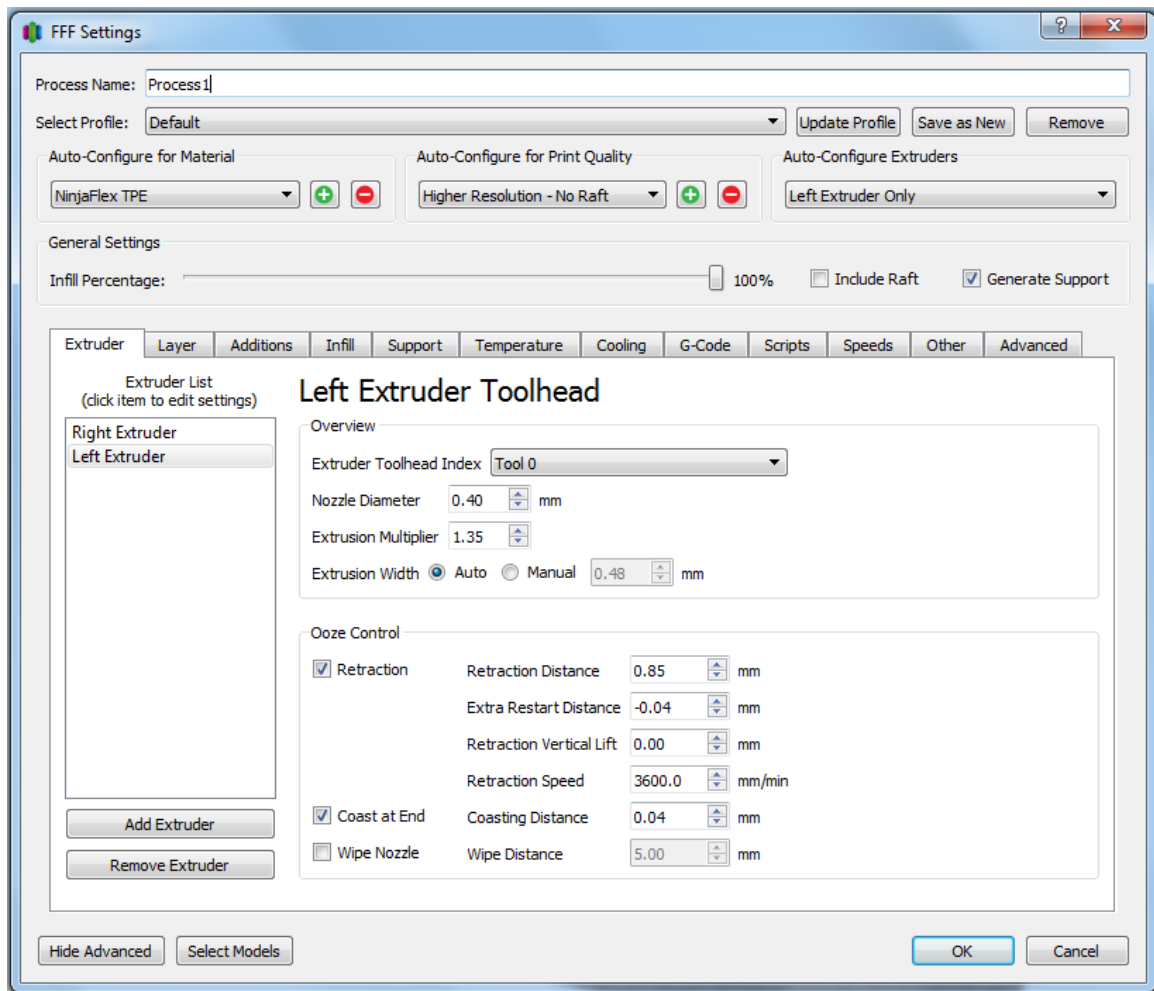
Figure 3.12: Print setting interface within Simplify3D slicer software

Once the print settings were entered and the user clicked the "Prepare To Print" button,

Simplify3D provided a preview of the entire printing process, including tool paths and speeds for

part material and any additional material including supports, rafts, skirts, and so on. The

simulation also noted material usage, print cost, estimated duration of print. The user has the

option to also see the process from start to finish by hitting the "Play/Pause" button at the bottom

of the interface. This allows the user to see how the print will execute, as well as go back to the

settings interface and make any necessary changes. Once the user is ready to print, the printer

information is exported as a g-code file to either an external drive or directly to the printer if the

computer is connected to it via USB. The print preview interface is shown in Figure 3.13. In this study, the g-code file was saved onto a micro-SD card.
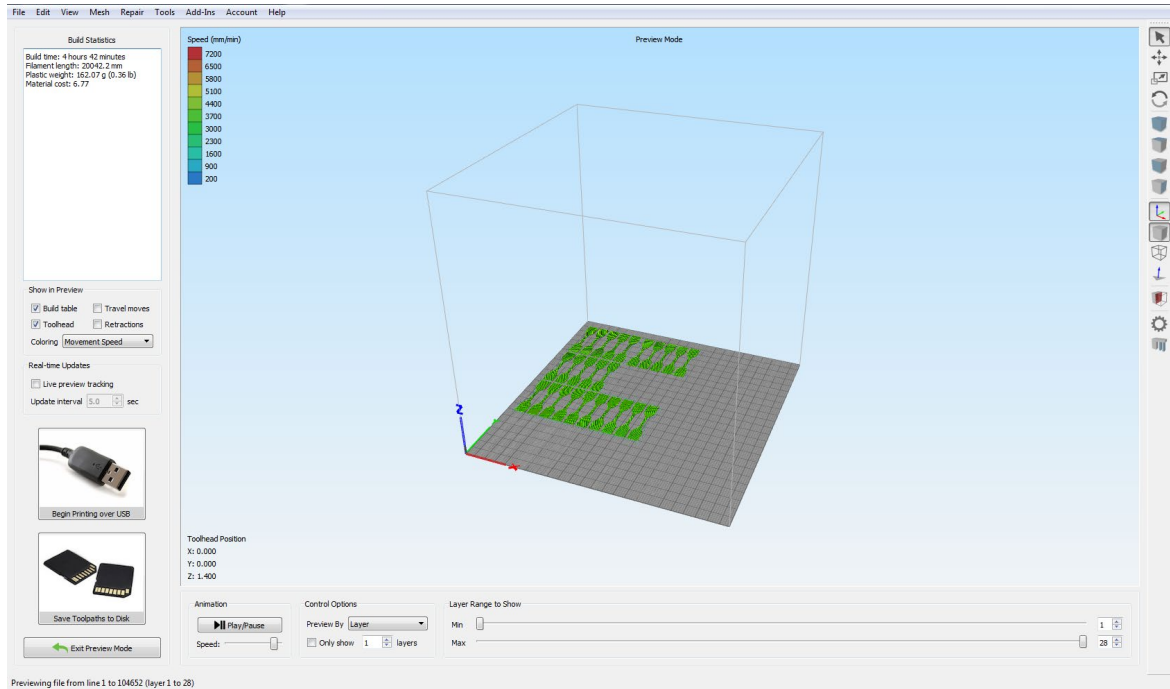
Figure 3.13: Print preview interface within Simplify3D slicer software

Fabrication of the TPE material was carried out by a Gigabot XL 3+ FFD printer manufactured by re:3D Inc., shown in Figure 3.14. The micro-SD card was inserted into the printer's Viki 2.0 LCD panel, from which the g-code file was selected on the LCD screen using the panel's click-wheel and the print was started.
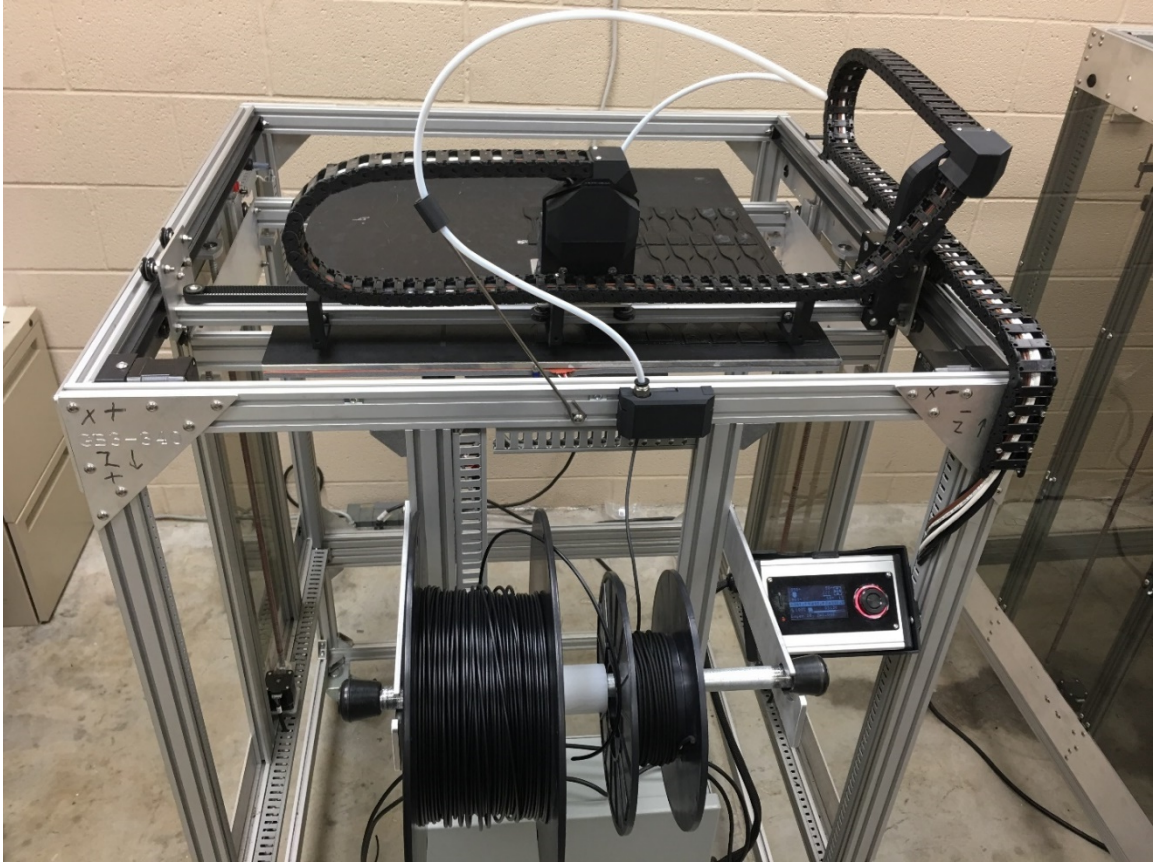
Figure 3.14: Gigabot XL 3+ printer

After the print was finished, any excess material was removed, as a final preparation for testing.

3.3 Testing Procedure

Three types of tests were carried out for the purpose of quantifying material behavior of the chosen 3D-printed TPE: tensile tests (to failure), cyclic loading tests within a specified extension range, and cyclic loading tests with various extension ranges. The tensile test to failure was chosen to determine material behavior and properties through the full range of loading before failure. The cyclic test within the specific extension range was chosen to determine material behavior and properties within the operating range of the band, determined to be

between 25mm and 40mm. The cyclic test with various ranges aimed to establish an elastic or nearly-elastic region of the material's stress-strain curve. All tests were conducted on an Instron 3345 Single Column Universal Testing System (SN: 3345B13274) shown in Figure 3.15. The system was fitted with mechanical wedge action grips, which automatically increase in gripping force as the specimen is loaded. The grips are also shown in Figure 3.15. The tests were controlled using Instron Bluehill 3 testing software.
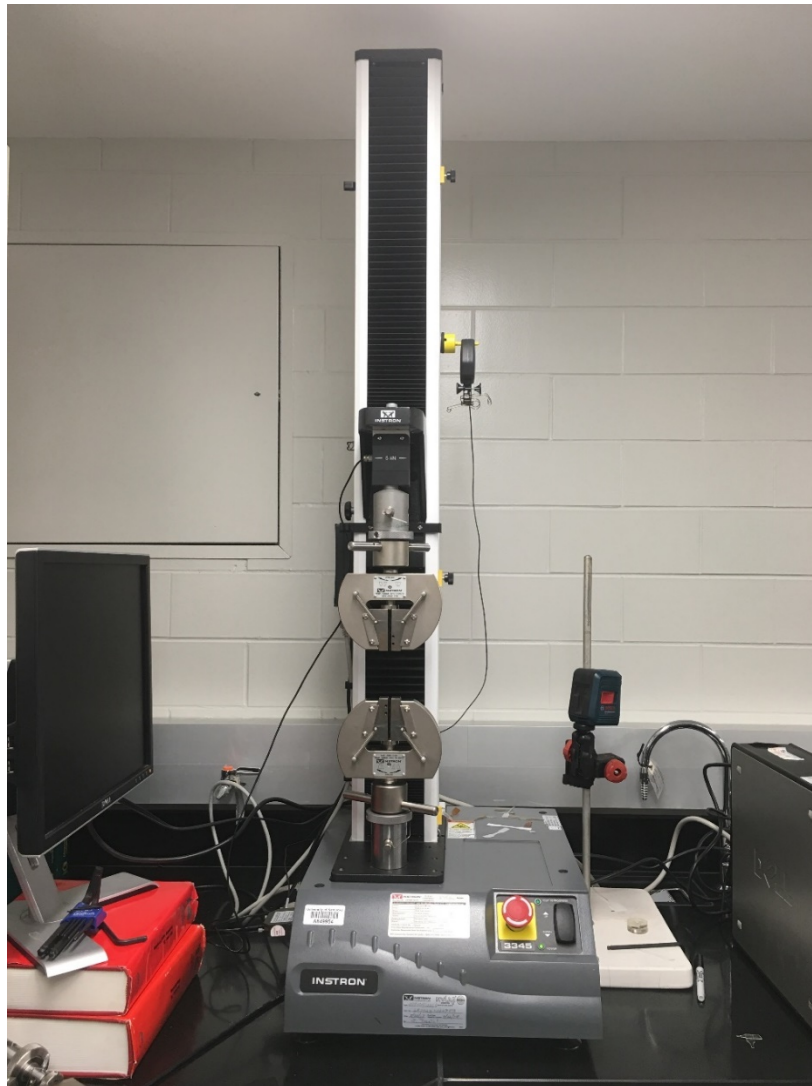
Figure 3.15: Instron 3345 Testing System with mechanical wedge action grips

3.3.1 Tensile Testing Procedure

The first type of test conducted was a tensile test to failure of the specimen. The Instron

Bluehill 3 software was opened, providing control to the Instron testing system both from the

computer and from the machine itself. The load cell was calibrated at the beginning of each

testing session. Per ASTM D638-14, the wedge grips were moved such that the distance between

them was 65 mm. The distance between the grips was measured and verified using a digital

Vernier caliper. The test setup was initiated within the Bluehill 3 software. The user was able to

choose from a variety of different default test methods for tensile testing, compression testing,

and others, or the user could create their own test method. Here, test method refers to the list of

testing parameters, prompted inputs, output data and save location, among other preferences. A

simple test method was designed and chosen. Specimen geometry and tensile testing parameters

per ASTM D638-14 standard was entered. Test parameters entered are shown in Table 3.1. The

test was specified to end once the force dropped rapidly, which occurs during specimen failure.

Table 3.1: Tensile test to failure input parameters

Parameter	Value
Length (mm)	65
Width (mm)	6
Thickness (mm)	1.5
Extension Rate (mm/min)	80
Sampling Rate (samples/second)	10

The tensile specimen was loaded into the mechanical wedge grips, loading the specimen

into the bottom grip before loading into the top grip. Since TPE experiences large strains during a

tensile test to failure, 240-grit sandpaper (P280) was cut to size, folded in half, and inserted at all

interfaces between specimen material and wedge grip. The sandpaper setup is shown in Figure

3.16.
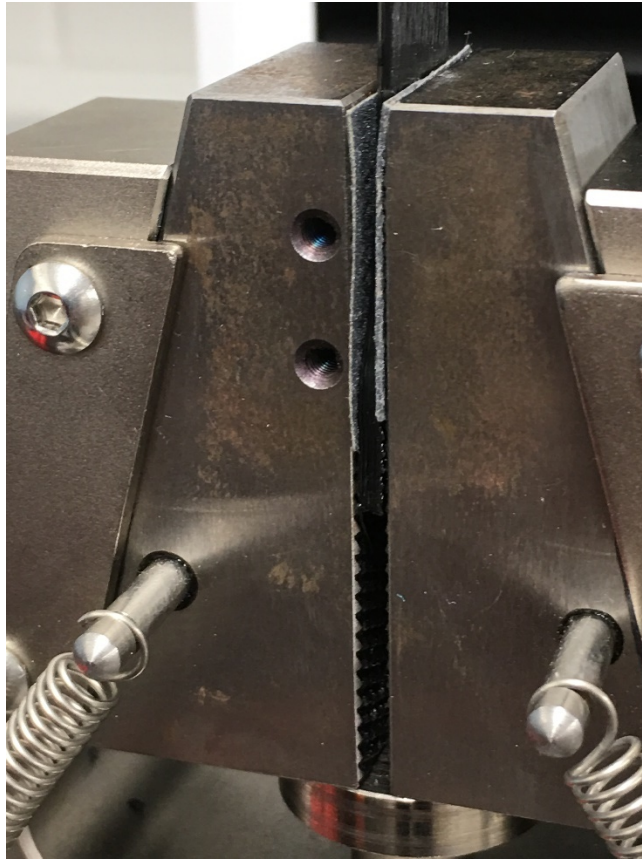
Figure 3.16: Specimen install using 240-grit sandpaper to prevent slipping at high strains

The wedge grips were tightened by hand until it became difficult to tighten any further

using the handles shown in Figure 3.15. The sandpaper and tight grip ensured no slipping would

occur during loading of the specimen, even at high strains. Once the specimen was loaded, a final

prompt on the screen allowed for verification and for any changes in geometry or extension rate

to be entered, as shown in Figure 3.17. The values entered into this prompt screen are shown in Table 3.1.

Figure 3.17: Pre-test prompt for specimen geometry and extension rate within Bluehill 3 software

Once all geometry data and the extension rate were set and verified, the "Start" button in the top right of the screen was clicked to initiate the test. The software recorded raw data including force and extension and plotted a graph of the data in real time. The graph during a test is shown in Figure 3.18.
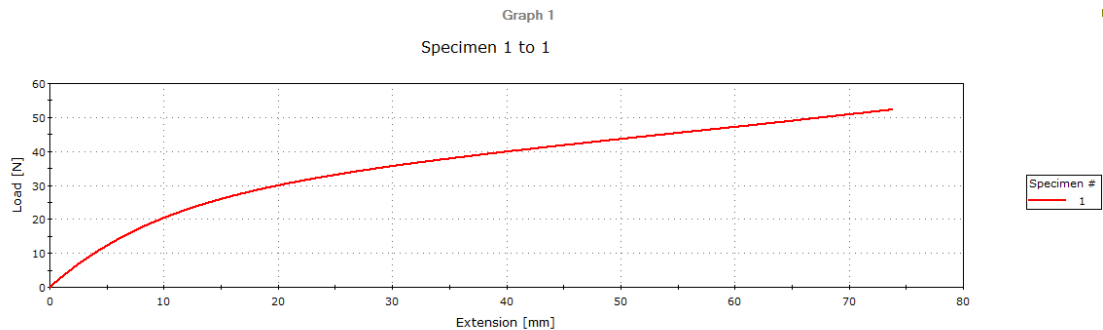
Figure 3.18: Force v. extension graph made in real-time during tensile test within Bluehill 3 software

When the specimen failed, the software ended the test and the raw data was exported to a flash drive. The "Return" button, shown in Figure 3.18 as the third button from the top on the right blue side panel, was pushed to return the top grip to its original position. The specimen was removed from the grips and labeled for future reference. The sandpaper pieces were set aside for reuse in other tests. The test was repeated for each of the four different infill orientations, with five samples for each.

3.3.2 Cyclic Testing Procedure, Single Range

Many of the same procedure details from the tensile testing apply to the cyclic testing procedure for the specified range. However, the major key difference is that a cyclic test method was not available with this testing system. So, both tensile and compression test methods were used to create the loading and de-loading portions of a cyclic loading test, respectively. For the loading portion, the tensile test method was chosen. Specimen geometry and tensile testing parameters per ASTM D638-14 standard was entered. An extension rate of 80 mm/min was entered, with a sampling rate of 10 Hz. However, instead of a force drop indicating the end of the test, an extension of 40mm was specified as the test end indicator. The Bluehill 3 software again recorded raw data including the extension and force. Once the tension test ended, the loading portion of the cycle was complete. Then, a new compression test was started in the Bluehill 3 software, serving as the de-loading portion of the test. This test method was created with the same specimen geometry, testing parameters, and sampling rate as the tensile test. However, the test was specified to end once the compression distance reached -25mm. Note that this is a negative value because, in a compression test, the top head of the system moves downward and extension is recorded as positive in this direction. However, because tensile extension up to 40mm was conducted prior, the compression test read -40mm once the compression test was

started. This is simply a sign convention, and the overall goal of performing the de-loading cycle with an initial position of 40mm and a final position of 25mm was accomplished. The crosshead path for the first two cycles is shown in Figure 3.19 by arrows, with the extension range shown by the noted dimensions.
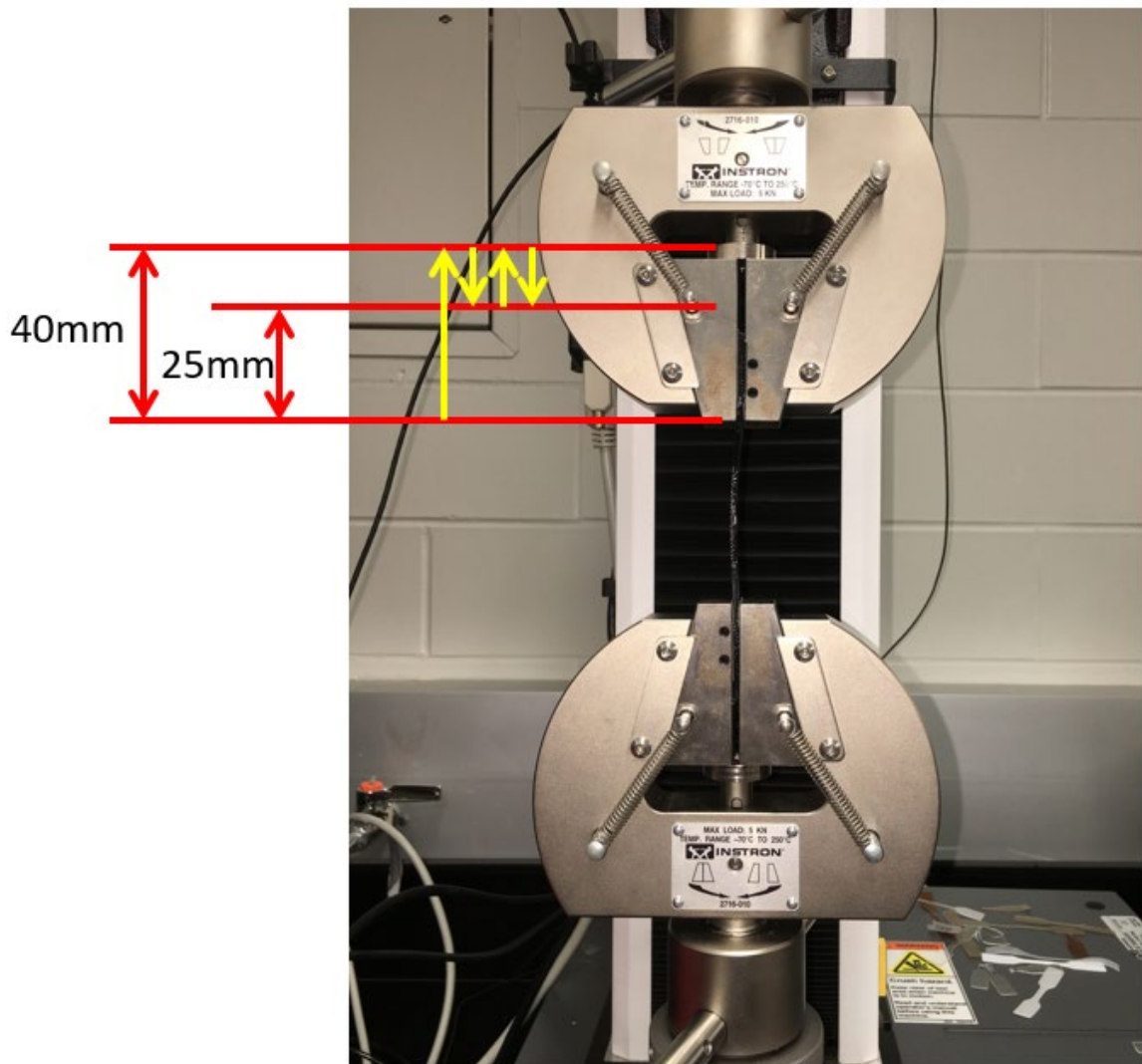
Figure 3.19: Cyclic test crosshead path showing loading and de-loading portions of two cycles

Raw data was recorded including extension and force, both now with negative signage. This process of conducting a tension and compression test constitutes a single cycle. Only the [45,-45] infill orientation was tested for cyclic loading. One sample was tested for 25 cycles.

3.3.3 Cyclic Testing Procedure, Varied Range

Cyclic testing within various extension ranges was carried out in a similar fashion to the cyclic tests concerning with a single range. Four ranges were specified to be tested, and only one sample was tested for each range. The samples were tested for only 5 cycles. The extension ranges tested are listed in Table 3.2.

Table 3.2: Extension ranges in varied-range cyclic testing

Range	Lower Bound (mm)	Upper Bound (mm)
1	15	30
2	10	20
3	5	10
4	0	5

3.4 Experimental Results

From the tensile tests, the raw data (extension and force) for each sample were exported into a spreadsheet. The raw data was taken every 0.1 seconds until the specimen failed. The averages of the extensions and forces recorded from the five samples were stored in a separate set of columns. The strain and stress were calculated from the averaged extension and averaged force, respectively, using specimen geometry specified in the ASTM D638-14. The data was plotted on a graph with the x-axis representing axial strain and the y-axis representing axial stress.

This was done for all four infill orientations, and the plots with the fit curves are shown in Figure 3.19, Figure 3.20, Figure 3.21, and Figure 3.22.
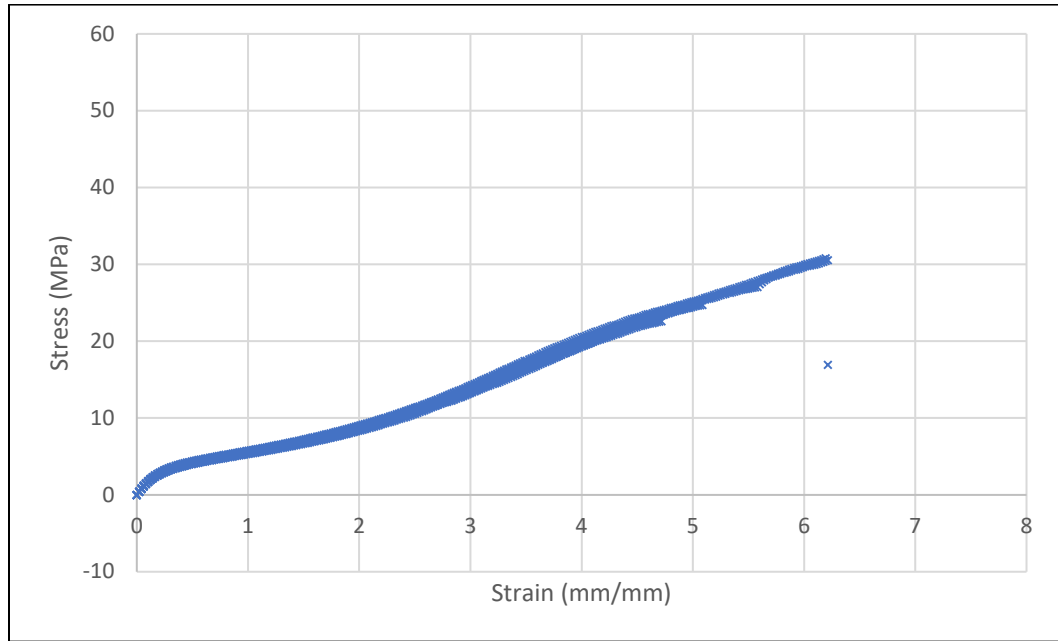
Figure 3.20: [0,45] infill orientation tensile test data points
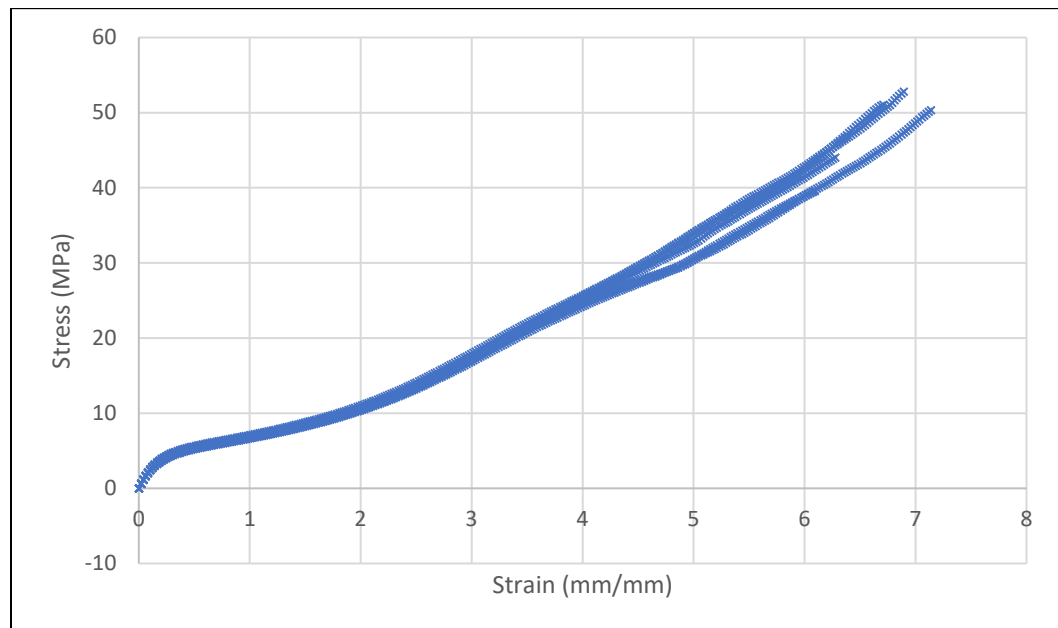
Figure 3.21: [45,90] infill orientation tensile test data points

53
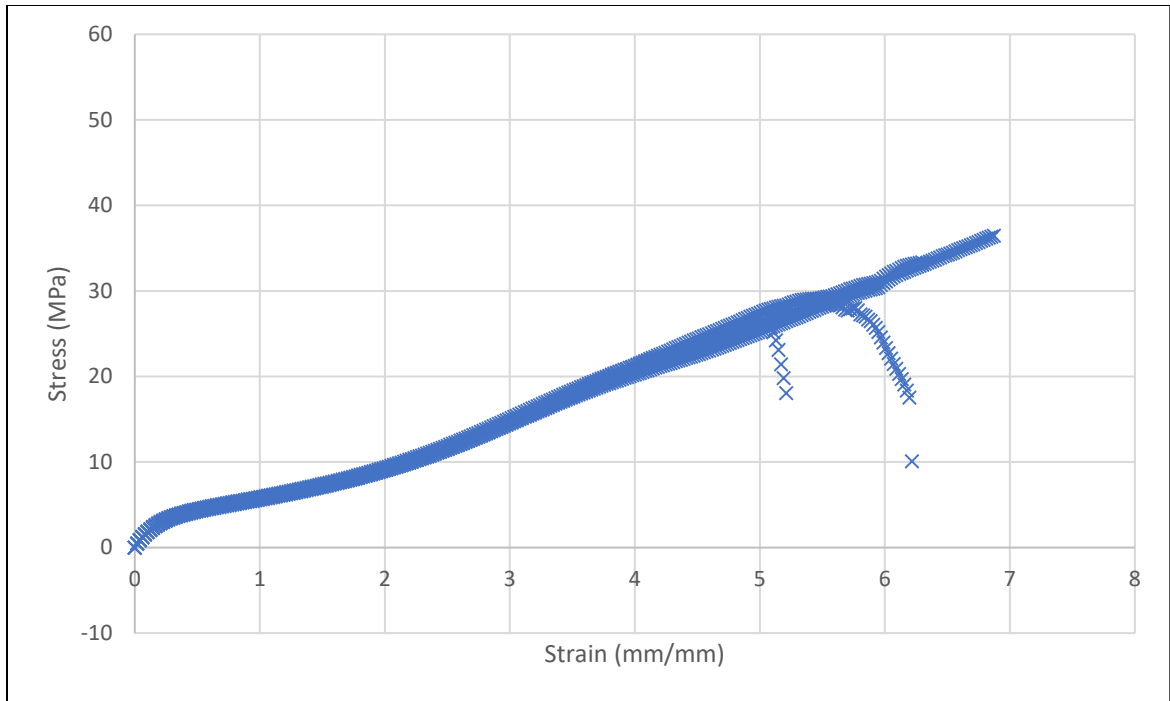
Figure 3.22: [0,90] infill orientation tensile test data points
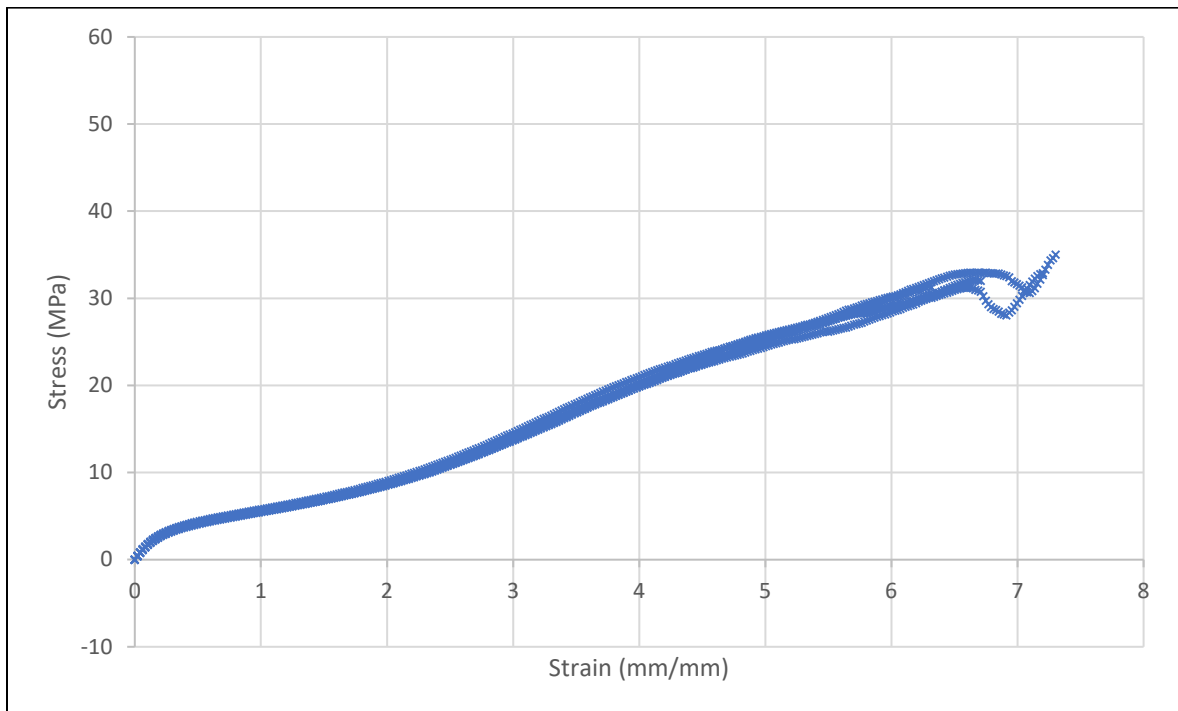
Figure 3.23: [45,-45] infill orientation tensile test data points

For the cyclic loading tests in the operating extension range, the raw data was also exported to a spreadsheet and averaged in a separate column. The stress and strain were calculated from the force and extension, respectively, and plotted on a stress-strain graph with the same axes specified in the tensile testing. The graph is shown in Figure 3.23.
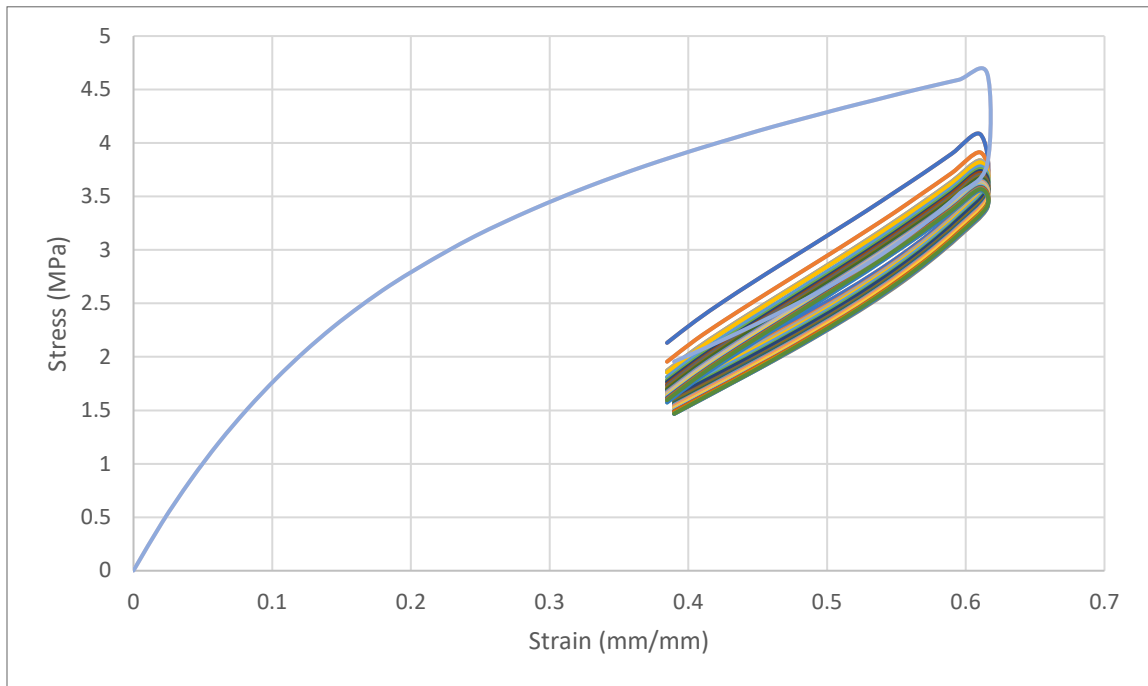
Figure 3.24: [45,-45] infill orientation cyclic test data, range [25mm,45mm], 25 cycles

The raw data from the cyclic loading tests performed at the various ranges listed in Table 3.1 also were exported to a spreadsheet. No averaging of data between samples was performed, as only one sample was tested per range. The stress and strain were calculated from the force and extension, respectively, and plotted on stress-strain graphs with the same axes as specified in the tensile testing. The graphs are shown in Figure 3.24, Figure 3.25, Figure 3.26, and Figure 3.27.
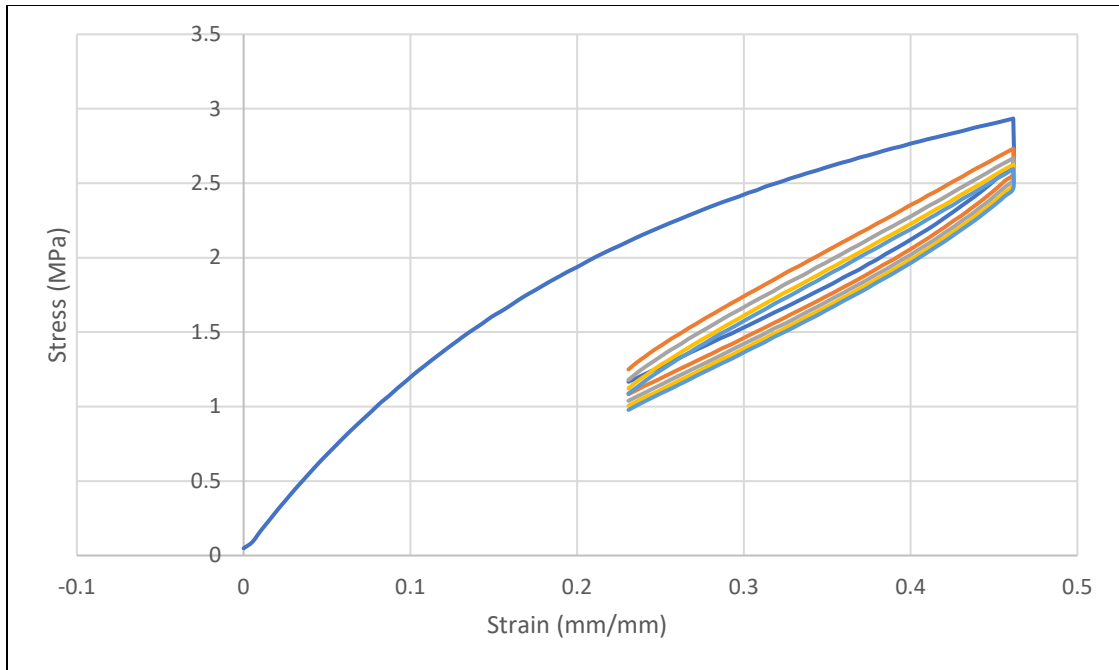
Figure 3.25: [45,-45] infill orientation cyclic test data points, extension range [15mm,30mm]
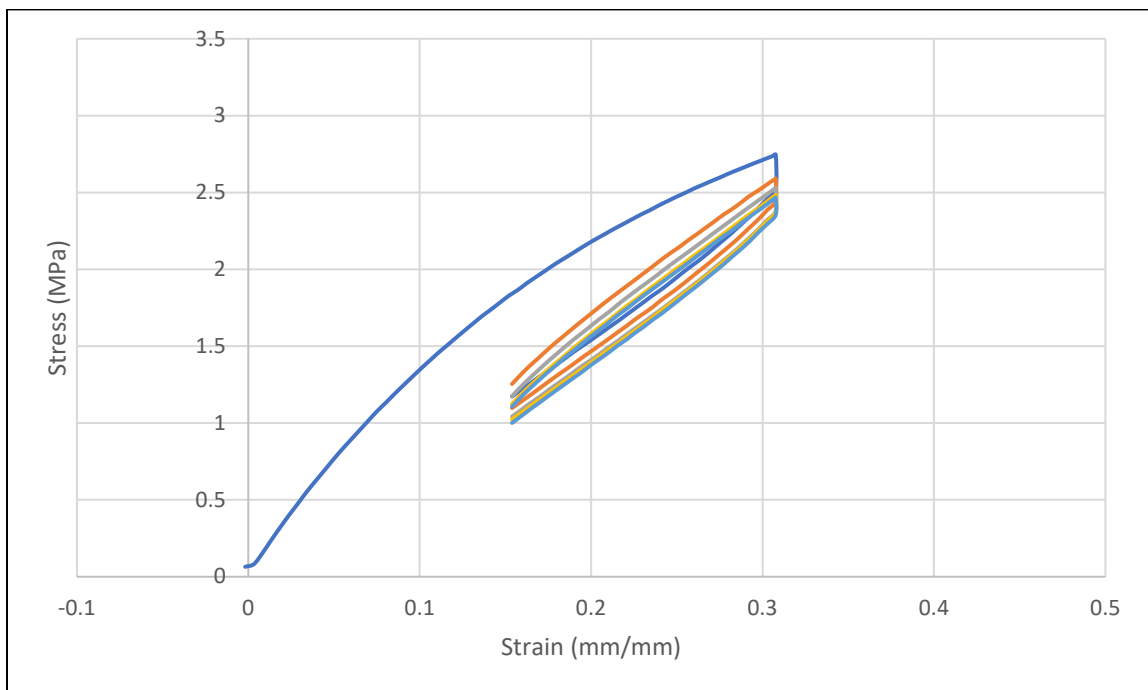
Figure 3.26: [45,-45] infill orientation cyclic test data points, extension range [10mm,20mm]
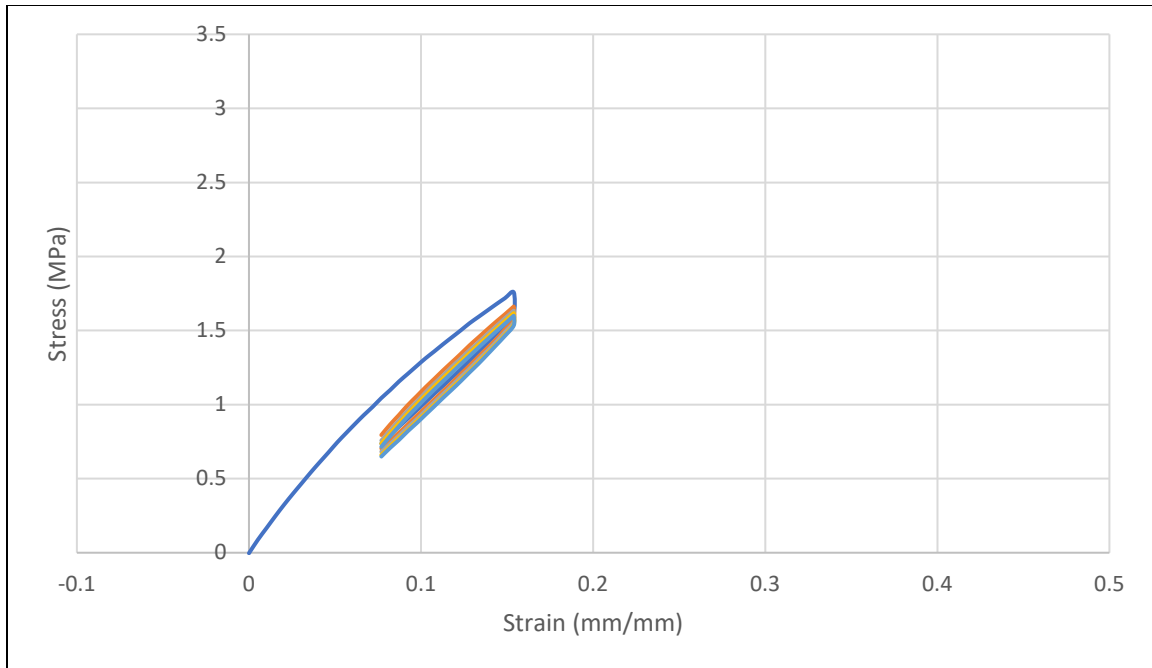
Figure 3.27: [45,-45] infill orientation cyclic test data points, extension range [5mm,10mm]
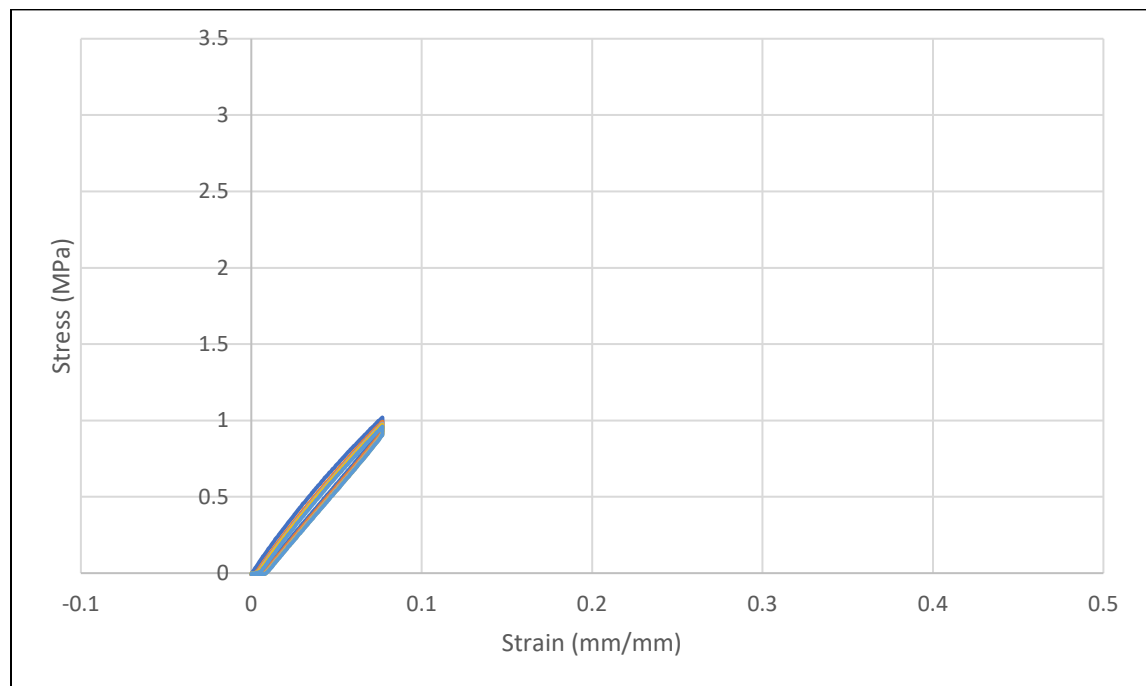
Figure 3.28: [45,-45] infill orientation cyclic test data points, extension range [0mm,5mm]

3.5   Discussion

As expected, the tensile test results showed a nonlinear relationship between stress and strain. The 3D-printed TPE material showed high levels of strain before ultimate failure, which is characteristic of TPE. Data from each sample for a given infill orientation was averaged, and a sixth-order polynomial curve was used to fit the average data up to 400% strain. This strain limit was chosen because the strain is expected to remain below this limit within this application of the material, and the data below this limit is most representative of the material. Data above this limit tended to become incomplete due to early and irregular specimen failure. These early failures could be due to irregularities in material caused by the fabrication process such as over/under-extrusion of material, printing on an unlevel or damaged section of the print bed, and damage to part during removal from the print bed. The polynomial curves for each infill orientation are shown in Figure 3.28, Figure 3.29, Figure 3.30, and Figure 3.31.
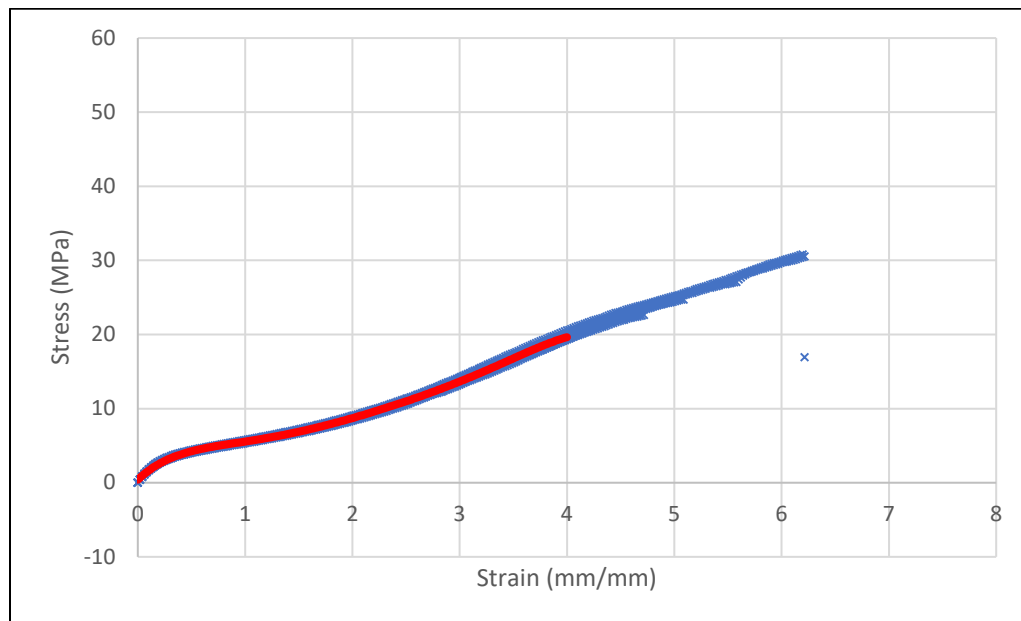
Figure 3.29: [0,45] infill orientation tensile test data points with polynomial curve fit,
$R^2 = 0.9998$
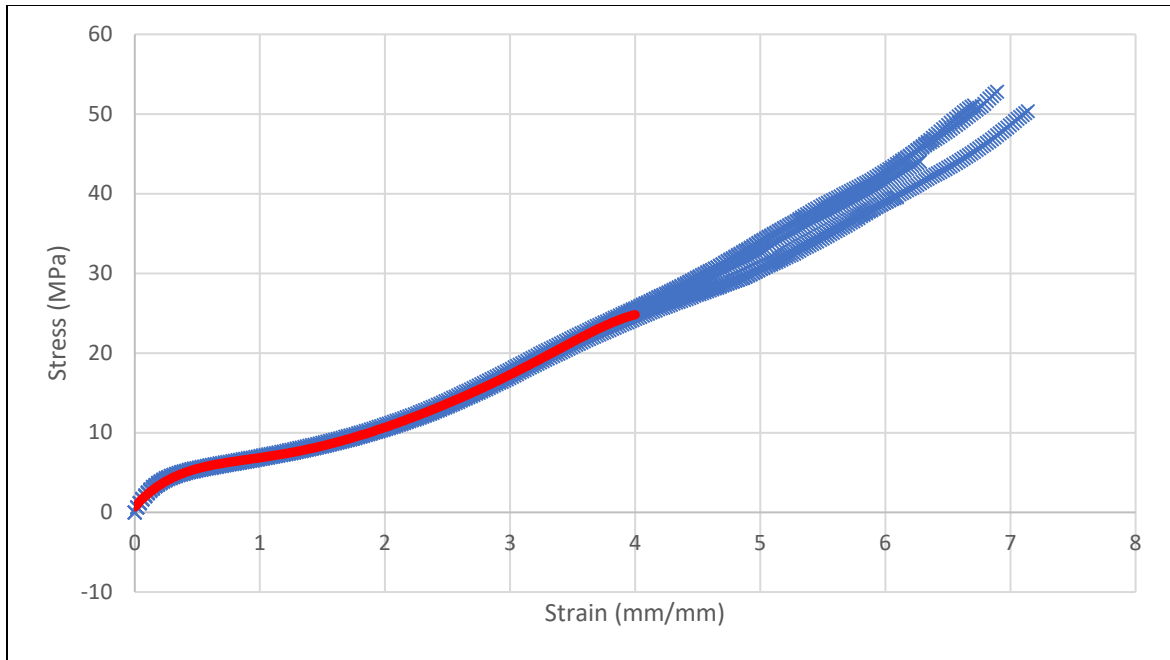
Figure 3.30: [45,90] infill orientation tensile test data points with polynomial curve fit,
$R^2 = 0.9997$
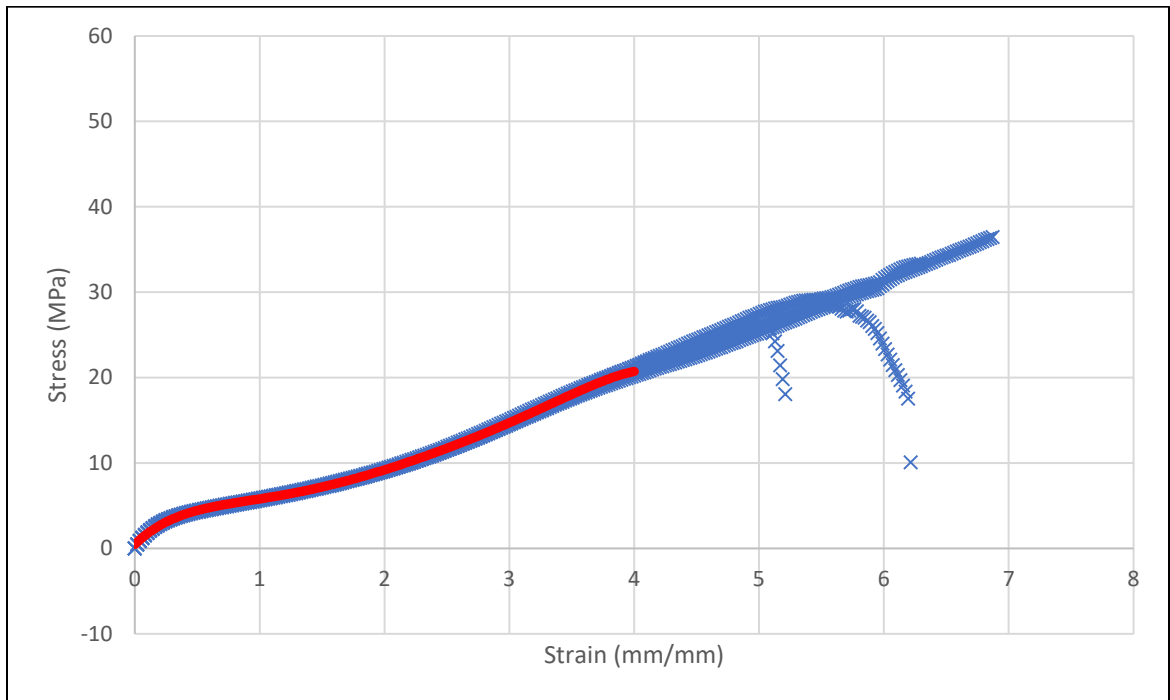
Figure 3.31: [0,90] infill orientation tensile test data points with polynomial curve fit,
$R^2 = 0.9998$
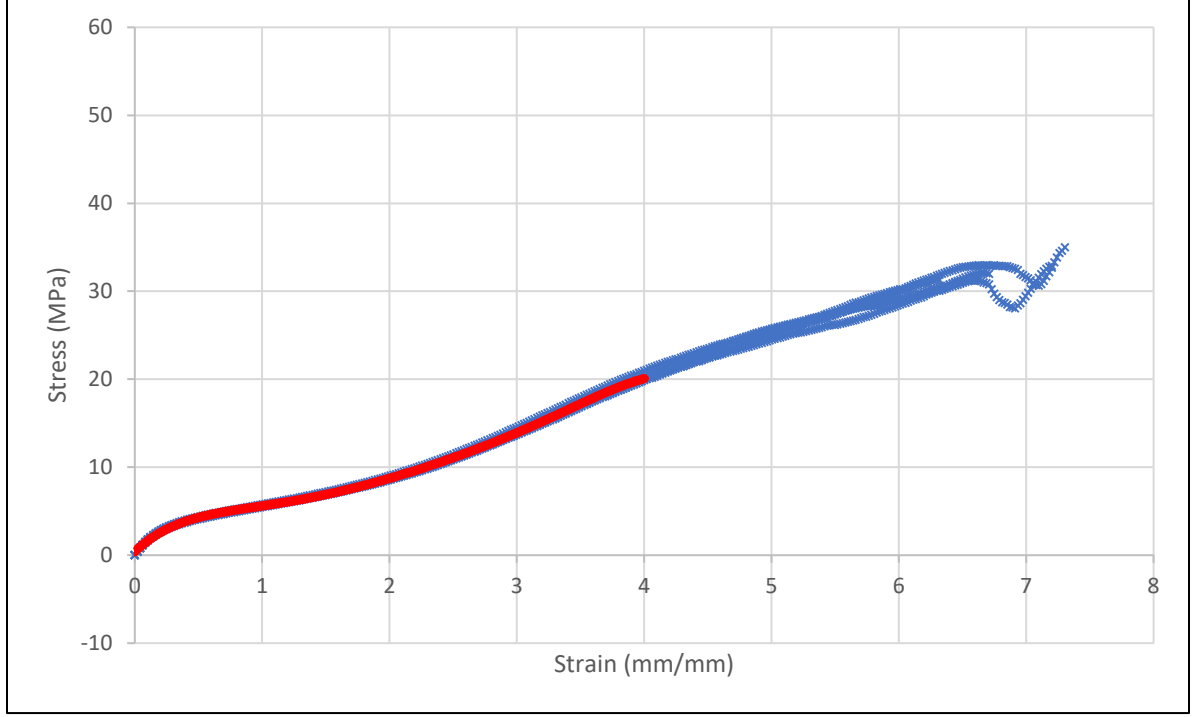
Figure 3.32: [45,-45] infill orientation tensile test data points with polynomial curve fit,
$R^2 = 0.9998$

The equations of the polynomial curves are shown in Equation (3.1).

$$\begin{bmatrix} \sigma_{[0,45]} \\ \sigma_{[45,90]} \\ \sigma_{[0,90]} \\ \sigma_{[45,-45]} \end{bmatrix} = \begin{bmatrix} -0.0662 & 0.8805 & -4.6897 & 12.705 & -17.433 & 13.75 & 0.4089 \\ -0.0897 & 1.19 & -6.3655 & 17.376 & -23.82 & 17.877 & 0.6934 \\ -0.0669 & 0.8842 & -4.7299 & 12.963 & -17.931 & 14.209 & 0.469 \\ -0.0637 & 0.8422 & -4.494 & 12.329 & -17.216 & 13.803 & 0.4054 \end{bmatrix} \begin{bmatrix} \epsilon^6 \\ \epsilon^5 \\ \epsilon^4 \\ \epsilon^3 \\ \epsilon^2 \\ \epsilon \\ 1 \end{bmatrix} \quad (3.1)$$

A plot with all four polynomial curves is presented in Figure 3.32, created within Matlab.
The code is found in Appendix C: Matlab Code For Stress-Strain Curve Plotting. From the plot, it is
observed that the infill orientations [0,45], [0,90], and [45,-45] are very similar, with infill
orientation [45,90] exhibiting nearly 30%-higher strength that the others.
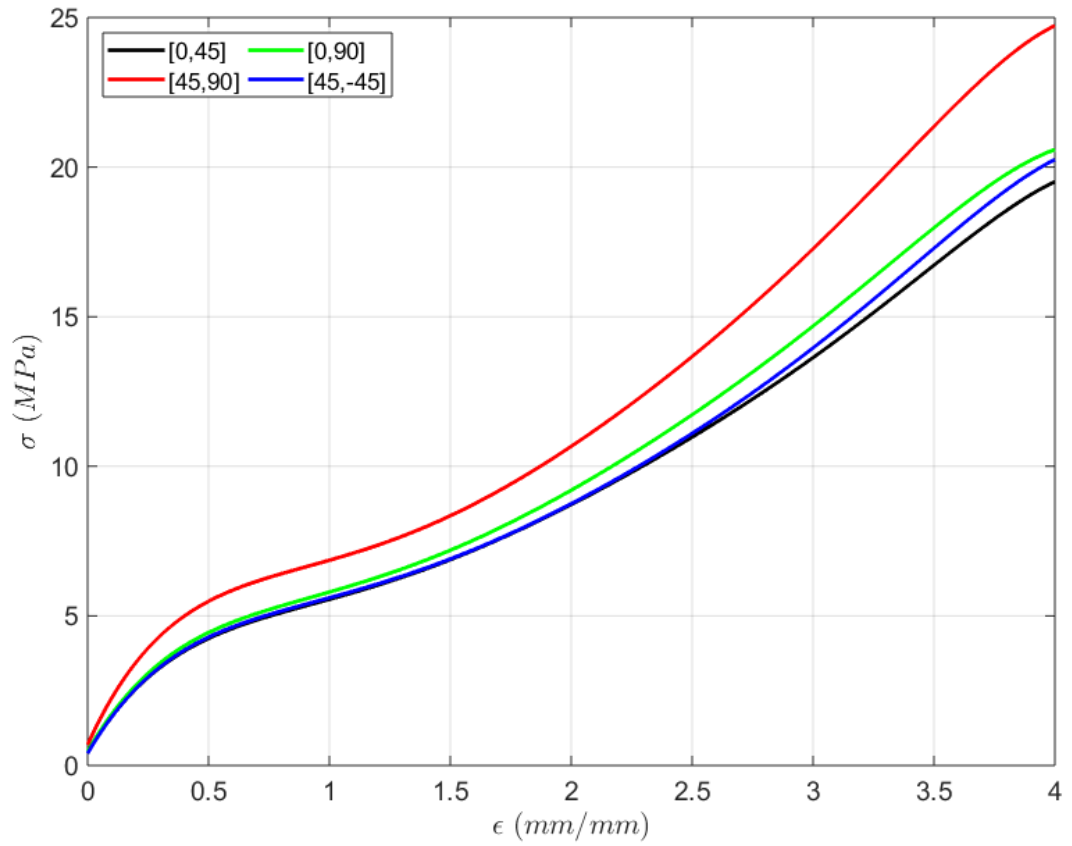
Figure 3.33: All infill orientation tensile test polynomial curves

Several factors could be used to explain the differences in the curves of the different infill orientations. It is noted that the 90° infill angle is the only angle that truly runs from the Instron machine's top grip to its bottom grip. This would likely lend to a higher strength of material, since the infill material is oriented along the same axis upon which the load is being applied. A similar phenomenon occurs in composite materials. Lamina with fibers oriented along the same axis as the applied load provide the most strength in that loading direction.

Additionally, the layers were analyzed and found to have different contact area between layers and nearly no contact area within the layers, regardless of infill orientation. Theoretically,

the contact area between two lines of material are shown in Figure 3.33 for each infill orientation.

$[0, 90]$

$[45, -45]$

$[45, 90]$

$[0, 45]$
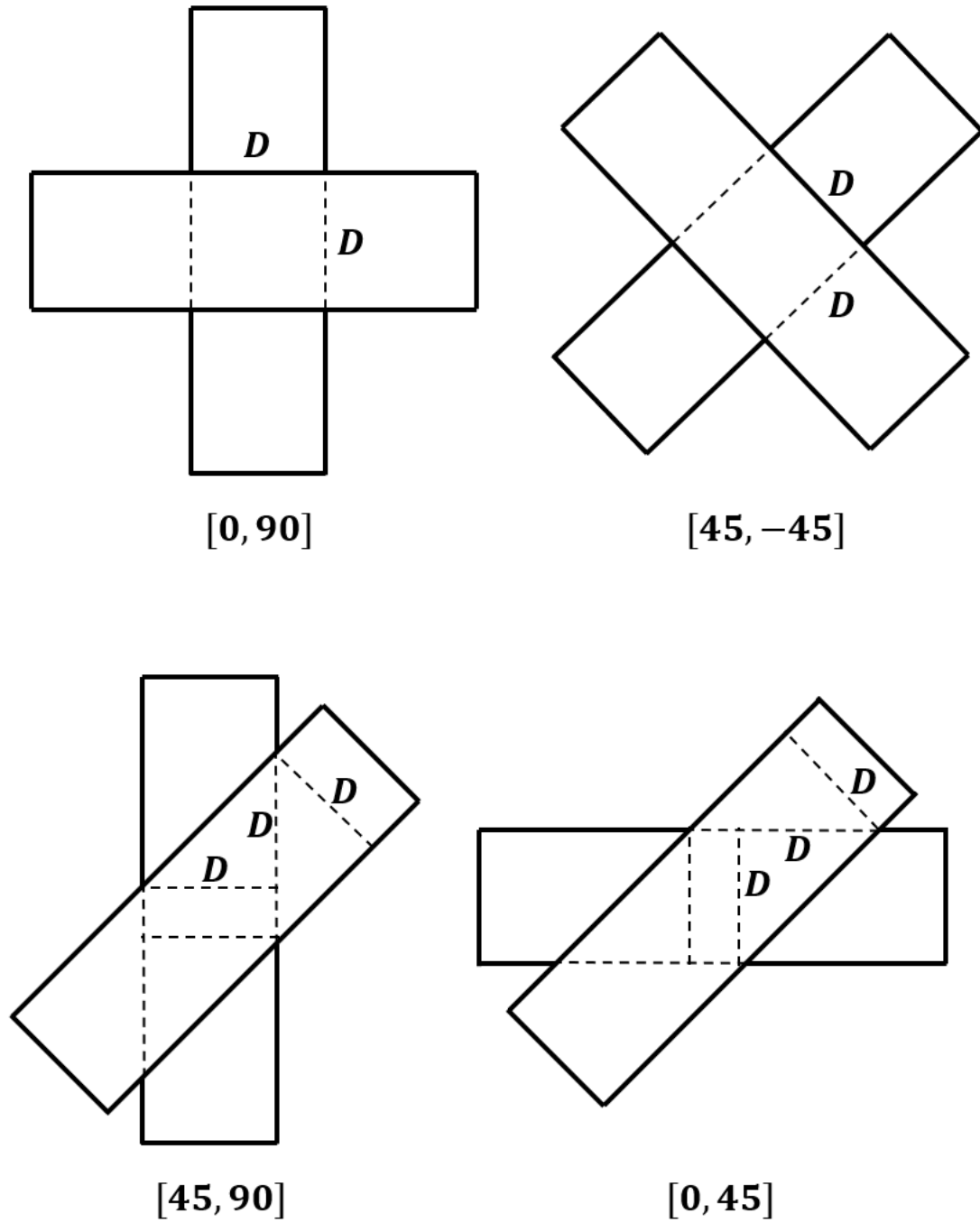
Figure 3.34: Theoretical contact area between 3D-printed lines of material from adjacent layers

The contact area for the [0,90] and [45,-45] orientations are the same, and will be referred to as A_{90}. The contact area for the [45,90] and [0,45] orientations are also the same, and will be referred to as A_{45}. The contact area A_{90} is shown in (3.2), where D represents the filament diameter after extrusion.

$$A_{90} = D^2 \tag{3.2}$$

The contact area A_{45} is a little more involved. Using basic trigonometry, the contact area is determined by Equation (3.3).

$$A_{45} = (2\sqrt{2} - 1)D^2 = 1.828D^2 \tag{3.3}$$

It should be noted that these are the maximum possible contact areas for these infill orientations, and the actual area may be a fraction of these values. Figure 3.34 shows an image of an infill layer. A layer had been removed to expose this interior layer. It is observed that the circular cross-section approximation for the infill material strands is valid. The strands have a diameter of 0.4mm, determined by the exit diameter of the extruder nozzle. Small marks or tears were also observed along the filament strands where the previous layer had been peeled away. The marks did not span the entire width of the filament surface, indicating that the material did not make maximum contact between this layer and the previous layer. The microscope used to view the specimen worked sufficiently for detailed layer imaging, but insufficiently for capturing the small marks and tears.
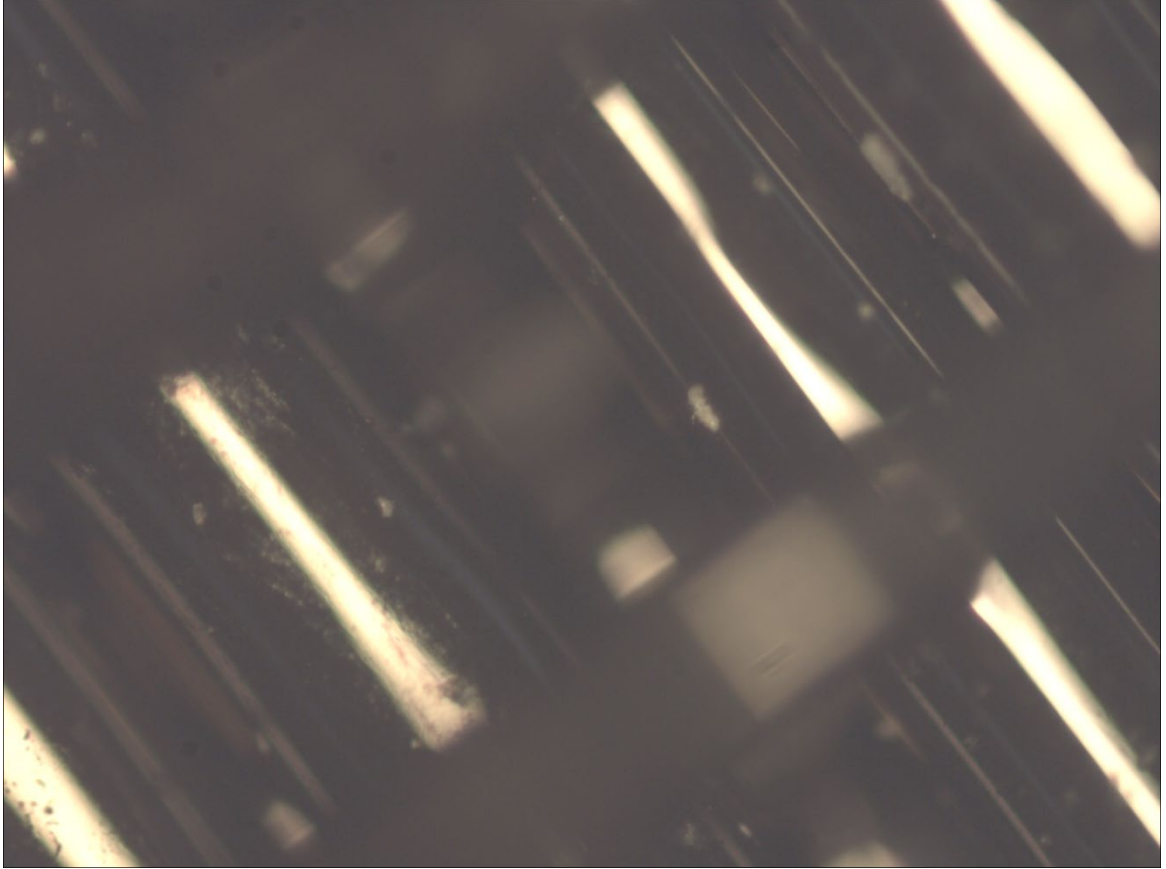
Figure 3.35: Interior infill material from tensile specimen, 5x magnification

Nonetheless, the percentage of maximum contact area would likely be the same for both

A_{90} and A_{45}, since the contact area is a product of print settings such as extrusion rate, extrusion

temperature, travel speed, and more. These settings were used across all specimens and all infill

orientations. So, the proportions would remain the same between the two contact areas, and

Equations (3.2) and (3.3) may still be used to explain differences between the bulk material

properties of 3D-printed tensile specimens with different infill orientations.

The final proposed factor for varied results from the tensile tests is the reorientation and

interactions between infill layers at high strains. The infill material strands oriented at an angle of

45° could be pulled closer to 90°, adding strength to the material as strain increased. The strands

orientated at 0° would not be reoriented but could have been compressed due to conservation of volume. This compression could have added strength to the material as well. Further tests and analysis are needed to fully understand the mechanics of this material that contribute to the bulk behavior.

The cyclic test results for the range of [25mm,40mm] shows several interesting material behaviors. First, hysteresis was shown within the range tested. Hysteresis is evidenced by a concave curve during the loading of the material, followed by a distinct and convex curve during the de-loading of the material back to its initial strain before loading. This is typical of elastomers and TPE materials. Second, plastic deformation was also seen in the tested specimen's stress-strain curve. As mentioned, TPE is a combination of a thermoplastic and an elastomer. Elastomers are considered a hyperelastic material. Hyperelastic materials are characterized by their ability to endure large deformations with full recovery of their initial shape, incompressibility, and nonlinear stress-strain relationship. However, from the cyclic testing, it is shown that TPE does not recover its initial shape. This is likely due to TPE's partial composition of thermoplastic. Plastics are named after their ability to irreversibly deform without material failure. When the TPE specimens underwent cyclic loading, plastic deformation likely caused the permanent lengthening of the specimen. This permanent deformation was evidenced by specimen folding after the Instron was reset to its initial position, shown in Figure 3.35. To see if any relaxation of the specimen occurred after the test, a tested specimen and a virgin specimen were placed side-by-side after leaving the tested specimen to sit for a day and visually compared. The comparison shows that, even if relaxation had occurred, permanent deformation was still present. The tested material and virgin material are shown in Figure 3.36. Thirdly, the stress-strain curve for this cyclic testing showed a softening of the material. The softening is most pronounced after the first cycle's

65

loading portion, shown by a large decrease in stress while being held at a constant strain. Softening can also be seen within each cycle thereafter at the extension range limits where the strains are held constant while the test method is being switched. This method changeover, which switched the test between loading and de-loading portions of a cycle, took between 20 and 30 seconds for all cycles. This shows that, while these changeover cycles were nearly constant, the first changeover in the first cycle has a more severe softening than the following cycles. This could be due to a number of factors, including the failure of weaker material strands and interlayer bonds within the material. These observations can also be seen in studies with testing of other thermoplastic elastomers (Drozdov and Christiansen 2007), (Drozdov 2007), (Scavuzzo 2000), including hysteresis loops and the softening effects found in the first cycle and in the later cycles.
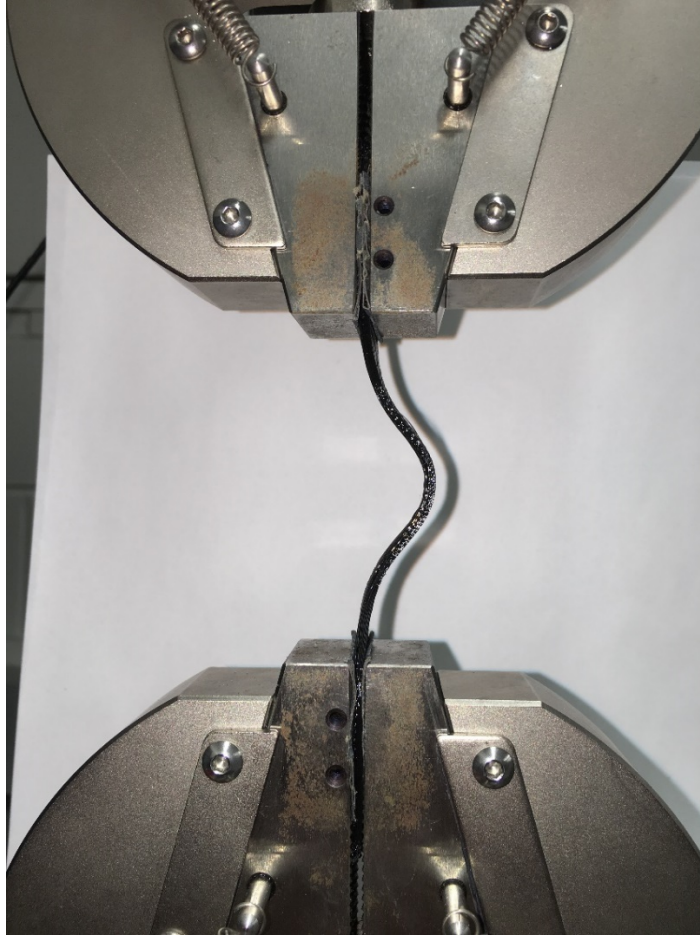
Figure 3.36: Specimen folding at Instron initial position, indicating permanent deformation

Figure 3.37: Comparison of virgin specimen (top) and specimen after 25 cycles (bottom), range [25mm,40mm]

The cyclic test results for various ranges shown in Table 3.1 show a correlation between strain and hysteresis. The [0mm,5mm] extension range had the lowest hysteresis, meaning that, while hysteresis was still apparent in the plot in Figure 3.27, the curves for each cycle remained fairly close to each other. This means that the material softened very gradually in this extension range. Increasing the extension range to [5mm,10mm] caused the hysteresis to become more pronounced, and this trend continued as the extension ranges were raised. It is also observed that most of the softening takes place within the first cycle. In the [0mm,5mm] range, this is not so easy to spot. However, as the hysteresis becomes more pronounced in the higher ranges, there is a large drop in stress experienced by the specimen between the loading portion and de-loading portion of the first cycle. After the first cycle, softening becomes much more gradual.

As mentioned, hyperelastic materials such as elastomers are revered for their ability to undergo high strains and revert back to their original shape after de-loading. TPE filament allows this elastomer material to be used in the fabrication process of FFD 3D-printing. However, from the material testing and analysis, it is apparent that the stress-strain curve of TPE shows several important material behaviors, including hysteresis, plastic deformation, and softening. For this application, the material chosen for the spring element must be able to exert the same force at full extension and return to its initial position once the load is removed. This requires repeatability in terms of the stress-strain relation. The three material behaviors mentioned result in irregularities in the stress-strain curve, causing unintended elongation of the spring element and short life of part functionality. Therefore, this material is not the best choice for the application. In addition to the material requirements listed, the material should have the capability of undergoing a fabrication process that allows for affordable customization, such as 3D-printing.

While FFD printing is focused on in this thesis, other print methods such as stereolithography (SLA) should also be considered.

4 Proposed Design

4.1 Introduction

This chapter focuses on how the topics of previous chapters can be combined to produce components of the design for a customized orthotic glove. A group of hypothetical hands are presented, along with data acquisition methods present in clinical settings, referred to as "fittings" for the glove. The inputs for the algorithm are drawn from this fitting. The outputs of the algorithm from the group of hypothetical hands are stated and discussed.

4.2 Fitting Procedure and Algorithm Inputs

For this translational study, a hypothetical hand is presented for showing the algorithm's operation and use. Measurements of the hand must be taken for input data. The clinician may measure each finger of the hand physically using a ruler, calipers, or sizing rings. Alternatively, a 3D scan of the hand may be made and measured using rendering software. For a physical measurement, the geometry measured is shown in Figure 4.1, where d_{i1}, d_{i2}, and d_{i3} are the measured diameters of the MCP, PIP, and DIP joints, respectively.
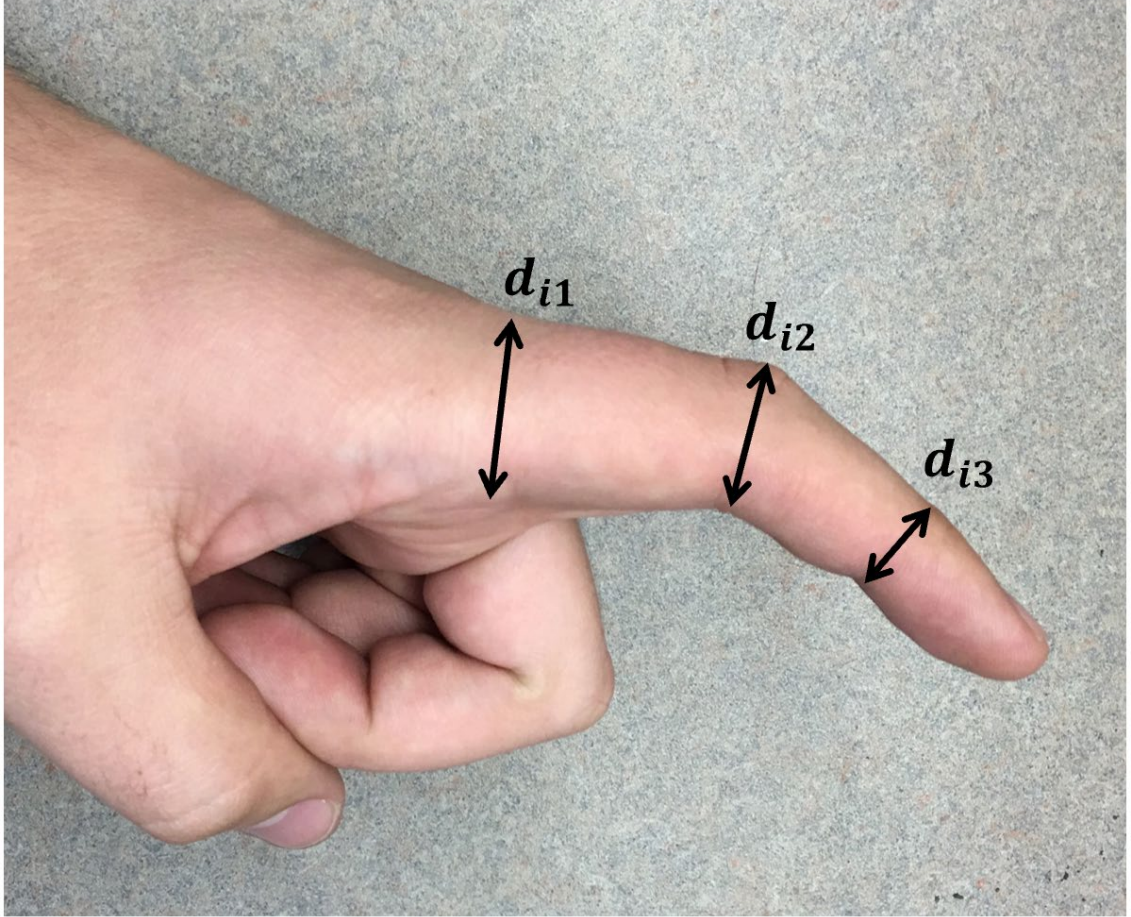
Figure 4.1: Physical finger image for joint diameter measurement

Finding the diameters of the finger joints for each finger allows for calculation of the radii for the model. The model laid over the finger in Figure 4.1 is shown in Figure 4.2, where r_{i1}, r_{i2}, and r_{i3} are the radii of the MCP, PIP, and DIP joints, respectively.
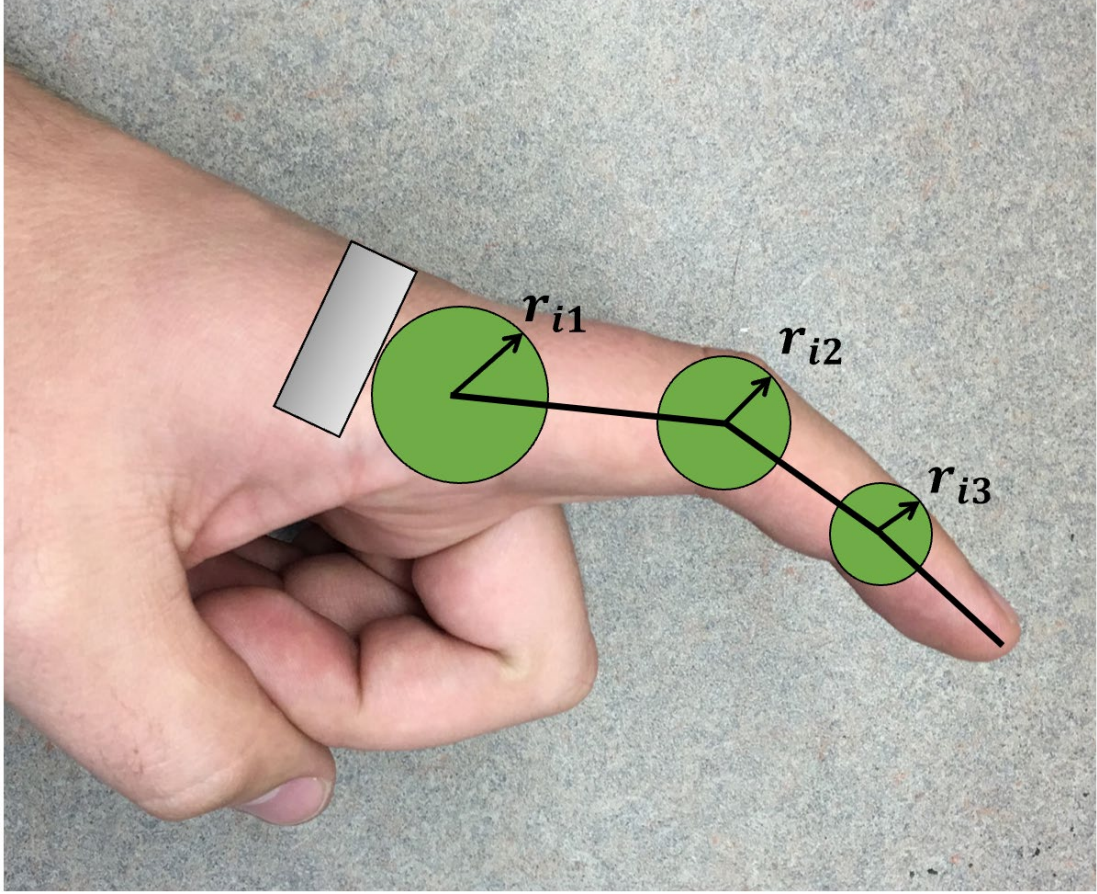
Figure 4.2: Finger model overlay for joint radius calculation

The radius r_{ik} is defined in Equation (4.1) as half of the diameter d_{ik}.

$$r_{ik} \triangleq \frac{d_{ik}}{2}$$
(4.1)

The clinician may also measure joint diameter with a 3D scan of the hand. The scan geometry corresponding to the joints must be identified by the medical professional, then a measurement may be made. An example of a joint measurement from a 3D scan is shown in Figure 4.3. The same process is used to calculate the radii of the three joints.
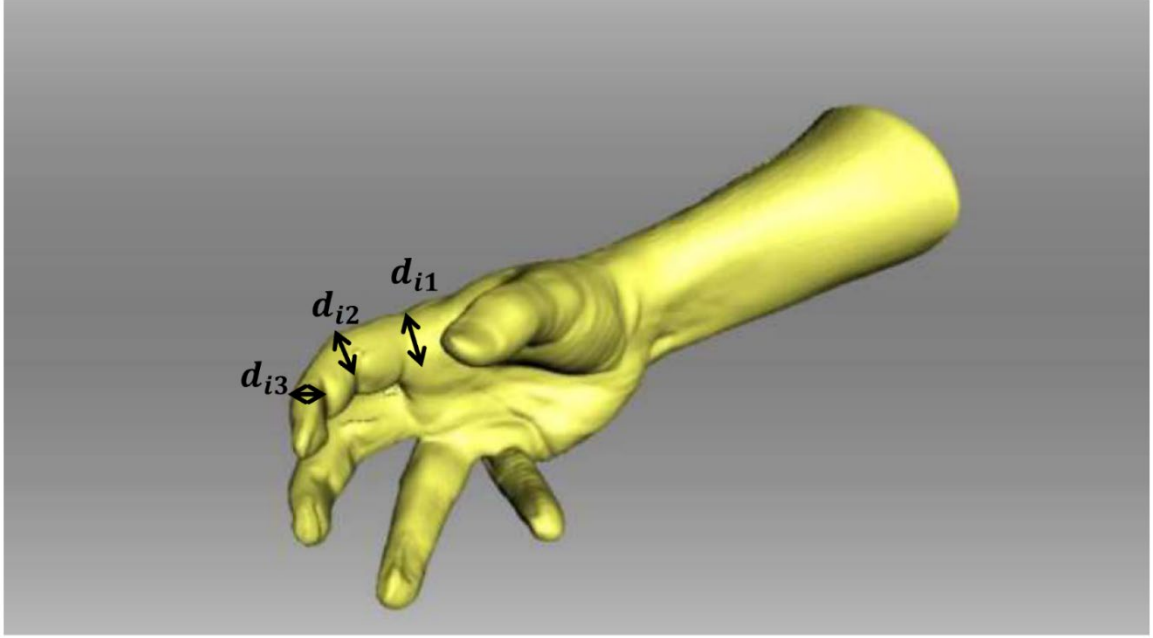
Figure 4.3: 3D scan of hand with finger diameter measurement

However the radii are determined, they are necessary as inputs for the algorithm. The radii of each joint on each finger are used in calculations.

The clinician must also measure the current position of the fingers of the hand in terms of the relative rotation angles $\theta_{r,ik}$. In the clinical setting, angle measurement of joints is typically performed by a goniometer, but again, 3D scans of the hand may be used.
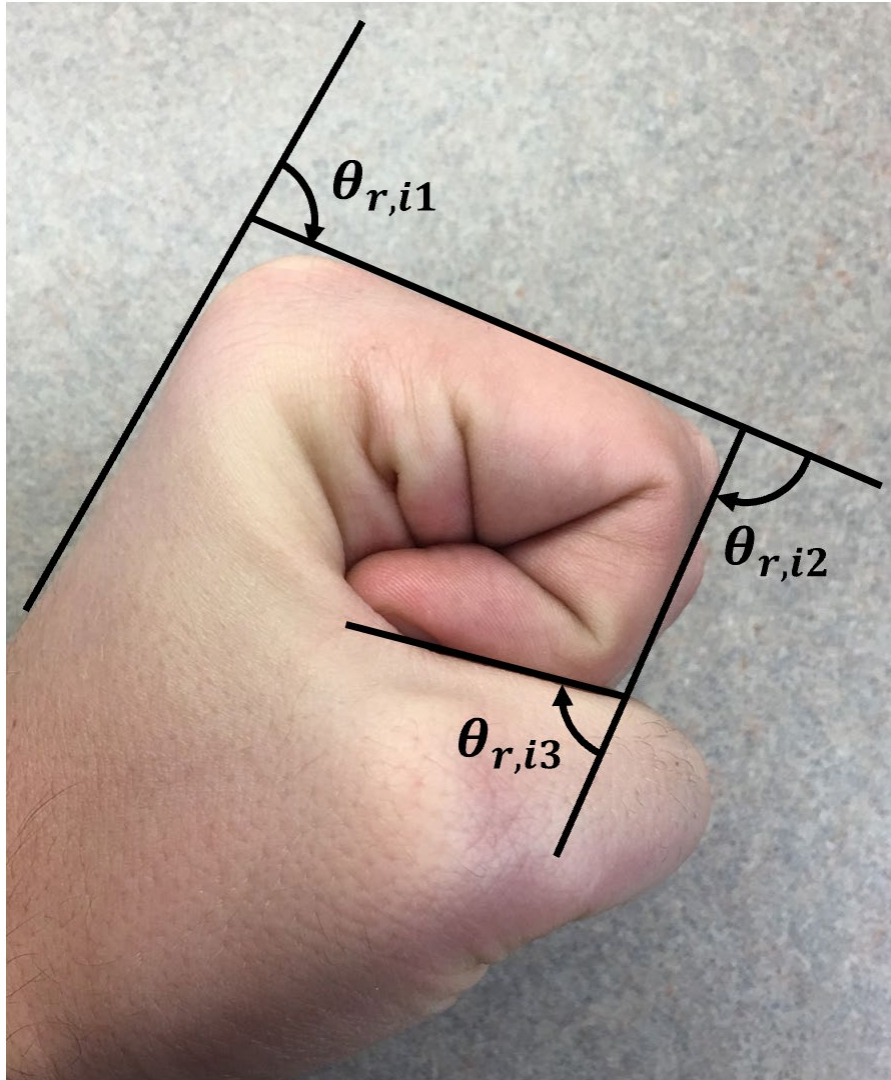
Figure 4.4: Physical measurement of relative angles of finger segments

The same 3D scan shown in Figure 4.3 is again used to show how a 3D scan is used for measurement purposes. The 3D scan's angle measurements are shown in Figure 4.5.
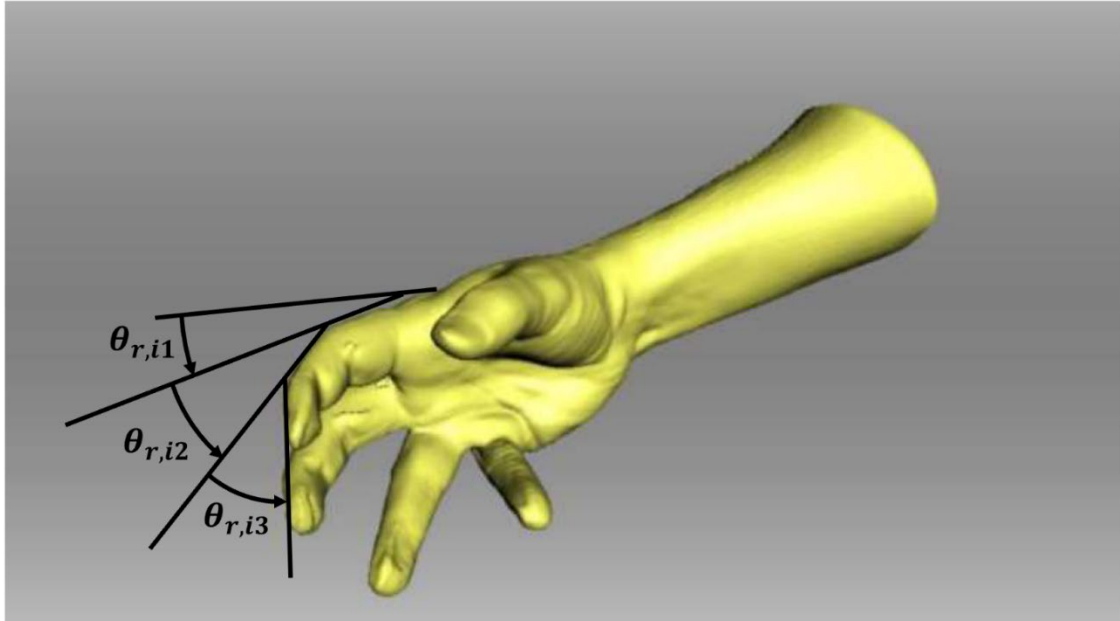
Figure 4.5: 3D scan measurement of relative angles of finger segments

These joint angles for each finger are also used as inputs for the algorithm.

The final measurement to be taken is the grip strength of the affected hand. This measurement is done by a hand dynamometer, shown in Figure 4.6.

Figure 4.6: Hand dynamometer for measuring grip strength

The grip strength of the hand that is being fitted is the final input for the algorithm. The data measured by these methods are shown in Table 4.1. The sizes were determined using values from previous studies that measured hand dimension of samples of the populations (Chandra, Chandna and Deswal 2011).

Table 4.1: Hypothetical hand data, all lengths in millimeters, angles in degrees, forces in Newtons

Finger		d_{i1}	d_{i1}	d_{i1}	r_{i1}	r_{i1}	r_{i1}	$\theta_{r,i1}$	$\theta_{r,i1}$	$\theta_{r,i1}$	$F_{i,total}$
Index	$i = 1$	24	20	18	12	10	9	60	50	40	
Middle	$i = 2$	26	23	20	13	11.5	10	50	40	35	142.2
Ring	$i = 3$	24	20	18	12	10	9	60	50	45	
Little	$i = 4$	22	18	17	11	9	8.5	90	80	70	

The clinician must also determine what the correction angles are for the given hand. The angles determine what position the fingers are held at once the spring element is producing its calculated force. The angles' values are a matter of medical professional opinion and are left to the clinician to choose. The correction angles for the hypothetical hand in question are shown in Table 4.2.

Table 4.2: Hypothetical hand correction angles, in degrees

Finger		$\theta_{c,i1}$	$\theta_{c,i1}$	$\theta_{c,i1}$
Index	$i = 1$	40	30	20
Middle	$i = 2$	25	20	20
Ring	$i = 3$	40	30	20
Little	$i = 4$	50	40	25

These inputs are used as inputs into the algorithm that was developed in the sections covering the finger mechanical model and the spring element design. The algorithm structure is provided in Figure 4.7, where the blue boxes are the inputs from the clinician and the designer, red boxes are the intermediate calculations, and the green boxes are the outputs of the algorithm.

The band is assumed to have a square cross-section, which allows the algorithm to solve for a single, definitive output.
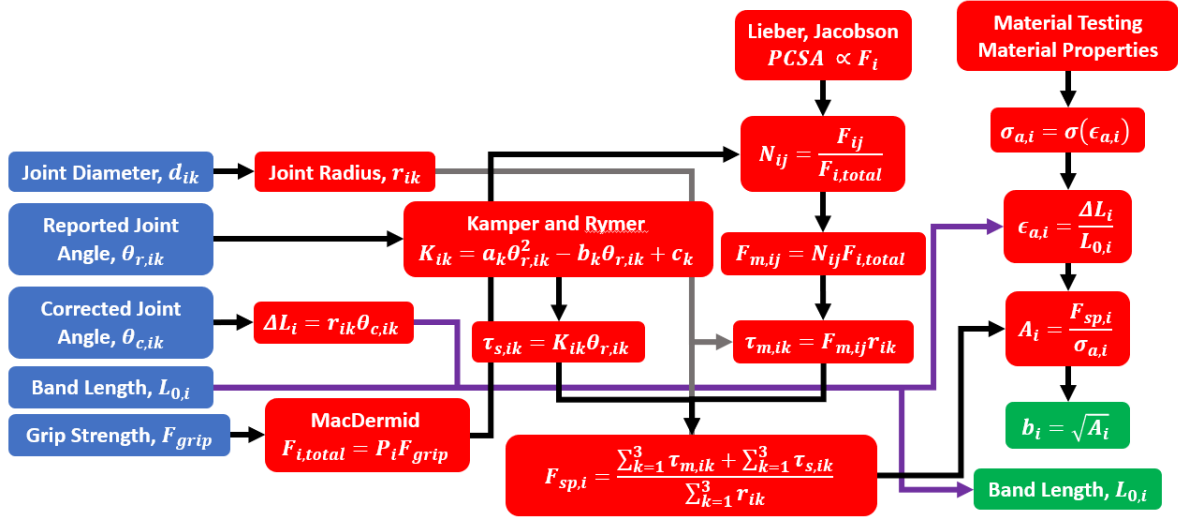
Figure 4.7: Algorithm structure

4.3 Algorithm Outputs and Design

Once the proper inputs for the algorithm have been entered and the algorithm has been executed, the outputs presented are used to design the glove. The outputs are listed in Table 4.3.

Table 4.3: Algorithm outputs for glove design, all lengths in millimeters

Property	Index	Middle	Ring	Little
Side Length (mm)	9.9	12.5	10	7.7
Band Length (mm)	25.4	25.4	25.4	25.4

Included in Table 4.3 are the side lengths of the band's cross-section and the band's length. The ultimate design output is the dimension of the cross-section sides, but the band's length was shown for completeness, as this would also be needed to design the bands. The

78

outputs include all necessary information to create the spring elements for the proposed glove. The main geometry of the spring element is given in Figure 2.6, with the exception of the attachment points. An existing orthotic device from Saebo, Inc. known as the Saebo Flex was modified to illustrate this application of 3D-printed spring elements, and is shown in Figure 4.7.
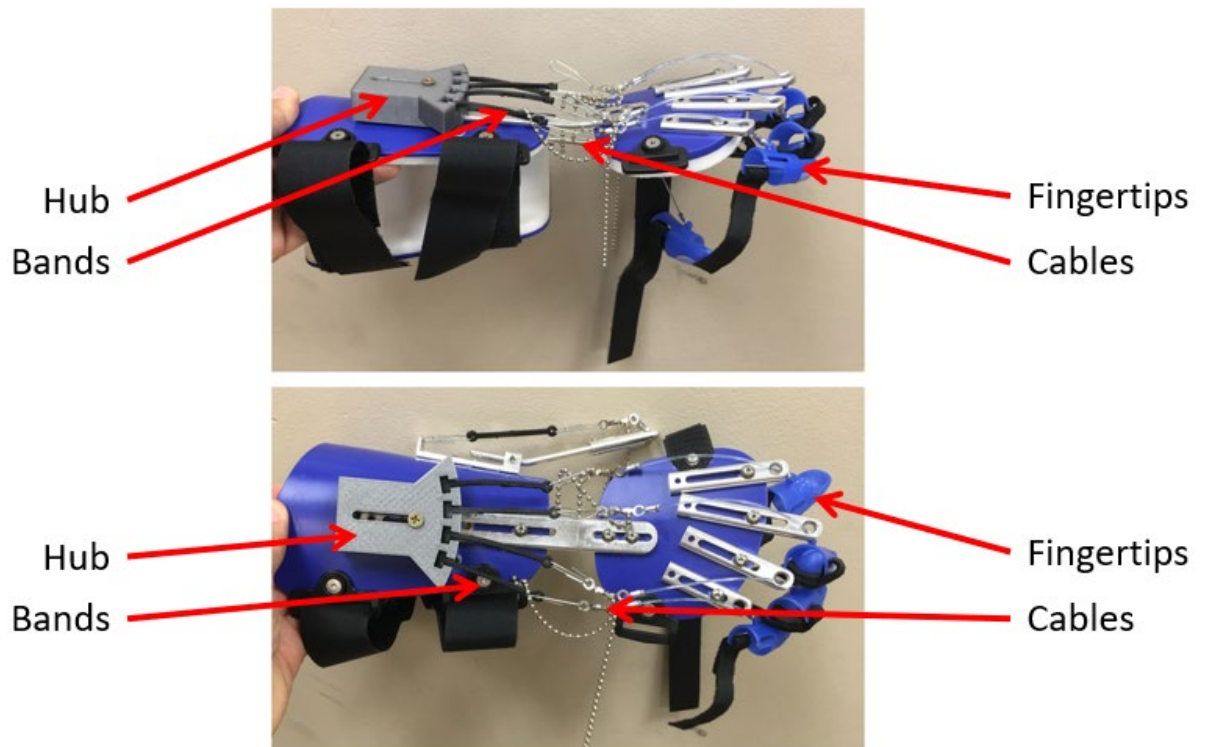
Figure 4.8: Modified orthotic device with spring elements installed, side view (top) and top view (bottom)

The attachment of the spring elements is done through loops incorporated into the model and 3D-printed to size. The bands connect proximally on top of the hand via a rigid support, shown as the gray hub on top of the wrist piece of the orthotic device. The bands will connect distally to cables or wire, similar to what is shown in the mechanical model in Figure 2.3. When the glove is stretched over the hand and fingers, the band will exert a force greater than that of the muscles. This causes the hand to be opened to the degree specified by the clinician in Table 4.2. At this

position, the stretched band will relax enough such that the produced band force now balances

out the forces exerted by the flexor muscles. An example of the Saebo Flex device being worn is

shown in Figure 4.8, and accurately illustrates how the orthotic device proposed in this thesis

would fit someone's hand and hold the fingers in an open position.
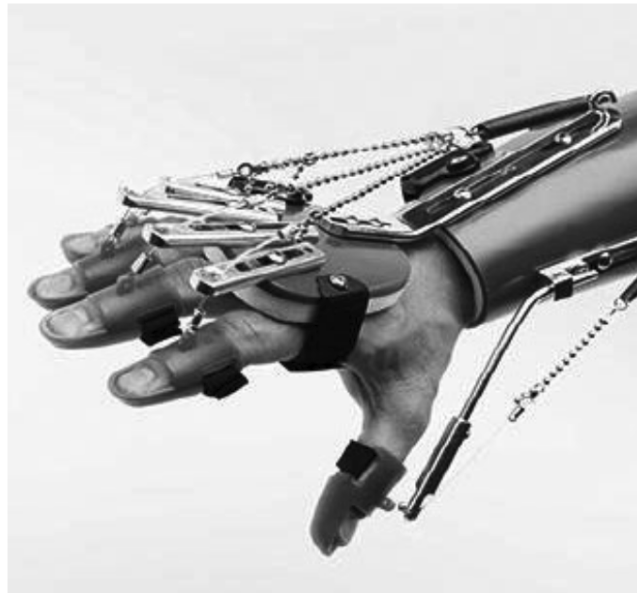
Figure 4.9: Saebo Flex orthotic device on a person's hand (Lannin, et al. 2016)

The result is a glove designed to meet clinician specifications for recovery through use of

the engineering principles of kinematics, mechanical design, and material properties.

5 Conclusions and Recommendations

5.1 Summary

A list of key points from this thesis are provided below:

1. A mechanical model of a human finger was posed that included information from anatomy and biomechanics. A triple-rod pendulum was used as the model's base. The model incorporated a cable system and eyelets to guide them with the purpose of mimicking the function of the tendons of the flexor muscles and the tendon sheaths that hold them closely to the finger bones. Equations from biomechanics and mechanical engineering were used to develop relationships between grip strength of the hand, grip strength of a finger, flexor muscle forces, and induced joint torques. Passive joint stiffness was also incorporated into the model.

2. A spring element of rectangular cross section was presented as a passive method of balancing out the joint torques induced by joint stiffness and flexor muscles of a finger. The force from the spring element was applied to the tip of the finger, and through experimental observation was found to apply a torque to each joint on the finger.

3. Material testing was conducted on thermoplastic elastomer (TPE) that was 3D-printed using fused-filament deposition (FFD). Tensile testing to failure was performed on specimens with four different infill orientations to determine infill effects on bulk material properties. Five samples were tested for each infill orientation. The test's raw data was averaged across the samples for a given infill orientation, and a sixth-order polynomial was used to fit the averaged data points. Differences in the curves were observed, and factors influencing these differences were posed, including material strand orientation as

it relates to loading direction, interlayer contact area, and reorientation/compression of material strands at high strains.

4. Cyclic testing within the extension range of 25mm and 40mm was performed for 25 cycles on a printed specimen with the infill orientation [45,-45] degrees. The raw data was plotted and presented. Material behaviors including hysteresis, plastic deformation, and softening were observed and factors contributing to these behaviors were presented. Cyclic testing within four smaller extension ranges were performed for 5 cycles each on specimens of the same type of infill orientation. Raw data for each range were plotted and compared, with the main findings being that the material behaviors found in the 25-cycle test became less pronounced was the extension ranges moved closer to zero.

5. A fitting procedure was posed that would yield the proper inputs for the algorithm developed from the equations in the finger mechanical model and spring element design. A hypothetical hand was presented, with measurements of key parameters discussed in the fitting procedure. The measurements were based upon measurements made in previous literature. The algorithm's structure was shown, and algorithm outputs were stated and discussed. The use of these outputs is mentioned, and images of the spring elements on an existing orthotic device are shown to illustrate how the resulting device proposed by this thesis may be designed in full, as well as how the device will be worn by the patient.

5.2 Conclusions

From the work presented in this thesis, the following conclusions are made:

1. A human hand exhibiting spasticity post-stroke has the potential to be modeled by a triple-rod pendulum with damping at the joints and cable systems that mimic the presence of structural ligaments and actuation of flexor muscles, respectively.

2. A method for determining contributions of each of the hand's digit flexor muscles is proposed by quantifying the physiological cross-sectional area (PCSA) of each muscle and normalizing them with reference to the total PCSA, thus giving a percentage of contribution to total flexion force to each individual muscle responsible.

3. Tensile tests provided data that showed a highly nonlinear relationship between stress and strain for 3D-printed thermoplastic elastomer (TPE).

4. The nonlinear stress-strain curve of 3D-printed TPE can be estimated by a sixth-order polynomial curve that fits the data from tensile testing between the longitudinal strains of 0 mm/mm and 4 mm/mm.

5. The print infill orientation [45,90] exhibited a different material behavior as shown in the stress-strain curve, compared to the curves of the other three infill orientations.

6. Hysteresis and softening are present in 3D-printed TPE within the first 5 cycles at various extension ranges, forcing a reconsideration of TPE as a suitable material for this application.

7. Softening is most pronounced during the first cycle of the repeated loading tests, indicating a "break-in" period for this material. After the first cycle, softening occurs much more gradually.

8. Potential factors contributing to material behavior are presented, including loading effects of axially-oriented material strands, inter-layer contact area, and reorientation of material strands at high strains.

9. Desired characteristics of the spring element material are given after determining that TPE may not be the best material. These characteristics include no hysteresis or softening within the operating range, flexibility, and the ability to be custom-fabricated at a low cost.

10. There is potential for a full bridging of knowledge between the disciplines of mechanical engineering and medicine through use of a computer algorithm which accepts human hand geometry, finger positioning, and grip strength as inputs; incorporates these into calculations based upon understandings of human anatomy, biomechanics, engineering statics, mechanical design, and material properties; and returns design parameters for a corrective elastic band to be used in a wearable orthotic. The application may be used for stroke survivors exhibiting spasticity in their hand as well as other groups requiring physical therapy, such as those involved in car accidents, sports injuries, and wounded veterans.

5.3   Future Work

The following recommendations are made to further the work of this study:

1. Tensile tests and cyclic loading tests of more varieties of print infill orientation to further establish a correlation between infill orientations and bulk material properties.

2. Tensile tests and cyclic loading tests of 3D-printed specimens created with other print settings such as temperature, extrusion rate, print speed, and others, with the goal of

identifying correlations between changes in these print settings and bulk material properties.

3. Cyclic loading tests of the material with more cycles to better characterize the material behavior of 3D-printed TPE, possibly a fatigue test to failure.

4. A study of other materials used for the spring element to determine a suitable material that provides the best material for the application.

5. An analysis of 3D-printed materials that seeks to determine the contributors to the bulk material properties and quantify their contribution.

6. An analysis of thermoplastic behavior within TPE material and its effects on tensile loading to failure as well as cyclic loading.

7. A study of 3D-printed TPE with a continuum mechanics approach. Tensile tests were the only test conducted in this study. To truly characterize a material, other tests must be conducted such as biaxial tension, shear testing, and others. These sets of data can be used to develop a constitutive model for 3D-printed TPE.

8. An analysis of cyclic loading of TPE that seeks to determine the cause of the relatively large softening experienced between the loading portion and de-loading portion of the first cycle. The analysis should also include various extension ranges to quantify how this softening changes with respect to extension range during the cyclic loading.

9. A study using 2D imaging and/or 3D scanning to determine the prescribed data for the fitting of the glove for an individual person. This may not be a feasible option for all clinicians, but it would serve to provide an alternative option to measuring with the current variety of diagnostic tools used in the clinical setting.

10. An analysis of the connection loops at the end of the spring element band for proper design around stress concentrations and force generated by the element. This area is most likely to experience failure in the band and must be analyzed for optimal life of the part.

11. A study of the proposed glove's efficacy in providing the correct force to balance those created from the flexor tendons in the fingers.

12. Designing a device that measures the contribution of each flexor tendon in the finger to the total gripping force of that finger *in vivo*, as none exist currently and would have been a major contribution to this study.

13. A study of the proposed glove's areas of improvement for successful integration into the daily life of the wearer, including design considerations such as comfort, safety, and aesthetics.

14.

15. A study of the effects of factors such as age, finger size, arthritis, previous hand injuries, weather, and stress levels on a finger's joint stiffness, identifying which factors have the largest effect.

16. A development of a robust control technique to account for uncertainties a finger's joint stiffness caused by factors such as age, finger size, arthritis, previous hand injuries, weather, and stress levels.

A study determining a second-order relationship between joint stiffness and joint flexion angle for the middle, ring, and little fingers, similar to the study conducted on the index finger (Kamper and Rymer 2001).

Appendix A: Pseudocode for Design Algorithm

```
INPUT finger joint diameters for each finger
INPUT current finger joint angles for each finger
INPUT desired finger joint angles for each finger
INPUT initial length of spring element band
INPUT measured grip strength

COMPUTE finger joint radii as half of finger joint diameters
COMPUTE stiffness of each joint as function of current finger
joint angles
COMPUTE grip strength contribution from each finger
COMPUTE contribution from each flexor muscle to total flexion
force
COMPUTE produced torque from flexor muscles
COMPUTE produced torque from joint stiffness
COMPUTE summation of moments from flexor muscles and joint
stiffnesses
COMPUTE required spring element force as quotient of moment
summation and joint radii
COMPUTE band deflection as sum of products of radii and desired
joint angles

COMPUTE strain as quotient of band deflection and initial band
length
COMPUTE stress as sixth-order function of strain found in tensile
test data
COMPUTE cross-sectional area of band as quotient of required band
force and stress on band at determined strain
COMPUTE cross-section side length as square root of cross-
sectional area, assuming a square cross-section
```

Appendix B: Simplify3D Printer Settings for TPE

EXTRUDER	EXTRUSION MULTIPLIER	1.35
LAYER	PRIMARY LAYER HEIGHT (mm)	0.2
	TOP SOLID LAYERS	1
	BOTTOM SOLID LAYERS	2
	OUTLINE/PERIMETER SHELLS	1
	FIRST LAYER HEIGHT (%)	100
	FIRST LAYER WIDTH (%)	120
	FIRST LAYER SPEED (%)	60
ADDITIONS	RAFT TOP LAYERS	N/A
	RAFT BASE LAYERS	N/A
	RAFT OFFSET FROM PART (mm)	N/A
	SEPARATION DISTANCE (mm)	N/A
	RAFT TOP INFILL (%)	N/A
	ABOVE RAFT SPEED (%)	N/A
INFILL	INTERNAL FILL PATTERN	Rectilinear
	EXTERNAL FILL PATTERN	Rectilinear
	INTERIOR FILL PERCENTAGE	100
	OUTLINE OVERLAP	50
	INFILL EXTRUSION WIDTH	110
	MINIMUM INFILL LENGTH	0.5
	INFILL ANGLE OFFSETS	45,-45
TEMP	EXTRUDER TEMPERATURE (°F)	250
	BED TEMPERATURE (°F)	50
COOL	PER LAYER FAN CONTROLS (% SPEED)	0
SPEEDS	DEFAULT PRINTING SPEED (mm/min)	3600
	OUTLINE UNDERSPEED (%)	100
	SOLID INFILL UNDERSPEED (%)	100

Appendix C: Matlab Code For Stress-Strain Curve Plotting

```matlab
%---TPE Stress-Strain Curve Plot---
%Kevin Richardson, 2018

clear
clc

e = 0:0.01:4;
c = [-0.0662 0.8805 -4.6897 12.705 -17.433 13.75 0.4089;
    -0.0897 1.19 -6.3655 17.376 -23.82 17.877 0.6934;
    -0.0669 0.8842 -4.7299 12.963 -17.931 14.209 0.469;
    -0.0637 0.8422 -4.494 12.329 -17.216 13.803 0.4054];
v = [e.^6; e.^5; e.^4; e.^3; e.^2; e; ones(1,length(e))];
s = c*v;

plot(e,s(1,:),'k','LineWidth',2)
hold on
plot(e,s(2,:),'r','LineWidth',2)
plot(e,s(3,:),'g','LineWidth',2)
plot(e,s(4,:),'b','LineWidth',2)
hold off
xlabel({'$\epsilon$ $(mm/mm)$'},
'Interpreter','Latex','FontSize',14)
ylabel({'$\sigma$ $(MPa)$'},'Interpreter','Latex','FontSize',14)
set(gca,'FontSize',14)
grid on
legend({'[0,45]','[45,90]','[0,90]','[45,-
45]'},'Location','northwest','NumColumns',2)

%---End Of Script---
```

References

Abdallah, Ismail Ben, Yassine Bouteraa, and Chokri Rekik. 2017. "Design and development of 3d printed myoelectric robotic exoskeleton for hand rehabilitaiton." *International Journal On Smart Sensing and Intelligent Systems* 10 (2): 341-366.

Arifa, Kunza, Muhammad M. Rahman, and Eylem Asmatulu. 2018. "Mechanical properties of 3D printed PLA specimens with various infill shapes and volumes." *TechConnect Briefs* 104-107.

Bahr, Ryan, Taoran Le, Manos M. Tentzeris, Stefano Moscato, Marco Pasian, Maurizio Bozzi, and Luca Perregrini. 2015. "RF characterization of 3d printed flexible materials - ninjaflex filaments." *Proceedings of the 45th European Microwave Conference (EuMC).* Paris, France. 742-745.

Baronio, Gabriele, Paola Volonghi, and Alberto Signoroni. 2017. "Concept and design of a 3d printed support fo assist hand scanning for the realization of customized orthosis." *Applied Bionics and Biomechanics* 1-8.

Baronio, Gabriele, Sami Harran, and Alberto Signoroni. 2016. "A critical analysis of a hand orthosis reverse engineering and 3d printing process." *Applied Bionics and Biomechanics* 1-7.

Bigoni, Matteo, Silvia Baudo, Veronica Cimolin, Nicola Cau, Manuela Galli, Lucia Pianta, Elena Tacchini, Paolo Capodaglio, and Alessandro Mauro. 2016. "Does kinematics add meaningful information to clinical assessment in post-stroke upper limb rehabilitation? A case report." *The Journal of Physical Therapy Science* 28 (8): 2408-2413.

Chandra, Arunesh, Pankaj Chandna, and Surinder Deswal. 2011. "Analysis of hand anthropometric dimensions of male industrial workers of haryana state." *International Journal of Engineering* 5 (3): 242-256.

Chen Chen, Fai, Silvia Appendino, Alessandro Battezzato, Alain Favetto, Mehdi Mousavi, and Francesco Pescarmona. 2013. "Constraint study for a hand exoskeleton: human hand kinematics and dynamics." *Journal of Robotics* 1-17.

Clauser, Charles E., John T. McConville, and J. W. Young. 1969. *Weight, Volume, and Center of Mass of Segments of The Human Body.* R&D Report, Air Force Aerospace Medical Research Lab Wright-Patterson AFB, OH.: National Technical Information Service: U.S. Department of Commerce.

Cobos, Salvador, Manuel Ferre, M.A. Sanchez Uran, Javier Ortego, and Cesar Pena. 2008. "Efficient Human Hand Kinematics for Manipulation Tasks." *IEEE/RSJ Internation Conference on Intelligent Robotics and Systems.* Nice, France: Institute of Electrical and Electronics Engineers Inc. 2246-2251.

Davidoff, Neil A., and Andris Freivalds. 1993. "A graphic model of the human hand using CATIA." *Internation Journal of Industrial Ergonomics* 12 (4): 255-264.

Drozdov, A. D. 2007. "An unusual elastoplastic response of thermoplastic elastomers at cyclic deformation." *International Journal of Engineering Science* 45: 660-678.

Drozdov, A. D., and J. deC. Christiansen. 2007. "Cyclic viscoplasticity of thermoplastic elastomers." *Acta Mechanica* 194: 47-65.

Ewing, J. A. 1889. "On Hysteresis in the relation of Strain to Stress." *Report of the British Association for the Advancement of Science, 59th Meeting.* Newcastle-upon-Tyne, England: Spottiswoode And Co. 502-504.

Fenner Drives. 2016. "NinjaFlex 3D Printing Filament." *NinjaTek | NinjaFlex.* April. Accessed November 12, 2018. https://ninjatek.fppsites.com/wp-content/uploads/2018/10/NinjaFlex-TDS.pdf.

2011. "Flexor Tendon Injuries." *OrthoInfo.* Accessed November 5, 2018. https://orthoinfo.aaos.org/en/diseases--conditions/flexor-tendon-injuries/.

Franko, Orrin I., Taylor M. Winters, Timothy F. Tirrell, Eric R. Hentzen, and Richards L. Lieber. 2011. "Moment arms of the human digital flexors." *Journal of Biomechanics* 44 (10): 1987-1990.

Garrett, John W. 1968. *Clearance and performance values for the bare-handed and the pressure-gloved operator.* R&D Report, Air Force Aerospace Medical Research Lab Wright-Patterson AFB, OH.: National Technical Information Service: U.S. Department of Commerce.

Gosling, J. A., P. F. Harris, J. R. Humpherson, I. Whitmore, and P. L. T. Willan. 2008. *Human Anatomy: Color Atlas and Textbook, Fifth Edition.* Philadelphia: Elsevier Health Sciences.

Gray, Vicki, Charles L. Rice, and S. Jayne Garland. 2012. "Factors That Influence Muscle Weakness Following Stroke and Their Clinical Implications: A Critical Review." *Physiotherapy Canada* 415-426.

Gustus, Agneta, Georg Stillfried, Judith Visser, Henrik Jorntell, and Patrick van der Smagt. 2012. "Human Hand Modelling - Kinematics, Dynamics, Application." *Biological Cybernetics* 106 (11-12): 740-755.

Hanten, William P., Wen-Yin Chen, Alicia Ann Austin, Rebecca E. Brooks, Harlan Clay Carter, Carol Ann Law, Melanie Kay Morgan, Donna Jean Sanders, Christe Ann Swan, and Amy Lorraine Vanderslice. 1999. "Maximum Grip Strength In normal Subjects From 20 To 64 Years Of Age." *Journal of Hand Therapy* 12 (3): 193-200.

Hipolite, Whitney. 2014. "Quack-Quack the duck walks again thanks to a 3d printed leg brace." *3D Print.* August 11. Accessed November 5, 2018. https://3dprint.com/11563/3d-printed-duck-leg-brace/.

Huber, Justin, Kevin Richardson, Lumy Sawaki, and Lyndon Scott Stephens. 2017. "Three-Dimensional Printing of Components for a Dynamic Upper Extremity Orthotic: Prototype Development." *2017 International Symposium on Wearable Robotics and Rehabilitation (WeRob).* Houstin, Texas, USA: IEEE. 1-1.

Jacobson, Mark D., Rajnik Raab, Babak M. Fazeli, Reid A. Abrams, Michael J. Botte, and Richard L. Lieber. 1992. "Architectural design of the human intrinsic hand muscles." *The Journal of Hand Surgery* 17 (5): 804-809.

Johnston, Mallory M., Mary J. Werkheiser, and Kenneth G. Cooper. 2014. "3D printing in zero-g ISS technology demonstration."

Kamper, D. G., and W. Z. Rymer. 2001. "A Biomechanical Simulation Of The Effect Of The Extrinsic Flexor Muscles On Finger Joint Flexion." *Annual International Conference of the IEEE*

Engineering in Medicine and Biology - Proceedings. Institute of Electrical and Electronics Engineerings Inc. 1256-1259.

Kasza, Damian. 2018. "Modelling of underground objects and geological-tectonic structures from a point cloud: application of the developed models in studies of geodynamic processes." *E3S Web of Conferences.*

Kim, Dong Hyun, Sang Wook Lee, and Hyung-Soon Park. 2014. "Feedback Control of Biomimetic Exotendon Device for Hand Rehabilitation in Stroke." *Engineering in Medicine and Biology Society (EMBS), 2014 36th Annual Internation Conference of the IEEE.* Institute of Electrical and Electronic Engineers Inc. 3618-3621.

Lannin, Natasha A., Anne Cusick, Caroline Hills, Bianca Kinnear, Karin Vogel, Kate Matthews, and Greg Bowring. 2016. "Upper limb motor training using a Saebo orthosis is feasible for increasing task-specific practice in hospital after stroke." *Australian Occupational Therapy Journal* 63 (6): 364-372.

Lee, Sang Wook, Katlin A. Landers, and Hyung-Soon Park. 2014. "Development of a Biomimetic Hand Exotendon Device (BiomHED) for Restoration of Functional Hand Movement Post-Stroke." *IEEE Transactions on Neural Systems and Rehabilitation Engineering* 22 (4): 886-898.

Lieber, Richard L., Mark D. Jacobson, Babak M. Fazeli, Reid A. Abrams, and Michael J. Botte. 1992. "Architecture of selected muscles of the arm and forearm: Anatomy and implications for tendon transfer." *The Journal of Hand Surgery* 17 (5): 787-798.

MacDermid, Joy C., Adrian Lee, Robert S. Richards, and James H. Roth. 2004. "Individual finger strength: are the ulnar digits "powerful"?" *Journal of Hand Therapy* 17 (3): 364-367.

Martin, Joel R., Mark L. Latash, and Vladimir M. Zatsiorsky. 2012. "Effects of the index finger position and force production on the flexor digitorum superficialis moment arms at the metacarpophalangeal joints - an magnetic resonance imaging study." *Clinical Biomechanics* 27 (5): 453-459.

McDonough, John K. (NinjaTek, Division of Fenner Drives, United States). 2016. "Thermoplastic polyurethanes for 3D printing." *Rubber World*, October: 40-42.

Moore, Jacob P., and Christopher B. Williams. 2008. "Fatigue Characterization of 3D Printed Elastomer Material." *19th Annual International Solid Freeform Fabrication Symposium (SFF).* Austin, TX. 4-6.

Moore, Jacob P., and Christopher B. Williams. 2015. "Fatigue properties of parts printed by Polyjet material jetting." *Rapid Prototyping Journal* 21 (6): 675-685.

Moy, F. M., E. W.H. Chang, and K. W. Kee. 2011. "Predictors of handgrip strength among the free living elderly in rural Pahang, Malaysia." *Iranian Journal of Public Health* 40 (4): 44-53.

Nimbarte, Ashish D., Rodrigo Kaz, and Zong-Ming Li. 2008. "Finger joint moton generated by individual extrinsic muscles: a cadaveric study." *Journal of Orthopaedic Surgery and Research* 3 (1): 27-33.

Pham, Trieu, Pubudu N. Pathirana, Hieu Trinh, and Pearse Fay. 2015. "A non-contact measurement system for the range of motion of the hand." *Sensors* 15 (8): 18315-18333.

Polygerinos, Panagiotis, Kevin C. Galloway, Siddharth Sanan, Maxwell Herman, and Conor J. Walsh. 2015. "EMG Controlled Soft Robotic Glove for Assistance During Activities of Daily Living." *2015 IEEE International Conference on Rehabilitation Robotics (ICORR)* 55-60.

Qingmeng, Li, Huang Jin, Wang Yang, Chen Tianfei, Hu Ying, Wu Xiang, and Chen Xinyu. 2012. "3D scanning system for digital dental based on line structured light sensor." *2012 International Conference on System Science and Engineering (ICSSE).* Institute of Electrical and Electronics Engineers Inc. 353-357.

Qiu, Dan, and Derek G. Kamper. 2014. "Orthopaedic applications of a validated force-based biomechanical model of the index finger." *2014 26th Annual International Conference of the IEEE Engineering in Medicine and Biology Society (EMBC).* Institute of Electrical and Electronics Engineers Inc. 4013-4016.

Rispler, David, Daniel Greenwald, Scott Shumway, Christopher Allan, and Daniel Mass. 1996. "Efficiency of the Flexor Tendon Pulley System in Human Cadaver Hands." *The Journal of Hand Surgery* 444-450.

Samadani, Ali-Akbar, Dana Kulic, and Rob Gorbet. 2012. "Multi-Constrained Inverse Kinematics for the Human Hand." *2012 Annual International Conference of the IEEE Engineering in Medicine and Biology Society (EMBS).* Institute of Electrical and Electronics Engineers Inc. 6780-6784.

Scavuzzo, Rudolph J. 2000. "Oscillating Stress on Viscoelastic Behavior of Thermoplastic Polymers." *Journal of Pressure Vessel Technology* 122: 386-389.

Spontak, Richard J., and Nikunj P. Patel. 2000. "Thermoplastic elastomers: fundamentals and applications." *Current opinion in colloid and interface science* 5.5 (6): 333-340.

2015. "Standard Test Method for Tensile Properties of Plastics." *ASTM Standard D638-14.* West Conshohocken, PA: ASTM International. doi:10.1520/D0638-14.

Stienen, Arno H.A., Theresa Sukal Moulton, Laura C. Miller, and Jules P.A. Dewald. 2011. "Wrist and Finger Torque Sensor for the Quantification of Upper Limb Motor Impairments Following Brain Injury." *2011 IEEE Internation Conference on Rehabilitation Robotics (ICORR).* Institute of Electrical and Electronics Engineers Inc. 1-5.

Wang, Kai, Yiting Shi, Wen He, Jing Yuan, Yuan Li, Xioalin Pan, and Ciulian Zhao. 2018. "The research on 3d printing fingerboard and the initial application on cerebral stroke patient's hand spasm." *Biomedical engineering online* 17 (1): 92-105.

Wang, Keming, Evan P. McGlinn, and Kevin C. Chung. 2014. "A Biomechanical and Evolutionary Perspective on the Function of the Lumbrical Muscle." *The Journal of Hand Surgery* 39 (1): 149-155.

Xu, Zhe, Emanuel Todorov, Brian Dellon, and Yoky Matsuoka. 2011. "Design and Analysis of an Artificial Finger Joint for Anthropromorphic Robotic Hands." *2011 IEEE Internation Conference on Robotics and Automation (ICRA).* Institute of Electrical and Electronics Engineers Inc. 5096-5102.

Vita

Kevin Thomas Richardson received his Bachelor of Science in Mechanical Engineering from the University of Kentucky on May 8th, 2016. During his undergraduate education, he was employed as an intern as Belcan Engineering Corporation, Webasto Roof Systems, Inc., and Quality Manufacturing, Inc. (QMI). During his stint at QMI, Kevin performed engineering design for automated assembly equipment for tier-1 manufacturers such as Lexmark and other companies, gaining practical engineering experience as well as involvement in working one-on-one with customers. Additionally, Kevin participated in the research and development of a rotational actuator through use of a curved hydraulic cylinder. The research resulted in a published patent (WO2017034849) and his first experience in research and in product development. This work enabled him to contribute valuable knowledge to his senior design project assigned during his senior year of his undergraduate studies. The project tasked Kevin and his team with designing and building a mobile dynamometer for the University of Kentucky Solar Car, which would enable the quantification of torque and power output of the solar car at speeds up to 90 miles per hour. The project was successful as a result of great teamwork, thorough engineering analysis via hand calculations and modeling in ANSYS Workbench, resourcefulness to stay within the allotted budget, and commitment to nothing but exceptional work. During his senior year of his undergraduate studies, Kevin made the decision to further his education and expand his horizons by pursuing his Master of Science in Mechanical Engineering at the University of Kentucky.

Kevin began his master's degree studies in the Fall of 2016. He was taken under the wing of Dr. L. Scott Stephens as his mechanical engineering faculty advisor and was brought onto a new

project presented by Dr. Lumy Sawaki and Justin Huber from the College of Medicine at the University of Kentucky. The project tasked team members with created a customized orthotic glove for stroke patients exhibiting spasticity in their hand and arm, with the goal of creating faster and more convenient recovery. This paper is one of the academic milestones within this initiative. Kevin also contributed to work presented at the 2017 International Symposium on Wearable Robotics and Rehabilitation by Justin Huber. At the beginning of his second year of his master's program in the Fall of 2017, Kevin was enrolled in the Entrepreneur's Bootcamp at the University of Kentucky, which is a semester-long bootcamp held by the Von Allmen Center for Entrepreneurship in the Gatton College of Business and Economics. The bootcamp placed Kevin as team leader of a group of students with the goal of exploring and pursuing a business opportunity surrounding the customized orthotic glove. Kevin gained invaluable knowledge, experience, and opportunities during this program, including effective networking, lean startup methodology, elementary financial analysis, and practical team management. The bootcamp was completed in December 2017, with Kevin's team earning the 4th place prize out of nearly 20 teams in the bootcamp based upon their final business pitch encompassing all aspects of the bootcamp material. Continuing the opportunity after the bootcamp, Kevin and his team pitched at 5Across, a pitch competition held by Awesome, Inc. in Lexington, Kentucky. The team again pitched in the regional and final rounds the Idea State U Business Model Competition, a state-level competition requiring a prepared pitch deck, business model document, and tradeshow-style booth for the company. In October 2018, the team was chosen by the University of Kentucky to represent the college in the SEC Pitch Competition, a competition consisting of one team from each college within the Southeastern Conference of American colleges, held at Texas A&M University.

Kevin's research interests include mechanical design, biomechanics, material science, and translational studies. Kevin also has strong interests in business, public speaking, product development, engineering design, and entrepreneurship.